Studies on Spin–Spin-Correlations in dileptonic $t\bar{t}$-events at LHC

Dissertation
zur Erlangung des Doktorgrades
des Department Physik
der Universität Hamburg

vorgelegt von

Benedikt Christopher Hegner

aus Bottrop

Hamburg
2008

Gutachter der Dissertation:	Prof. Dr. Joachim Mnich Prof. Dr. Peter Schleper
Gutachter der Disputation:	Prof. Dr. Joachim Mnich Jun.-Prof. Dr. Johannes Haller
Datum der Disputation:	10. März 2008
Vorsitzender des Prüfungsausschusses:	Prof. Dr. Karen Hagner
Vorsitzender des Promotionsausschusses:	Prof. Dr. Joachim Bartels
Leiter des Departments Physik:	Prof. Dr. Robert Klanner
Dekan der MIN-Fakultät:	Prof. Dr. Arno Frühwald

Zusammenfassung

Der Proton–Proton-Speicherring LHC wird im Sommer 2008 seinen Betrieb aufnehmen. Bei einer Schwerpunktsenergie von 14 TeV und einer anfänglichen Luminosität von 10^{33} cm^{-2}s^{-1} werden rund $8 \times 10^6 t\bar{t}$-Paare pro Jahr erzeugt. Aufgrund ihrer kurzen Lebensdauer zerfallen die beiden Quarks bevor eine Hadronisation stattfinden kann. Dies ermöglicht es, das Top-Quark als freies Quark zu untersuchen. Als Beispiel ist die Untersuchung des Top-Spins möglich. Die Information über den Spin des Tops wird an die Zerfallsprodukte weitergegeben und ist in Winkelverteilungen sichtbar. Aufgrund der Paarproduktionsprozesse sind die Spins der beiden Top-Quarks miteinander korreliert. Durch die hohe Ereignisrate wird man in der Lage sein, mittels des CMS-Experimentes genaue Studien der Spin–Spin-Korrelation durchzuführen. Die vorliegende Studie konzentriert sich auf den dileptonischen Zerfallskanal $t\bar{t} \rightarrow b\bar{b}l_1\bar{\nu}_1\bar{l}_2\nu_2$ bei einer integrierten Luminosität von 10 fb^{-1}. Für die vorbereitenden Studien wird eine detailierte Simulation des kompletten CMS-Detektors mit anschließ ender Rekonstruktion durchgeführt. Unter Berücksichtigung der zu erwartenden statistischen und systematischen Fehler lassen sich Spin–Spin-Korrelationen mit einer Genauigkeit von ca. 7% messen.

Summary

During summer of 2008 the proton–proton-collider LHC will start its operation. With a centre-of-mass engery of 14 TeV and an initial luminosity of 10^{33} cm^{-2}s^{-1} about 8×10^6 $t\bar{t}$-pairs will be produced per year. Due to its short lifetime the two quarks decay before any hadronization can take place and the top-quarks can be treated as a free quarks. As effect of this, a unique possibility is the study of the undiluted top-spin. The spin information of the top is passed to the decay particles and visible as angular distributions. Because of the processes that lead to the pair-production the spins of the two tops are correlated. The high event rate allows to do precise studies of spin–spin-correlations with the CMS experiment. The present study uses the dileptonic decay channel $t\bar{t} \rightarrow b\bar{b}l_1\bar{\nu}_1\bar{l}_2\nu_2$ at an integrated luminosity of 10 fb^{-1}. For the preparatory studies detailed event simulation and reconstruction for the CMS detector are done. Taking the expected statistical and systematic uncertainties into account a precision of 7% for the correlation measurement can be achieved.

Contents

Preface

The work presented in this thesis covers the measurement of spin–spin-correlations in the $t\bar{t}$-production with the CMS detector using the dileptonic decay channel. One of the unique features of the top quark is its very short lifetime. Therefore it decays without building bound-states and the information about its spin state gets almost perfectly transferred to the decay products, which is visible in angular distributions.

Chapter 1 describes the LHC accelerator and the experiments using this facility. An overview about the CMS detector serves as foundation for the following chapters describing the analysis of data reconstructed with this apparatus.

Chapter 2 summarizes some of the motivations for performing measurements in high energy physics. The most important features of proton–proton-collisions get briefly discussed and build a base for the following parts of the thesis.

The field of top-quark physics at LHC is discussed in chapter 3. One expected effect is the spin–spin-correlation in $t\bar{t}$ production. Observables for measuring this correlation are introduced and it further motivates why the study of correlations is best done in the dileptonic channel.

To increase the flexibility of the studies of spin–spin-correlations the used Monte-Carlo-Generator was extended. This gets shortly described in chapter 4. It is followed by a short introduction into the software and computing issues of current high energy physics experiments.

In chapter 6 the used definition and identification of basic physics objects like jets, b-jets or electrons is given. The performance of the reconstruction algorithms is tested and adjusted to fit the needs of the processes under study.

The actual topic of this thesis, the measurement of spin–spin-correlations, gets discussed in chapter 6. It is divided into four main parts. These are selection, kinematical reconstruction, unfolding and discussion of uncertainties.

Since the signature of dileptonic $t\bar{t}$-events is very clean, the selection can be done in a very simple manner. Important background contributions are checked for their influence on the measurement.

For the calculation of the spin–spin-correlation the full kinematics of each single event need to be known. Quality and performance of the used kinematical solver routine are discussed.

Effects of selection and migration lead to observed distributions which differ significantly from the expected behaviour. To be able to use the obtained data unfolding techniques are needed. An overview of possible algorithms is given and promising ones compared. Some are well suited for the physics under study and the information can be reconstructed in satisfactory quality.

An investigation of uncertainties completes this chapter. The obtained results are compared with other studies on the same field.

1. Introduction

Over the last hundred years the knowledge about the building blocks of matter has increased enormously. The driving experimental approaches have been scattering experiments. Starting from Rutherford's experiment in 1911 leading to the discovery of the atomic nuclei, several generations of collider experiments have been built and successfully operated. The results of these ever improving and other experiments are combined in the *Standard Model of Particle Physics*. It delivers astonishing precise results for the physics at particle colliders and is able to explain all present data. But several measurements outside collider physics, for example astronomical observations, indicate that the Standard Model does not cover all observed phenomena.

A new collider facility at the energy frontier will start its operation in the summer of 2008. The Large Hadron Collider (LHC) located at CERN will reach a centre-of-mass energy of about 14 TeV. Among other experiments two multi-purpose detectors – CMS and ATLAS – will use the facility to study a broad range of physics. At energies of the terascale many new physics that could unite findings of particle physics with astrophysical data are expected to emerge. But not only the search for new particles is covered by the experiments. Several already known effects of the Standard Model can be studied to a more precise level. For example, the top-quark was only discovered about ten years ago in 1995 and studies are still limited by the relatively small data sampes collected so far.

Because of its high mass, which is close to the electroweak symmetry breaking scale, the top-quark will be a good probe for the Standard Model. With a luminosity of 10^{33} cm^{-2}s^{-1} in the first years of running about one $t\bar{t}$ event per second or 8 million events per year are produced. Thus it is legitimate to call LHC a top factory and the machine will allow measurements in the top quark sector of surpassing precision.

Due to its almost intermediate decay the top-quark decays before any hadronization takes place. This opens the unique possibility to study the properties of a bare quark. Among those properties is the spin of the top. Not diluted by QCD effects the spin information is passed to the decay particles and is visible in their angular distributions. Because of this the top-quark is the only quark where a direct spin measurement is possible.

Whilst both top-quarks from pair production are hardly polarized in the Standard Model, their spins are correlated via the production process. This correlation is expected to be measurable at the LHC. A measurement would be a good consistency check of Standard Model predictions and could open the space for effects of new physics.

The goal of this thesis are preparatory studies of spin–spin-correlation measurements with the CMS detector. Techniques to measure the spin effects and possible precisions in the dileptonic $t\bar{t}$ channel are explored. Base of the study are Monte-Carlo samples and a full detector simulation, which provides currently the best base for CMS studies.

The thesis is structured as follows. Chapter 2 describes the LHC accelerator and the experiments using this facility. An overview about the CMS detector serves as foundation for the following chapters describing the analysis of data reconstructed with this apparatus.

Chapter 3 summarizes some of the motivations for performing measurements in high energy physics. The most important features of proton–proton-collisions get briefly discussed and build a base for the following parts of the thesis.

The field of top-quark physics at LHC is discussed in chapter 4. One expected effect is the spin–spin-correlation in $t\bar{t}$ production. Observables for measuring this correlation are introduced and it further motivates why the study of correlations is best done in the dileptonic channel.

To increase the flexibility of the studies of spin–spin-correlations the used Monte-Carlo-Generator was extended. This gets shortly described in chapter 5. It is followed by a short introduction into the software and computing issues of current high energy physics experiments.

In chapter 6 the used definition and identification of basic physics objects like jets, b-jets or electrons is given. The performance of the reconstruction algorithms is tested and adjusted to fit the needs of the processes under study.

The actual topic of this thesis, the measurement of spin–spin-correlations, gets discussed in chapter 7. It is divided into four main parts. These are selection, kinematical reconstruction, unfolding and discussion of uncertainties.

Since the signature of dileptonic $t\bar{t}$-events is very clean, the selection can be done in a very simple manner. Important background contributions are checked for their influence on the measurement.

For the calculation of the spin–spin-correlation the full kinematics of each single event need to be known. Quality and performance of the used kinematical solver routine are discussed.

Effects of selection and migration lead to observed distributions which differ significantly from the expected behaviour. To be able to use the obtained data unfolding techniques are needed. An overview of possible algorithms is given and promising ones compared. Some are well suited for the physics under study and the information can be reconstructed in satisfactory quality.

An investigation of uncertainties completes this chapter. The obtained results are compared with other studies on the same field.

A final summary and an outlook to possible extensions build the last chapter of the thesis.

2. The CMS Experiment at the LHC

2.1. The Large Hadron Collider

The LHC (Large Hadron Collider) [1] is currently under construction at CERN and will be the world's most powerful particle accelerator so far. The 27 km long storage ring is housed inside the old LEP tunnel and will provide two proton beams with both of an energy of 7 TeV, which is seven times bigger than the energies currently achieved at the $p - \bar{p}$ collider Tevatron. In another operation mode LHC will be able to provide $Pb - Pb$ collisions with an energy of about 2.76 TeV per nucleon.

The main LHC operation mode will be $p - p$ collisions. In the first years the LHC will run in a *low luminosity phase* of $10^{33}\,\mathrm{cm}^{-2}\mathrm{s}^{-1}$. Afterwards the mode will be switched to the *high luminosity phase* of $10^{34}\,\mathrm{cm}^{-2}\mathrm{s}^{-1}$. Collisions take place at a frequency of 40 MHz, corresponding to a bunch spacing of 25 ns. This sets very hard boundary conditions for the read-out electronics of all LHC experiments.

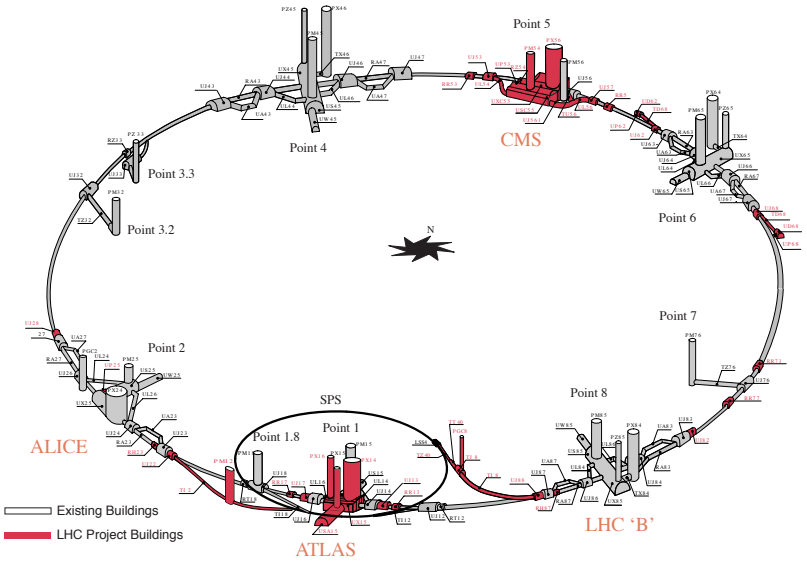

Figure 2.1.: The LHC ring with the old LEP (light grey) and the new LHC (red) facilities. On the four interaction points the six experiments are located. TOTEM and LHCf are not shown here and share their interaction point with CMS and ATLAS.

The injection to the LHC will be using many of the existing accelerator facilities at CERN, namely the Linac2, the Proton Synchrotron Booster (PSB), the Proton Synchrotron (PS) and the Super Proton Synchrotron (SPS). Details of

the injection procedure can be found in [2]. At the point of the injection into the main LHC ring the proton energy will be around 450 GeV. Refilling the ring and ramping up to nominal energy takes about 20 min. The physics runs and last for about 15 h.

Further information is available in [1, 2, 3]. For the sake of completeness some of the main parameters of the LHC machine for the pp-mode are shown in table 2.1.

Table 2.1.: Main LHC machine parameters for proton-beams.

Parameter	value	unit
Proton Energy	7000	GeV
Injection Energy	450	GeV
Number of Collision points	4	-
Number of particles per bunch	1.5×10^{11}	-
Number of bunches	2808	-
DC beam current	582	mA
Ring circumference	26.7	km
Main dipoles	1232	-
Dipole field	8.3	T
Bunch spacing	24.95	ns
Total crossing angle at I.P.	300	μrad

2.1.1. LHC Experiments

At LHC there will be six experiments, ALICE (A Large Ion Collider Experiment), ATLAS (A Toroidal LHC ApparatuS), CMS (Compact Muon Solenoid), LHCb (LHC beauty experiment), LHCf (LHC forward) and TOTEM (Total Cross Section, Elastic Scattering and Diffraction Dissociation at the LHC), which are located at four interaction points. These points can be seen in figure 2.1. TOTEM (not shown) shares the point 5 with the CMS experiment, while LHCf (not shown) shares point 1 with ATLAS. The following paragraphs briefly explain the different detectors and experiments. For a detailed discussion of the CMS design, see section 2.2.

ALICE

Unlike the other experiments at LHC, the ALICE detector serves only Heavy-Ion-Collisions. Its purpose is the study of the quark-gluon plasma (QGP), a state of matter that existed in the initial moments of the universe. Especially the design of the tracker is very challenging, since up to 50000 tracks would come from a single heavy ion interaction. To serve this the inner silicon tracker is followed by a huge time projection chamber (TPC). The photon spectrometer, build from lead-tungsten crystals, and the RICH detector are the next parts

inside the magnet. Outside the magnet and only surrounding half of the detector, a single muon arm will be used for muon identification. [4]

ATLAS

The ATLAS detector is designed as a multi-purpose detector with the general layout of a common collider detector. Specifics of the design are mainly driven by the choice of configuration of the magnetic field. Using a complementary design to the purely solenoidal field of CMS, the field of ATLAS is build from large air-core toroidal magnets. An additional 2 T solenoid surrounds the inner tracking system. [5]

The inner tracker is build of three parts – a silicon pixel vertex detector, a silicon strip tracker and a transition tracking detector (TTR), which allows additional particle identification. The next part is the solenoid, surrounded by a liquid-argon calorimeter with a high longitudinal segmentation. It is followed by the hadronic calorimeter (Fe-scintillator and Cu-liquid argon detector). The outermost part builds the muon spectrometer.

LHCb

The LHCb detector is build to especially study the physics of B-mesons and CP violations. Because of the forward emission of B mesons it is designed as single arm spectrometer. The innermost part is build from a vertex system at the beam pipe, surrounded by a dipole magnet and a tracking system. Charged-particle identification is provided by Ring-Imaging Cerenkov Hodoscopes (RICH). Calorimeters and a muon spectrometer complete the detector. For cleaner signatures with less simultaneous proton interactions, the proton beams will be weaker focused at the LHCb interaction point than for the other experiments. [6]

LHCf

The LHCf experiment shares the interaction point IP1 with ATLAS and is located at a distance of 140 m on either side. Its special purpose is the study of very forward collision remnants to have a solid measure for the understanding of cosmic ray shower physics. [7]

TOTEM

The TOTEM detector is designed to detect protons from elastic and diffractive scattering and measures the pp cross section at small angles. [8]

2.2. The Compact Muon Solenoid

The CMS detector is, despite its name, one of the largest high energy experiments ever build. It is 21.6 m long, has a diameter of 15 m and a mass of

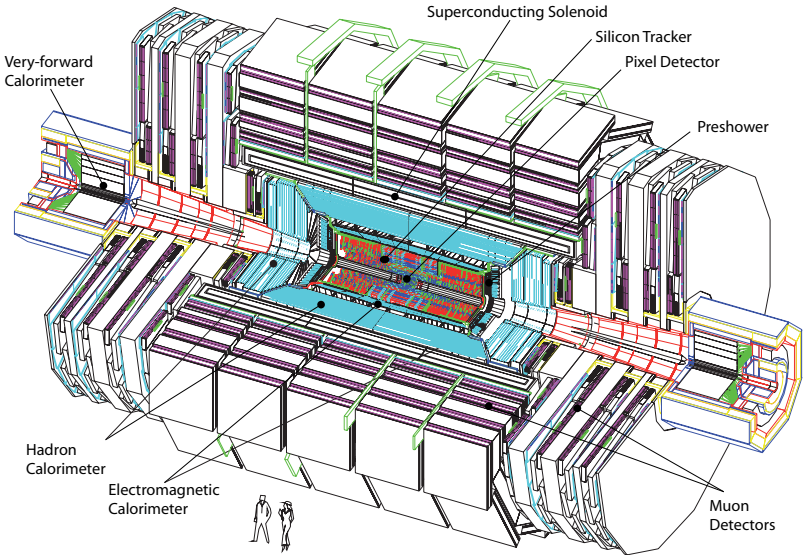

Figure 2.2.: Cut of the CMS detector with its different compontents. [9]

about 12,500 metric tons. The general detector layout is similar to other multi-purpose concepts. This onion layer like structure can be seen in figure 2.2. One of the main goals of the LHC experiments is the search for the Higgs boson. Some Higgs discovery channels were driving design decisions for the high quality electromagnetic calorimeter and the good muon resolution, are discussed in section 3.3. In the present chapter a short description of the main detector parts is given, following the structure from inside out. The resolutions achieved with the detector parts are discussed.

2.2.1. Vertex Detector

The first part of the CMS detector around the beam pipe is the silicon pixel vertex detector, which provides three dimensional measurements of charged particle tracks. A schematic view of the detector is given in figure 2.3.

The barrel part covers the pseudorapidity range of $|\eta| < 2.2$ and consists of three layer of silicon pixel sensors at distances of 4.3 cm, 7.2 cm and 10 cm. In the endcap two layers at a z position of 32.5 cm and 46.5 cm extend the range to $|\eta| < 2.5$. In total the vertex detector has a total area of 1 m^2, corresponding to 50 million pixels. One of the building pixel modules is shown in figure 2.4. Details about the achieved resolutions are discussed in section 6.2.

The main function of the vertex detector is providing such a good track resolution that those can be grouped into or assigned to single vertices. This is for example important for the proper tagging of b-type jets, as will be explained in section 6.6.

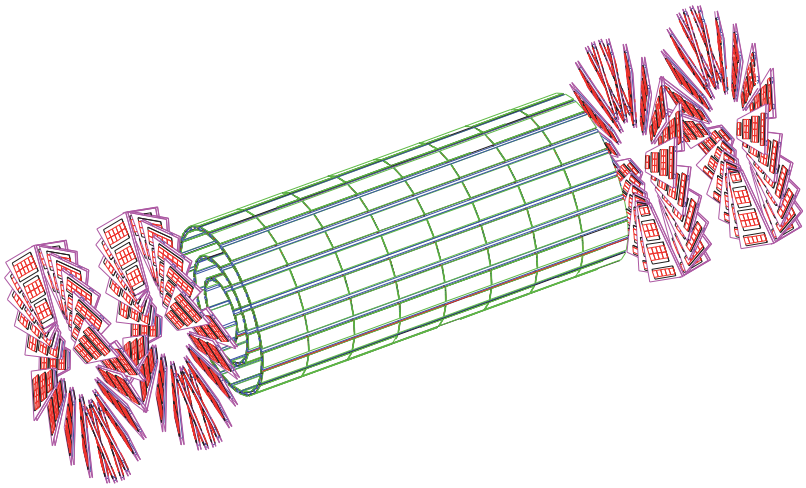

Figure 2.3.: Sketch of the CMS silicon pixel vertex detector. Though all three barrel layers are shown here, only two will be used simultaneously during the different phases of operation. [10]

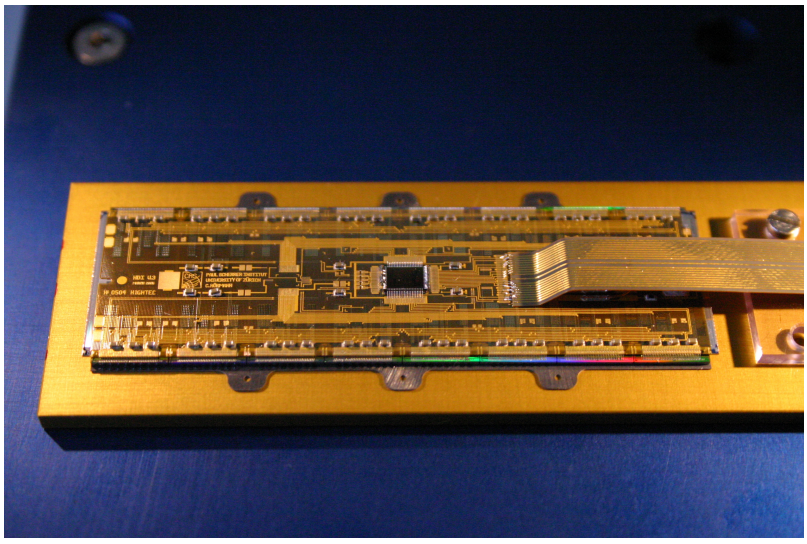

Figure 2.4.: Picture of a CMS Pixel Module. The pixels have a pitch of $100 \times 150\,\mu\mathrm{m}^2$. [9]

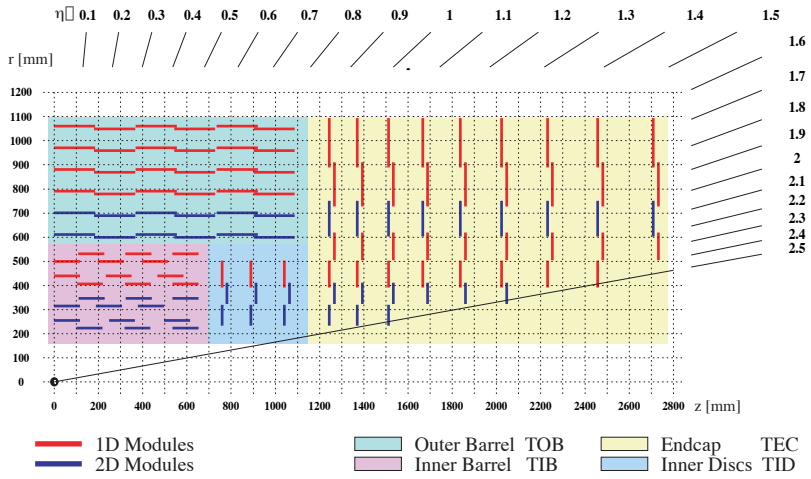

Figure 2.5.: A quarter view of the tracking detector. The different parts of the detector are indicated by colour. The lines represent the silicon modules, which are either single sided (red) or double sided (blue).

2.2.2. Tracking system

The tracking system of CMS is entirely based on silicon technology. In total 24,244 silicon strip sensors cover a sensitive surface of 198.34 m^2. [11, 12, 13]. Because of the high radiation dose of 1.6×10^{14} 1-MeV-equivalent neutrons per cm^2 in the inner region, the tracker needs to be cooled down to $-10°C$ to minimize the radiation damage. Details about tests of radiation hardness can be found in [14].

The overall size of the tracker is 280 cm in $|z|$ direction and the radius r ranges from 20 to 120 cm. It is segmented in four main parts – the Tracker Inner Barrel (TIB), the Tracker Outer Barrel (TOB), the Tracker Inner Disks (TID) and the Tracker Endcaps (TEC). The barrel part covers the pseudorapidities up to 0.9, the end cap part up to $|\eta| = 2.5$ (see figure 2.5). Depending on η a particle passes between 8–14 layers. Details on the overall tracker layout can be found in [15, 16].

Resolution

Combining the measurements from the silicon vertex and the silicon pixel detector the momentum resolution for isolated tracks in the barrel region of $|\eta| \leq 1.6$ is given by:

$$\Delta p_T / p_T \simeq (15 \cdot p_T \oplus 0.5)\% \quad (p_T \text{ in TeV}). \tag{2.1}$$

2.2.3. Electromagnetic Calorimeter

One of the design goals of CMS was a high quality electromagnetic calorimeter (ECal). In particular the $H \rightarrow \gamma\gamma$ channel as described in section 3.3 was chosen as performance measure.

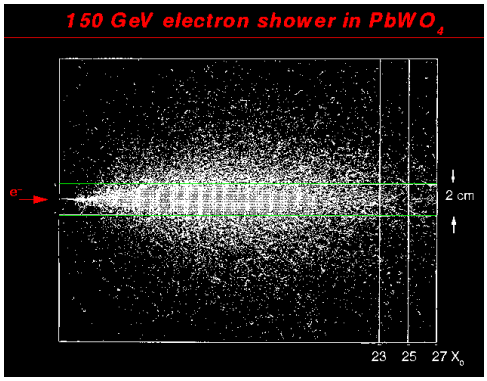

Figure 2.6.: Simulation of a shower caused by an 150 GeV electron stopped in $PbWO_4$. The green lines indicate the size of the crystals used in CMS. Source: Based on [17]

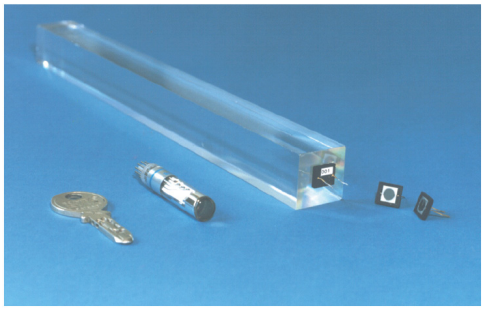

Figure 2.7.: Picture of a CMS Ecal crystal. The scintillation light is collected and amplified by avalanche photodiodes.

The entire CMS ECal is build from one layer of lead tungsten scintillator crystals ($PbWO_4$). The advantages of lead tungsten are the radiation hardness and the fast scintillating process, where in only 20 ns already 80% of the light is emitted. This significantly reduces the interplay of multiple bunch crossings which happen every 25 ns. Another advantage is the short radiation length of $X_0 = 0.89$ cm and a Molière radius of only 2.2 cm. Figure 2.6 showhs the simulation of a shower in the used material. The size of the crystal matches these properties. In the barrel region the front face is $2.2 \times 2.2\,\mathrm{cm}^2$ and and $2.86 \times 2.86\,\mathrm{cm}^2$ for the endcap. They are almost $26X_0$ deep, which translates to 230 mm and 220 mm in barrel and endcap respectively. A picture of such a crystal is shown in fig. 2.7.

In total 61,200 crystals in the Ecal barrel (EB) and 14,648 in the endcap (EE) are mounted in a quasi projective geometry and cover an η region up to 3.0. The size of the crystals translates to a lateral granularity of $\Delta\phi = 0.0175 \times 0.0175$. A tilt of 3 degree in η and ϕ with regard to the primary vertex reduces the leakage due to inter-crystal gaps. An r-z-view of the ECal is shown in figure 2.8. The inner radius of the EE is about 129 cm, and the EE located at a distance of 314 cm from the interaction point.

In front of the EE a lead-silicon preshower detector is located. It is required to increase the π_0 rejection, where two very close photons have to be separated. Due to its 3 radiation lengths of thickness, the crystals in the endcap could be made shorter than in the barrel.

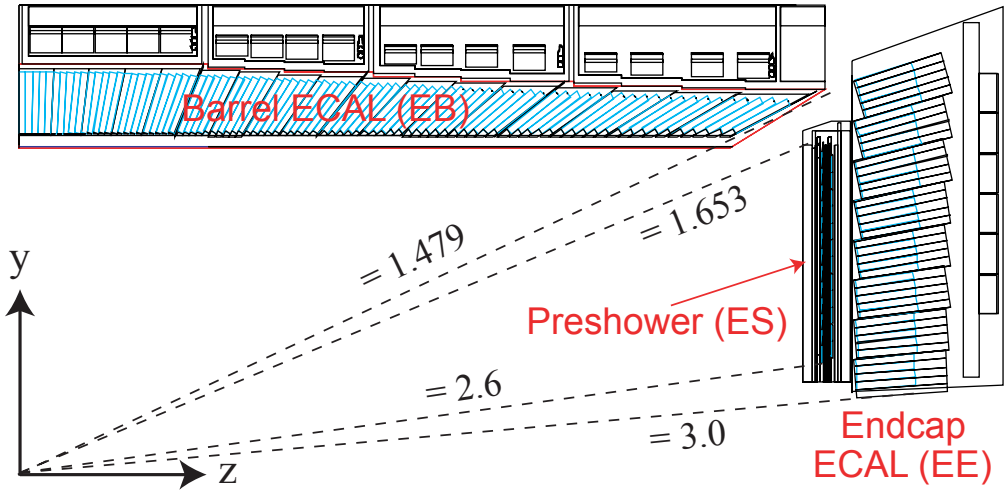

Figure 2.8.: An r-z-view of the CMS electromagnetic calorimeter. The ECal consists of three parts, the barrel, the preshower and the end cap. All crystals are mounted in quasi projective geometry.
Source: Based on [9]

Resolution

The ECAL reaches an energy resolution which can be parameterized as follows:

$$\left(\frac{\Delta E}{E}\right)^2 = \left(\frac{S}{\sqrt{E}}\right)^2 + \left(\frac{N}{E}\right)^2 + C^2 \tag{2.2}$$

The single terms in formula 2.2 are the stochastic contribution S, related to e.g. the shower profile, the electronic noise N and the constant offset C, which is caused be e.g. rear leakage, other geometrical effects or cracks. Test beam measurements with electrons of 20 – 250 GeV/c have been used to estimate the actual values. The stochastic term is in the order of 2.8%, the noise N about 127 MeV and 213 MeV for 3×3 and 5×5 blocks respectively. Finally the offset C was found to be 0.3%. For electrons at 100 GeV a relative resolution of around 0.5% can be achieved. Further details can be found in [18].

2.2.4. Hadronic Calorimeter

The hadronic calorimeter (HCAL) is the last subdetector placed inside the magnet coil. Like the other detector parts, it consists of a barrel (HB) and an end cap (HE). Some parts of the barrel are supported by the HCal outer (HO) system. A schematic view is shown in figure 2.9. To complete the hermiticity there is an additional forth part outside the magnet. The hadronic forward (HF) calorimeter is placed around the beam pipe 6 m from the primary vertex. In this section only a brief overview of the single components is given. A detailed description of the HCal system can be found in [19].

The HB covers the pseudorapidity range up to $|\eta| < 1.4$. It is realized as copper alloy calorimeter in the radius range of 1.8 – 2.9 m. Layers of plas-

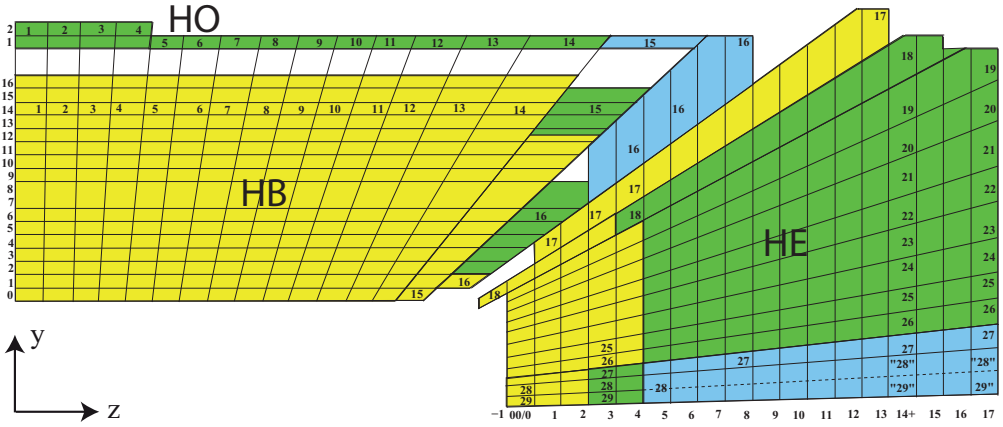

Figure 2.9.: Quarter view of the hadronic calorimeter in the r-z-plane. Shown are the hadron barrel (HB), the hadron outer (HO) and the hadron end cap (HE) calorimeter with their projective geometry.
Source: Based on [9]

tic scintillator tiles between the 5 cm thick absorber material are read-out via wavelenght shifting fibres. The scintillator tiles have a fine granularity of $\Delta\eta \times \Delta\varphi = 0.087 \times 0.087$ (corresponding to a block of 5×5 crystals in the ECal) to provide a good di-jet separation and are aligned in a projective geometry building so-called towers. The calorimeter thickness of 15 absortion layers or 75 cm in the barrel corresponds to about five nuclear interaction lenghts. Since these interaction lengths of the hadronic barrel are not sufficient for a full shower containment one or two additional scintillator layers are placed outside the solenoid serving as tail catcher. This outer hadron calorimeter (HO) completes the calorimeter in the barrel region.

The two hadronic endcaps are build from each 2304 towers which are 19 scintillator layers deep and cover the pseudorapidity region $1.3 < |\eta| < 3.0$. The η range up to $|\eta| = 1.74$ is segmented into towers with a $5^\circ\varphi$ and 0.087η segmentation. The region up to $|\eta| = 3$ is segmented into $\Delta\varphi = 10^\circ$, whilst $\Delta\eta$ ranges from 0.09 to 0.35. As material steel absorbers and quartz fibers parallel to the beam are chosen.

Resolution

Combining the information of the electromagnetic calorimeter and the hadronic calorimeter the following energy resolution in the range $30\,\text{GeV} < E < 1\,\text{TeV}$ can be achieved:

$$\frac{\Delta E}{E} = \frac{1}{\sqrt{E}} \otimes 0.045 \quad (\text{E in GeV}). \tag{2.3}$$

The initial calibration for the barrel prior to start up is expected to be in the order of 4%. [19, 20]

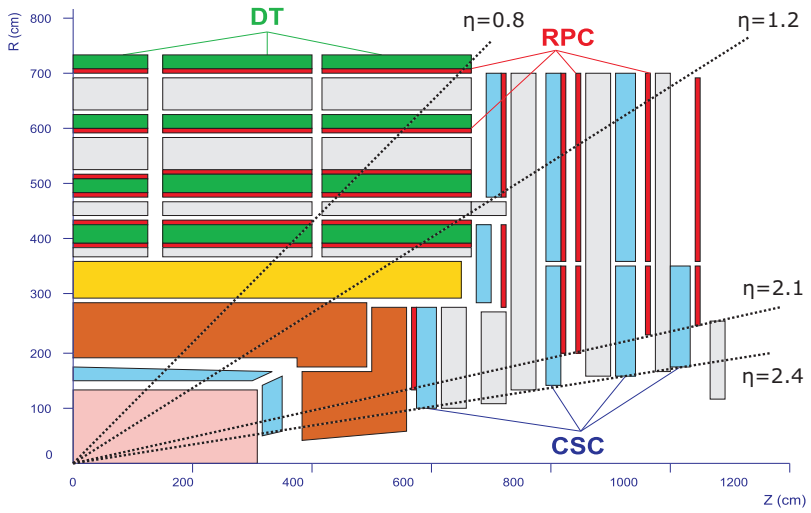

Figure 2.10.: CMS muon system cross section. Three different detector types are used. Drift tubes (DT), Cathode Strip Chambers (CSC) and Resistive Plate Chambers (RPC).

2.2.5. Superconducting Magnet

To measure the momentum of charged particles the method of choice is applying an external magnet field and measuring the bend trajectory. The magnetic configuration of CMS is chosen as a strong solenoid field of about 4 Tesla, which became part of the experiment's name Compact Muon Solenoid. It is created by a 12.5 m long, 5.9 m wide (inner diameter) and 225 t heavy superconducting magnet of a temperature of 4.5 K. Consisting of 2,168 turns of aluminium reels it conducts a current of 19,500 A at design field intensity. This yields to a total field energy of 2.7 GJ. [21]

2.2.6. Muon Spectrometer

Outside the solenoid the second eponymous part of the detector is located, the muon system. As for the ECal there exists one design performance channel, which is the $H \rightarrow 4l$ channel as descriped in section 3.3.

Similar to other detector subsystems it is separated into a barrel and an end cap part. The barrel is located in the gaps of the iron return yoke. The two end caps are mounted on each three wheels. This setup ensures that muon system can benefit from the returning magnetic flux. A schematic overview is given in figure 2.10.

Three different detector types are used in the muon system. In the barrel region standard *drift tubes* (DT) are inserted. This type of detector is possible because of the low magnetic field in the gaps of the return yoke. Furthermore both the muon signal and the background rate from neutrons are expected to be low. The 250 drift tubes on 5 rings are packs of aluminium covered, gas filled cells. A single cell is 13 cm high, 42 cm wide, and 2–3 m long, containing a central anode wire. On pass of a charged particle the wire collects the

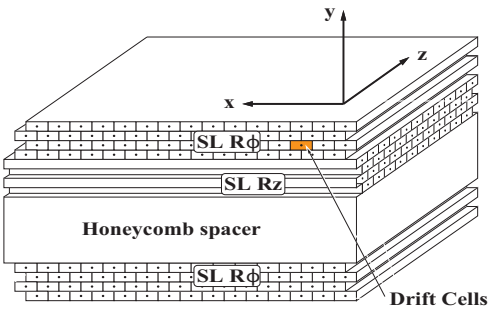

Figure 2.11.: Cross section of a CMS drift tube. It consists of three superlayers of each four layers. The outer superlayers are aligned along the beam line. The middle one is rotated by 90 degree to measure the z coordinate. Source: [9]

ionization charges and a signal can be read out. A standard DT has three cell superlayers of each four layers (figure 2.11). (n the outer part of the muon system there are DTs with only two superlayers. As can be seen the anode wires of the outer superlayers are along the beam line to measure the r and ϕ coordinate. For a measurement of the z coordinate the middle superlayer is rotated by 90 degree. It is designed to a precision better than 100 μm as spatial resolution and 1 mrad for ϕ.

The forward region is more challenging in terms of environment and occupancy. The chosen technology are cathode-strip chambers with each six gas layers. In total 468 of these are grouped in four stations (ME1–ME4) with each two concentric rings.

Cathode strips and a perpendicular plane of anode wires provide a two dimensional resolution. The CSC is working in electron avalanche mode. A fast shower is collected by the anode wires, while a slightly slower image charge traverses to the cathode strips. Using both informations the spatial resolution is in the order of 200 μm, the ϕ resolution about 1 mrad.

To allow fast triggering the DTs and CSCs are accompanied by resistive plate chambers (RPC). A chamber is basically build of two high-resistive bakelite plates with a small gap of a few milimeters filled with gas.When a high voltage is applied, ionizing particles traversing the gas volume trigger an avalanche cascade which then can be registered in the read-out electronics. The position of the RPCs with regard to the other parts of the muon system is shown in figure 2.10.

Resolution

Taking multiple scattering in the massive detector parts, misalignment and uncertainties on the magnetic field into account, the combined tracker and muon system provides the following muon resolution [9]:

$$\frac{\Delta p_T}{p_T} = 0.045\sqrt{p_T} \quad (p_T \text{ in TeV}). \tag{2.4}$$

A more detailed discussion on the muon reconstruction efficiency is given in section 6.3.

2.2.7. Trigger system

The design bunch crossing rate of LHC is about 40 MHz. Compared to the computer facilities that are designed to store event data at a rate of 100 Hz the trigger will reduce the number of events by a factor of 4×10^8. To achieve this there are two trigger steps in CMS – the Level 1 (L1) and the High Level Trigger (HLT).

The L1 trigger

The L1 trigger is build from flexible configurable hardware based on FPGAs (Field Programmable Gate Array). The input for the L1 trigger decision are information from muon and calorimeter readout. In the ECAL and HCAL a total of 4176 trigger towers provide energy values at a frequency of 40 MHz. In the muon system the fast RPCs help assigning the signal to the right bunch crossing. Together with the DT and CSC data it is combined in the global muon trigger.

At the end of the L1 trigger the results of 128 different trigger paths are combined to one single bit deciding if the event is fully read out or thrown away. The design output rate is in the order of 100 kHz.

One of the main problems for the L1 trigger are signal transportation times. In total the signal propagation and the data processing sum up to a trigger signal delay of 3.2 µs or about 128 bunch crossings. This is the time data has to be stored inside the data pipelines of each single readout channel. More information on the L1 trigger system can be found in the first part of the TriDAS technical design report [22].

The HLT trigger

The next trigger level is entirely software based and applies the same algorithms as used for the final reconstruction. The software runs on a computing farm build from standard computer and processor technology. This allows full flexibility for later updates to new developed IT technology. Currently the setup consists of about 1000 processors connected via a high bandwidth switching network with a throughput of 100 Gb/s.

From the processing point of view the HLT is separated into three stages - level 2, level 2.5 and level 3. Where level 2 uses calorimeter and muon information only, level 2.5 includes some tracking information and finally level 3 accesses all detector information. Since the time for a trigger decision is between 40 ms and 1 s common random access memory is sufficient for event buffering.

The output of the HLT are single bit decisions for different event patterns. The total output will be about 100 Hz, which means a data reduction factor of

10^3 compared to the L1 output. Still a total of 10 TBytes event data per day will be stored. [23, 24]

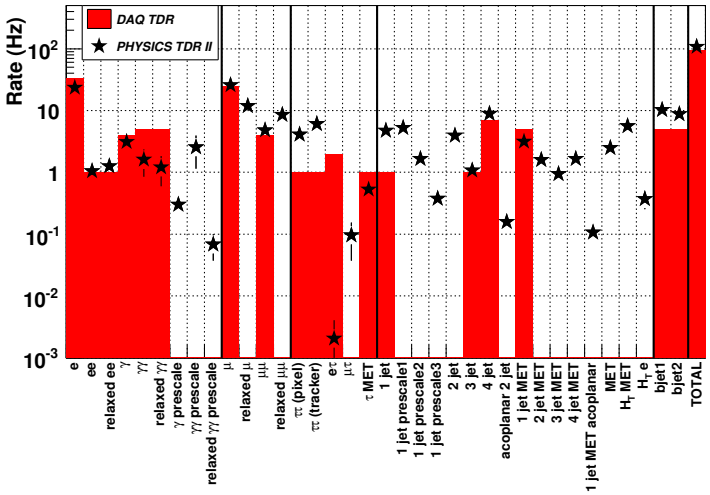

Figure 2.12.: The bandwidths for the different trigger paths. Source: [9]

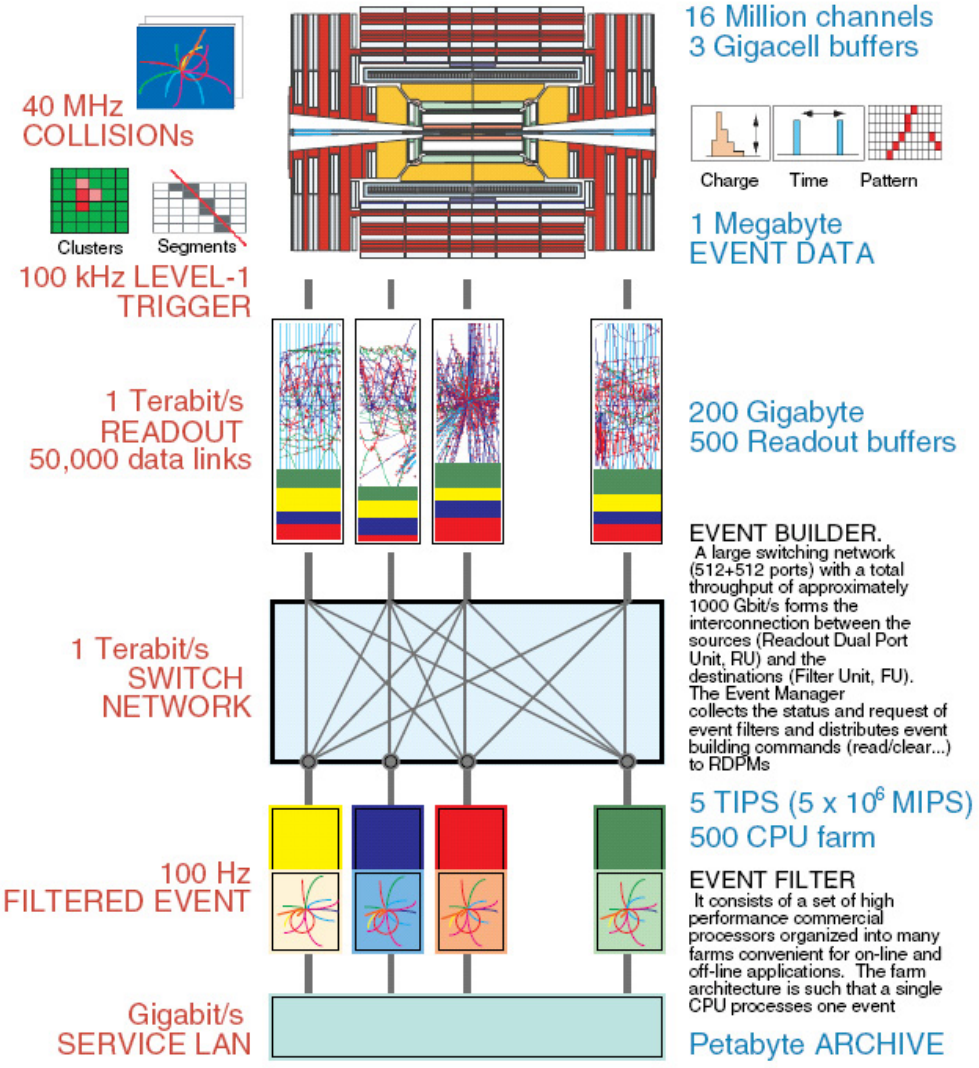

Figure 2.13.: A schematic view of the trigger system.

3. Physics at the LHC

First some general remarks to proton–proton collisions are given. It is followed by a short summary on the Standard Model (SM) of Particle Physics. One of the design goals of the LHC is the search for the Higgs boson. Promising search strategies which had a big impact on design choices for the CMS experiment are briefly explained. Even if the SM is very successful in explaining the present experimental results to a very precise level, it has several shortcomings, of which are some mentioned. Finally, the chapter is completed by a short outlook to possibilities beyond the current Standard Model.

3.1. Proton–Proton-Collisions

The total cross section for the inelastic $p - p$ scattering at LHC will be about 55 mb. For the low luminosity phase of $10^{33}\mathrm{m}^{-2}\mathrm{s}^{-1}$ this translates into an interaction rate of $R = \sigma_{tot} \times L \approx 0.55 \cdot 10^{8}\mathrm{Hz}$. Most of these interactions are soft interactions, i. e. large distance collisions between the two protons, where the transverse momentum exchanged between the two protons is such small, that most of the energy escapes along the beam pipe.

The more interesting events are hard interactions, in which the inelastic scattering between the two protons can be treated as direct parton–parton scattering. Since the interacting partons (quarks or gluons) do not carry the whole proton energy they enter the hard process only with momentum fractions x_1 and x_2, Thus the center of mass energy of the interaction is only a fraction of the total energy:

$$\hat{s} = \sqrt{x_1 x_2 s}. \tag{3.1}$$

The probability for a parton of type i to carry the momentum fraction x is given by the parton density functions (PDF) of the proton

$$f_i^P(x, Q^2), \tag{3.2}$$

with Q^2 as the exchanged four momentum square. As a result the cross section of the scattering process can be written as:

$$d\sigma = \int_0^1 dx_1 \int_0^1 dx_2 f_1(x_1, Q_F^2) f_2(x_2, Q_F^2) d\hat{\sigma}(Q_F^2). \tag{3.3}$$

The scale Q_F^2 sets the separation between the calcuable hard pertubative parton interaction and the effects in the proton, which are parameterized by the experimentally derived parton density functions.

3.1.1. PDFs

Currently the best global parton density descriptions are provided by the CTEQ and the MRST group. The main experimental input are both results from proton–electron collisions at HERA and fixed target experiments where neutron–nucleon scattering is measured. To desribe these data MRST applies a fit of 15 parameters and CTEQ uses a set of 20 parameters. In this thesis the CTEQ5L parameterization was used for most of the event simulation. [25]

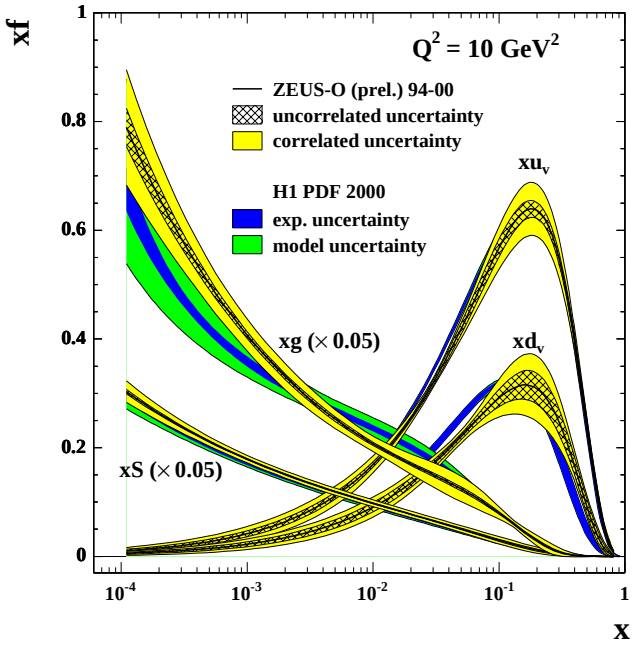

Figure 3.1.: Parton density functions. Here a comparison of ZEUS and H1. Shown are the density of u and d valence quarks, gluons and sea quarks. [26]

3.1.2. Underlying Event

After the hard interaction from both protons a coloured remnant that did not take part in hard interaction itself is left over. Furthermore multiple hard interactions can occur within one collision. These two effects are subsumized under the term *underlying event* [27]. Fragments of the underlying event can influence the study of the hard process (see section 7.10.2).

3.1.3. Pile-up

Due to the luminosity at LHC it is not unlikely that multiple independent hard interactions happen during one bunch crossing. The additional processes are called *pile-up events* and are a major challenge to many of the physics studies

at LHC. For example the beams at the LHCb interaction point need to be defocussed during the high luminosity phase to allow sensible studies [6]. During the low luminosity phase one expects about 3.5 pile-up events per hard interaction at CMS. It has to be noted that the uncertainty to this assumption is quite high and thus has to be taken into account for systematic uncertainties (see 7.10.2).

3.1.4. Expected Cross Sections

Figure 3.2 shows the extrapolation of various cross sections to the LHC. While the total cross section increases only little with regard to Tevatron, many interesting processes have a much higher increase. One for example is the top production, which increases significantly stronger than the relevant backgrounds (W,Z). The cross sections used for Monte-Carlo studies by the CMS collaboration and in the present study are given in [28] and table 7.1.

3.2. The Standard Model of Particle Physics

The current knowledge of particle physics is combined in the so-called *Standard Model of Particle Physics* (SM), which will be explained briefly.

The known matter consists of three generations of spin $\frac{1}{2}$ fermions, which are given in table 3.1. Each generation consists of a right handed singlet and

Table 3.1.: The three families of leptons and quarks of the Standard Model. Q denotes the electric charge,T_3 the weak isospin and Y the hypercharge.

	1	2	3	Q[e]	T_3	Y	Colour
Quarks	$\begin{pmatrix} u \\ d' \end{pmatrix}_L$	$\begin{pmatrix} c \\ s' \end{pmatrix}_L$	$\begin{pmatrix} t \\ b' \end{pmatrix}_L$	$2/3$ $-1/3$	$1/2$ $-1/2$	$1/3$ $1/3$	rgb rgb
	u_R	c_R	t_R	$2/3$	0	$4/3$	rgb
	d_R	s_R	b_R	$-1/3$	0	$-2/3$	rgb
Leptons	$\begin{pmatrix} \nu_e \\ e^- \end{pmatrix}_L$	$\begin{pmatrix} \nu_\mu \\ \mu^- \end{pmatrix}_L$	$\begin{pmatrix} \nu_\tau \\ \tau^- \end{pmatrix}_L$	0 -1	$1/2$ $-1/2$	-1 -1	$-$ $-$
	$\nu_{e,R}$	$\nu_{\mu,R}$	$\nu_{\tau,R}$	0	0	0	–
	e^-_R	μ^-_R	τ^-_R	-1	0	-2	–

a left handed doublet of the weak isospin. Not shown are the antiparticles, which are simple copies of the shown particles, only they differ in sign for all additive quantum numbers. From these particles only the first generation is present in the matter around us. Up to now there is now evidence for a fourth generation of fermions. Furthermore, the number of lepton generations with

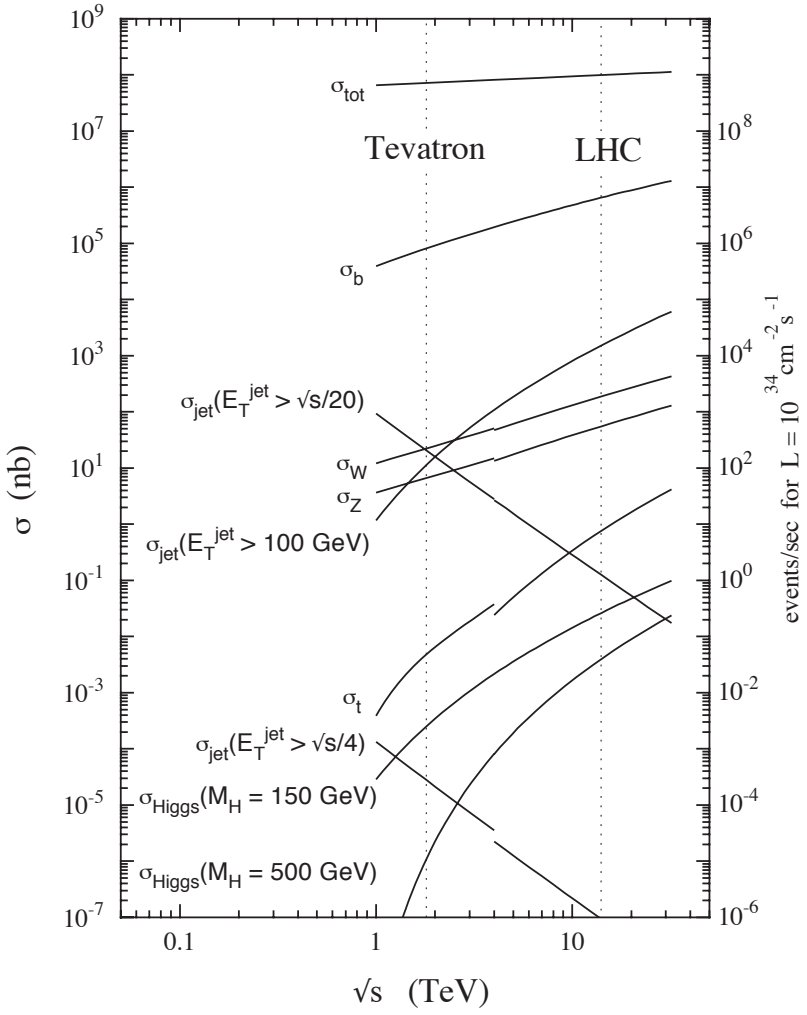

Figure 3.2.: Cross sections and event rates for some characteristic standard model processes as function of the center of mass energy. Two lines indicate the proton–antiproton collider Tevatron and the proton–proton collider LHC. Source: [29]

light neutrinos is determined to be three by the LEP experiments [30]. One of the quarks shown in the table – the top quark – is of special interest for LHC studies. Details about the physics of the top quark at LHC will be discussed in chapter 4.

Interactions between the fermions happen through the exchange of spin-1 bosons, shown in table 3.2, which are directly connected to the fields of the three fundamental interactions, namely the electromagnetic, the weak and the strong force. The mathematical representation of these fields is a gauge theory

Table 3.2.: The gauge bosons in the standard model.

Boson	Interaction	Charge	Mass
γ (Photon)	electromagnetic	0	0
Z^0	weak	0	91.2 GeV
W^+, W^-	weak	$+1e$, $-1e$	80.4 GeV
8 g_i	strong	(r,g,b)	0

with the combined group $SU(3)_C \times SU(2)_L \times U(1)_\gamma$. A great success of this formalism was the unification of the electromagnetic and the weak force to the electroweak interaction. The fourth fundamental interaction, gravity, is not yet included in the theoretical framework. Though its strengths is not relevant for the processes under study here, this fact is a major theoretical drawback (see section 3.4).

An important aspect of the weak interaction is the fact, that the mass eigenstates for quarks are different from the weak eigenstates. The mixing is given by the Cabbibo-Kobayashi-Maskawa (CKM) matrix [31, 32]:

$$\begin{pmatrix} d' \\ s' \\ b' \end{pmatrix} = \begin{pmatrix} V_{ud} & V_{us} & V_{ub} \\ V_{cd} & V_{cs} & V_{cb} \\ V_{td} & V_{ts} & V_{tb} \end{pmatrix} \begin{pmatrix} d \\ s \\ b \end{pmatrix} \tag{3.4}$$

This is needed to explain flavour changes during weak interactions. Present results of neutrino oscillations indicate that a similar matrix for the neutrino states exists.

3.3. The Higgs-Boson

It is known, that the particle masses in the Standard Model are strongly connected to the so-called "Higgs mechanism", which induces the spontaneous symmetry breaking in the electroweak sector. Apart from giving a mechanism for explaining the masses (directly for the gauge bosons, indirectly for the fermions) it requires a new scalar boson, the Higgs boson. A free parameter of the model is the mass of the Higgs itself. Theoretically it can only be bound to a mass below or in the TeV range, which is induced by the requirement of

unitarity. One of the performance goals of the CMS and ATLAS experimental design is the search for this Higgs boson. According to the expected higgs branching ratios as shown in figure 3.3, the search can be roughly devided into three mass ranges which will be shortly explained. [33]

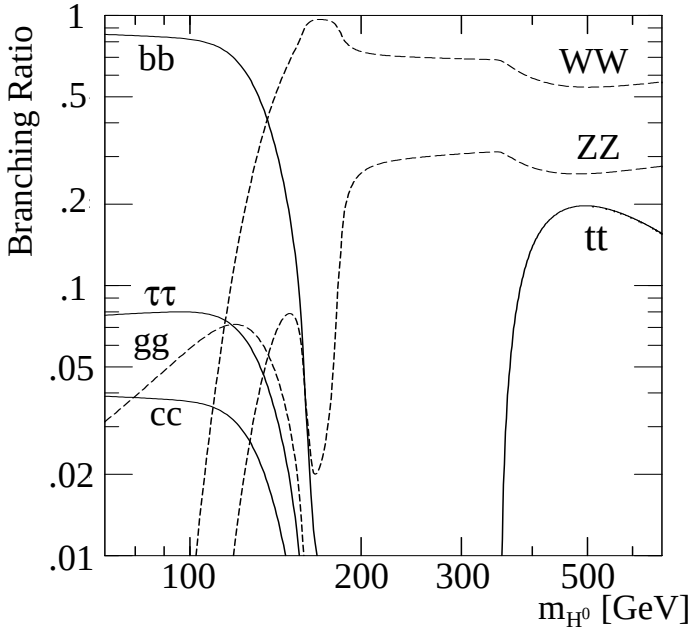

Figure 3.3.: Branching rations for different decay modes of the SM higgs. According to these ratios there exist different search strategies for different mass regions.

Low mass region: For masses below 130 GeV the dominant decay mode is $H \to b\bar{b}$. Since the overall $pp \to b\bar{b}$ cross section is 10^7 times higher the possible Higgs signal would be completely hidden in the background, and one has to go for non-hadronic decay modes. The most promising channel is $H \to \gamma\gamma$. Even if it has a low branching ratio of 10^{-3}, it has a relatively low background. Though the irreducible background is still bigger than the signal, it should be visible as peak above the continous background. Here the CMS detector should perform particulary well in this channel as it is one of the performance benchmarks of the overall detector design. As second possibility in this mass region there is the associate Higgs production. [33]

Intermediate mass region: For masses between 130 GeV and $2m_Z$ the best suited channels are $H \to ZZ^* \to 4l$ and $H \to WW^* \to 2l2\nu$. The former has a very clear signature of 4 leptons in the final state and especially the 4 muon case is again a performance channel for the CMS design.

High mass region: In the region above $2m_Z$ the four lepton channel becomes completely on-shell and gives an almost background free signature. Again

the $H \to ZZ \to 4\mu$ channel is the most promising one. Figure 3.4 shows a simulated signal in this channel.

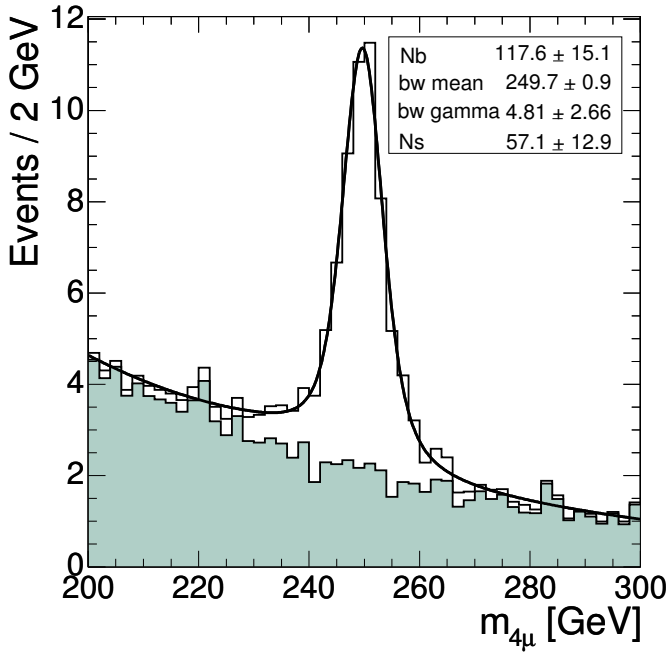

Figure 3.4.: Simulated higgs signal in the four muon channel. It can be seen as peak above the continous background. This channel is one of the performance channels for the CMS detector design. [33]

3.4. Problems of the Standard Model

For all measurements done in collider experiments, the Standard Model provides astonishingly precise predictions and results. Still several shortcomings of the Standard Model let us belief that there will be new physics discovered in the energy range of LHC. The SM will then be an effective theory of some bigger theory. Without going into detail about the candidates for SM replacements or extensions, some of the Standard Model problems have to be mentioned:

Higgs boson Despite long searches for the Higgs boson, it has not been found yet. Though the simplicity and elegance of the Higgs mechanism is sort of esthetical advantage, there is no strong reason that there cannot be another explanation for the electroweak symmetry breaking.

Matter–Antimatter-Asymmetry Cosmological surveys lead to the observation of an asymmetry between matter and antimatter. This asymmetry is e. g. constrained by the measurements of primordial cosmic rays. Theories explaining this effect require a CP violation that is much higher

than it is possible in the Standard Model. Furthermore they lead to baryon-number violation, while the baryon number is strictly conserved in the Standard Model. A baryon-number violating effect would be for example the proton decay. The current limit on the proton lifetime is $\tau_{proton} > 1.9 \cdot 10^{-29} a$, and thus too big for those theories. [34]

Dark matter Studying galaxy rotations one finds that the distribution of the visible mass can explain the dynamics only partially. This is only one of the many evidences for non-baryonic and neutral matter, the so-called dark-matter. Even if unknown what this matter is built of, there exist estimations for its amount. Unfortunately massive right-handed neutrinos are ruled out as explanation because of the low upper mass constraint. [35]

Gravity Still the first of all discovered forces is not included in the Standard Model – Gravity. There are many efforts building a *theory of everything*. Using the mechanism of quantum field theories, the natural representation of the field tensor is a gauge boson with spin-2, called graviton. But adding this to the Standard Model destroys renormalizability. Briefly spoken, the Standard Model cannot be the last answer.

3.5. Beyond Standard Model

A possible candidate for replacing the Standard Model is the concept of Supersymmetry (SUSY). The basic idea is a symmetry operation translating fermions into bosons and vice versa. It is able to solve the hierarchy and the fine tuning problem. The postulated symmetry operation results in one additional *sparticle* for each known particle. None of the known particles could be identified as supersymmetric pairs, thus the number of particles doubles [36]. Because SUSY predicts that the supersymmetric partners have the identical mass and since none of the sparticles have been observed, the supersymmetry must be a broken symmetry. There are multiple models to achieve this. One of the more prominent ones is the MSSM (Minimal Supersymmetric Standard Model). If this theory is realised in nature, the newly predicted particles will not be above the TeV range and thus discoverable at the LHC. These new particles are very promising candidates for the dark matter. In case the number of particles and sparticles is conserved (R parity), there must be at least one stable supersymmetric particle.

4. Top Quark at the LHC

The top quark was discovered as last of the six quarks at the Tevatron in 1995 [37, 38] and is the heaviest elementary particle known. With the current mass estimate of

$$m_{top} = 170.9 \pm 1.1(\text{stat.}) \pm 1.5(\text{sys.}) \text{ GeV} \tag{4.1}$$

it has a mass which is 35 times bigger than the next heavy quark [39]. Because of this high mass the production of top quarks was not possible before Tevatron and most measurements are still statistically limited. At LHC the production rate of top quarks will be much higher (see section 4.1) and it will be possible to use the top quarks for more precise measurements.

Being at a different mass scale than the other quarks, the top quark offers some unique possibilities. One is the study of the spin of a bare quark, which is the topic of this thesis. The theoretical foundations will be explained later in this chapter.

Besides being of interest of its own the top is strongly connected to other physics. In radiative corrections the top and the W mass give a limit to the Standard Model Higgs boson, which is compatible with current measurements. This is shwon in figure 4.1.

For further reading an extensive review of current top physics at Tevatron and prospects for the LHC are given in [40, 41].

4.1. Pair Production Processes

At hadron colliders the main $t\bar{t}$ production modes are gluon–gluon fusion and quark–antiquark annihilation, which are

$$q(p_1) + \bar{q}(p_2) \rightarrow t(p_3) + \bar{t}(p_4) \tag{4.2}$$

and

$$g(p_1) + g(p_2) \rightarrow t(p_3) + \bar{t}(p_4) \tag{4.3}$$

with p_i being the parton four-vectors. The corresponding Feynman diagrams in first order are shown in figure 4.2 and the matrix elements at leading order (LO) are

$$\begin{aligned} |\overline{\mathcal{M}}|^2(gg \rightarrow t\bar{t}) =& (4\pi\alpha_s)^2 \times \left(\frac{(p_1+p_2)^4}{24(p_1\cdot p_3)(p_2\cdot p_3)} - \frac{3}{8} \right) \\ & \times \left(4\frac{(p_1\cdot p_3)^2 + (p_2\cdot p_3)^2}{(p_1+p_2)^4} + \frac{4m_t^2}{(p_1+p_2)^2} - \frac{m_t^4(p_1+p_2)^4}{(p_1\cdot p_3)^2(p_2\cdot p_3)^2} \right) \end{aligned} \tag{4.4}$$

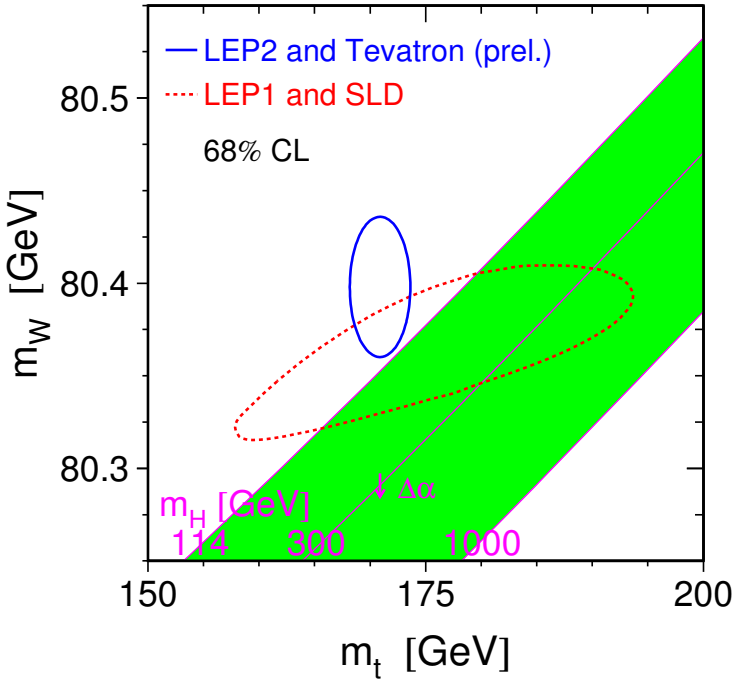

Figure 4.1.: Limit to the Higgs mass from radiative corrections. The contours are the experimental mass limits obtained from direct and indirect measurements from SLD, LEP and Tevatron. The band indicates the higgs masses which are compatible with the SM. [30]

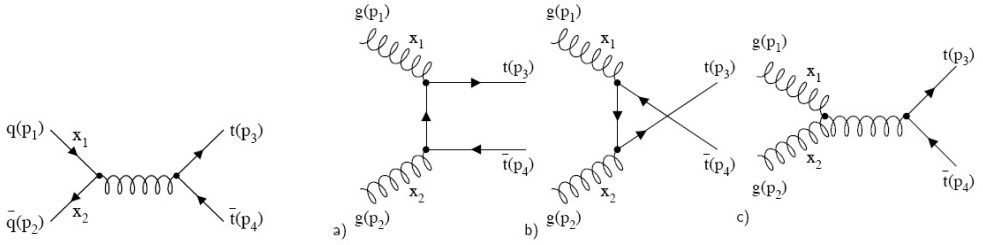

Figure 4.2.: Feynman diagrams of the production processes of $t\bar{t}$-pairs at a proton–proton-collider.

for the gg fusion, and for the $q\bar{q}$ annihilation:

$$|\overline{\mathcal{M}}|^2(q\bar{q} \to t\bar{t}) = (4\pi\alpha_s)^2 \times \frac{8}{9}\left(2\frac{(p_1 \cdot p_3)^2 + (p_2 \cdot p_3)^2 + (p_2 \cdot p_3)^2}{(p_1 + p_2)^4} + \frac{m_t^2}{(p_1 + p_2)^2}\right) \tag{4.5}$$

Recalling the kinematics of proton-proton collisions (chapter 3.1) the differential cross section for the $t\bar{t}$ production becomes:

$$d\sigma = \int\int dx_1 d_x 2 f_1(x_1, Q^2) f_2(x_2, Q^2) d\hat{\sigma} \tag{4.6}$$

Slightly above the energy threshold of $2m_t$ the on-shell production reaches its maximum. With a center of mass energy of 14 TeV the gluon density of the PDF is much higher than the quark density and thus approx. 90% of the production is done via gg fusion and only 10% via $q\bar{q}$ annihilation. For Tevatron the situation is almost reversed and there $q\bar{q}$ annihilation dominates. At LHC, the leading-order cross section is 560 pb, in next-to-leading-order 830 pb. This translates to almost one top-pair per second at CMS. Thus it is legitimate to call LHC a top factory.

For the sake of completeness it has to be mentioned, that single top production is almost as likely. Details can for example be found in [42].

4.2. Top Decay

In theory the top quark can decay weakly into any quark with a charge of -1/3 (d, s, b) and an on-shell W-boson. The branching ratio for the different modes can be calculated using the CKM matrix elements. For the mode $t \to Wb$ it reads:

$$B_b = \frac{|V_{tb}|^2}{|V_{td}|^2 + |V_{ts}|^2 + |V_{tb}|^2}. \tag{4.7}$$

With the current experimental data we have $|V_{tb}|$ close to one and it turns out that all other channels are almost completely suppressed with regard to this one. Because of their long lifetime the two b-quarks build hadronic bound states before they decay further. They can be seen as hadronic jets in the detector and help identifying top pair events.

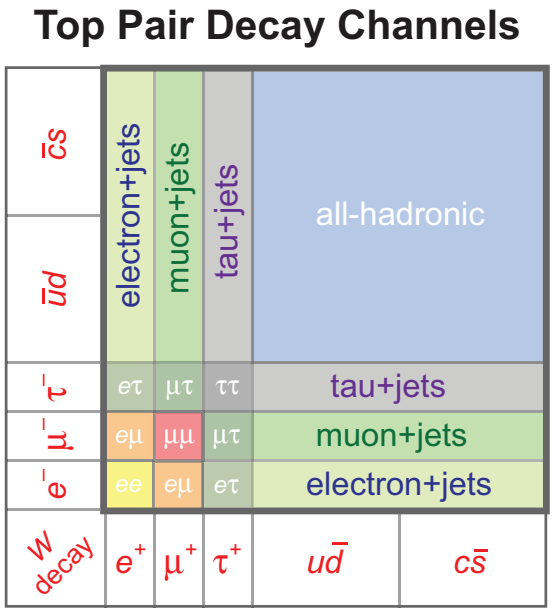

Figure 4.3.: The top quark decay channels. The considered dilepton channels are only those without τ-leptons. [43]

The classification of the top decay channels is done using the further decay of the W. It can decay either hadronically in two quarks or leptonically in a lepton and the regarding anti-neutrino. The relative branching rations are:

$$\frac{hadronically}{leptonically} = \frac{\{cs, ud\} \times colour}{\{e, \mu, \tau\}} = 6/3 \tag{4.8}$$

Accordingly, top pair events are characterized by the decays of the W^- and W^+ as fully hadronic (36/81), semileptonic (36/81) or dileptonic (9/81), as can be seen in figure 4.3.

In this thesis only dileptonic events will be analyzed. Excluding the decays with one or two τ-leptons, a total fraction of 4/81 of all top pair events counts as signal. An example for the dileptonic case is given in figure 4.4. The final state consists of two b-quarks, two charged leptons and two neutrinos.

4.2.1. Decay Width

The matrix element $|V_{tb}|$ does not only play an important role for the decay mode of the t-quark but also for its decay width. The theoretical prediction of the decay width is:

$$\Gamma(t \to Wb) = \frac{G_F m_t^3}{8\pi\sqrt{2}} \|V_{tb}\|^2 (1 + \mathcal{O}(\frac{m_W^4}{m_t^4})) \approx 1.5 GeV. \tag{4.9}$$

Expressed in lifetime this translates to $\tau_t \approx 4.3 \times 10^{-25}$s and $c\tau_t \approx 0.12$ fm. Compared to the hadronization scale $\tau_{hadr} \approx 28 \cdot 10^{-25}$ s this means that the

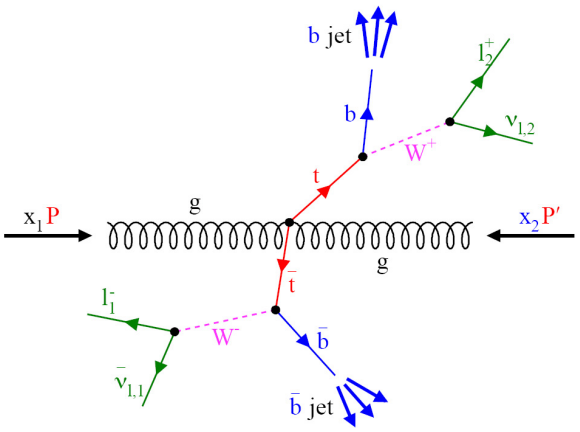

Figure 4.4.: The dileptonic decay of $t\bar{t}$-pairs is characterized by two b-quarks, two charged leptons and two neutrinos in the final state. In the detector the b-quarks will be visible as b-jets and together with the two charged leptons, this decay leaves a clear experimental signature.

top quark will decay before hadronization can take place. At present, the mass width has not been measured directly. The latest experimental results give an upper limit of 12.7 GeV at 95% C.L. [44]

4.3. Spin of the Top

As for the other fundamental fermions the spin of the top quark is expected to be $\frac{1}{2}$. Alternative integer spin hypotheses can be ruled out, since it would require another decay fragment besides W and b-quark carrying the remaining spin.

Unfortunately the direct spin measurement for quarks is far from trivial because hadronization dilutes any spin information. As explained above this is not the case for the almost instantly decaying top quark. In addition the lifetime is well below the average spin flip time and so the spin information of the top quark will be transfered to the decay products.

4.3.1. Spin Flip

Theoretically an (off-shell) top quark can change its spin state by radiating a gluon. The likelihood for this process can be estimated by

$$\Gamma(M1) \sim \alpha_s \cdot \frac{E_g^3}{m_t^2} \tag{4.10}$$

with E_g as the energy of the emitted gluon. For reasonable gluon energies, the to be expected time for a spin flip $\tau_{flip} = 1/\Gamma(M1)$ is much longer than the lifetime of the quark which is in the order of $\tau = 1/1.5\,\text{GeV}$. [45]

Table 4.1.: Correlation Coefficient α for the leptonic decay of a spin-up top quark. The parameter $\epsilon = \frac{m_t^2}{m_W^2}$ is calculated for a top mass of $m_t = 175GeV$ and a bottom mass of $m_b = 0$. The values are obtained from [46].

Particle	coefficient α in LO	LO value	NLO value
W^+	$\frac{\epsilon-2}{\epsilon+2}$	0.41	0.39
b	$-\frac{\epsilon-2}{\epsilon+2}$	-0.41	-0.39
ν	$\frac{(\epsilon-1)(\epsilon^2-11\epsilon-2)+12\epsilon\ln\epsilon}{(\epsilon+2)(\epsilon-1)^2}$	- 0.31	–
$\bar{e}$	1	1	0.998

4.4. Top Polarization

The spin polarization of the top quark can be analyzed through the angular distribution of its decay particles, which act as spin analyzers. The angular distribution of a spin analyzer with regard to the spin direction is given by:

$$\frac{1}{N}\frac{dN}{d\cos\Theta_i} = \frac{1}{2}\left(1 + P \cdot \alpha_i \cos\Theta_i\right) \tag{4.11}$$

where P is the magnitude of the polarization, depending on the chosen quantization axis. The factor α_i is the analyzer quality denoting, how much polarization information gets transfered, and depends on the particle type. It has to be noted that the analyzer i is not limited to direct daugthers (W, b) but W decay products are possible as well. The values are given in table 4.1. Even though b and W are first level daughters, their analyzing quality is quite low. This is due to the strong polarization of the W boson itself resulting in destructive interference.

In the case of single-top production, as an electroweak process, the spin of the top quark is 100% polarized if the right axis is chosen and a measurement of top polarizations in single-top events is possible [42]. For top quarks from $t\bar{t}$ production the situation is different. Because of parity invariance the polarization in the QCD induced process is zero at leading-order [47]. With one-loop corrections only a very small polarization of 2% transversal to the production plane is induced [48].

4.5. Spin–spin-Correlations

With the almost negligible top quark polarization in the pair production a remaining feature is the strong correlation of both top spins. Looking at the Feynman diagrams in figure 4.2, the dominant states at the threshold are ${}^1S_0$ (opposite spin, same helicity) for gg fusion, as a direct result of the Landau-Yang theorem, and ${}^3S_1$ (same spin, opposite helicity) for the s-channel $q\bar{q}$ annihilation. At the LHC as pp-collider the first process dominates, as at Tevatron

with lower energy (higher x) and because of $p\bar{p}$ collisions the $q\bar{q}$-annihilation dominates. One expects different correlations for both colliders.

Leaving the region near the threshold, the relative probability of other states increases. This can be seen in figure 4.5. At about 850 GeV the opposite spin state starts to dominate. This behaviour is due to a higher likelihood of angular momenta in the $t\bar{t}$ system for increasing energies.

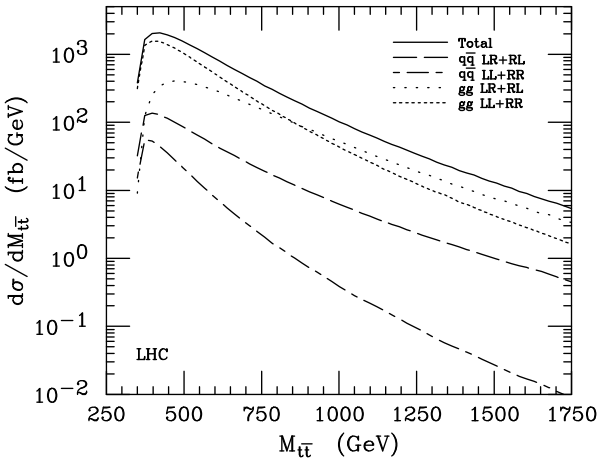

Figure 4.5.: Branching ratio for the different $t\bar{t}$ production processes at LHC. The strong dependency on $m_{t\bar{t}}$ has to be noted. [46]

In section 4.1 the matrix elements of $t\bar{t}$ pair production were introduced. For the sake of simplicity the spins were omitted. Introducing them now, the spin density matrix can be written as the following sum of four terms:

$$\rho = A \cdot 1 \otimes 1 + P_i^t \cdot \sigma_i \otimes 1 + P_i^{\bar{t}} \cdot 1 \otimes \sigma_i + S_{ij} \cdot \sigma_i \otimes \sigma_j \tag{4.12}$$

with σ_i as the usual Pauli matrices. The first part is the known production at parton level. The second and the third part are the already mentioned polarizations, which are $P_i^t = P_i^{\bar{t}} = 0$ for the tree level. The fourth part, the matrix S_{ij} can denote a spin correlation.

Using the correlation between top spin and decay particle directions from formula 4.11, the generic form can for the present case be translated into a double differential distribution for the decay products of the kind:

$$\frac{1}{N}\frac{d^2N}{d\cos\theta_1 d\cos\theta_2} = \frac{1}{4}\left(1 + P_1\kappa_1\cos\theta_1 + P_2\kappa_2\cos\theta_2 - A\kappa_1\kappa_2\cos\theta_1\cos\theta_2\right) \tag{4.13}$$

Again build as sum of four terms. These are a constant term, the polarizations of both tops and the spin–spin-correlation. The constants κ_1 and κ_2 denote the spin analyzer quality of the decay particles, the angles are chosen to a given spin quantization axis, and A is the strengths of the correlation, namely the spin asymmetry given by:

$$A = \frac{N(\uparrow\uparrow) + N(\downarrow\downarrow) - N(\uparrow\downarrow) - N(\downarrow\uparrow)}{N(\uparrow\uparrow) + N(\downarrow\downarrow) + N(\uparrow\downarrow) + N(\downarrow\uparrow)} \tag{4.14}$$

with the arrows representing the spin states of the top or anti-top respectively for the chosen quantization axes.

4.5.1. Spin-dependend observables

Spin dependend effects are measured via well defined observables. In general, observables can be simply constructed from the t and $\bar{t}$ spin operators, for instance

$$\begin{aligned} \hat{\mathcal{O}}_1 &= \sigma \otimes \sigma, \\ \hat{\mathcal{O}}_2 &= \hat{k} \cdot \sigma \otimes \hat{k} \cdot \sigma, \end{aligned}$$

where $\hat{k}$ is the direction of the outgoing top quark. These are the two observables that will be explored in this thesis. For additional choices see [49]. Translated into measurable quantities, replacing the spin operators by the spin analyzing particles, the observables become:

$$\begin{aligned} \mathcal{O}_1 &= p^*_{l^+} \cdot p^*_{l^-}, \\ \mathcal{O}_2 &= (p^*_{l^+} \cdot p_t)(p^*_{l^-} \cdot p_t), \end{aligned}$$

with $p^*_{l^+}$ and $p^*_{l^-}$ as momenta of the charged leptons coming from the dileptonic $t\bar{t}$ event.

4.5.2. The Observable $\mathcal{O}_1$

For the first observable one gets a distribution like

$$\frac{1}{N}\frac{dN}{d\cos\phi} = \frac{1}{2}(1 - A_D \kappa_1 \kappa_2 \cos\phi), \tag{4.15}$$

where ϕ is the angle between the (anti-)top analyzing lepton in the (anti-)top rest frame, in the following referred to as *opening angle*. The newly introduced correlation parameter A_D is connected to the expectation value $\langle \mathcal{O}_1 \rangle = A_D \kappa_1 \kappa_2$ of the observable. The theoretical distribution for the Standard Model case is shown in figure 4.6.

4.5.3. The Observable $\mathcal{O}_2$

For the second observable the expectation value $\langle \mathcal{O}_2 \rangle = A\kappa_1\kappa_2 = C$ is the asymmetry parameter from formula 4.13. As already mentioned the quantization axis is important for this value. There are several possibilities for a quantization axis. In practice only three choices play an important role, which are the beam basis, the off-diagonal basis [50] and the helicity basis. With $\hat{p}$ as the direction of the incoming beam and $\hat{k}$ again as the direction of the outgoing top quark the spin quantization axes a and b are defined as follows:

$$\begin{aligned} a = b &= \hat{p}\ (\text{beam basis}) \\ a = -b &= \hat{k}\ (\text{helicity basis}) \\ a = b &= d\ (\text{off} - \text{diagonal basis}) \end{aligned}$$

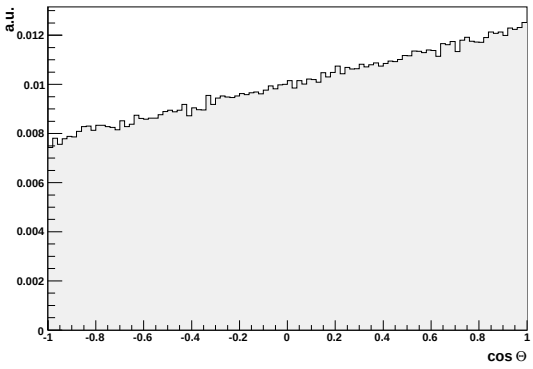

Figure 4.6.: One dimensional distribution of the lepton opening angle for the SM case. It is used to measure the observable $\mathcal{O}_1$. In this case the parameter is -0.290.

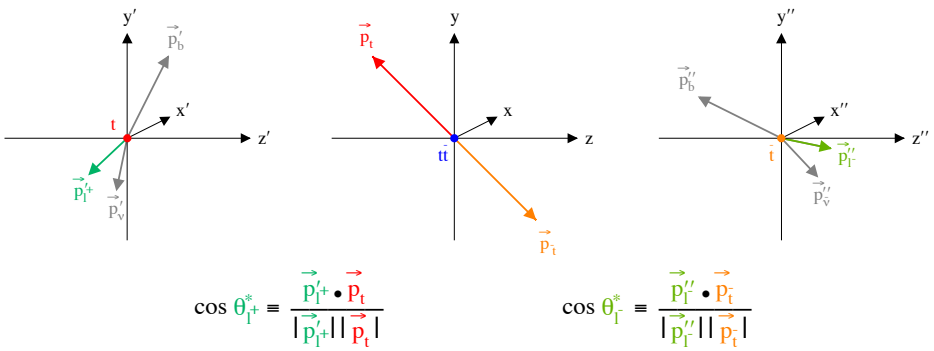

Figure 4.7.: Explanation of the helicity basis. The helicity angle of a lepton is calculated by the angle between the lepton momentum in the rest frame of the corresponding top and the top momentum in the $t\bar{t}$ rest frame. [52]

For Tevatron, where mainly $q\bar{q}$ annihilation takes place, the beam basis is the quantization of choice, yielding a correlation of almost 90% at leading order. For LHC there is no such ideal basis. The best result for a such reconstructed quantizations is given by the helicity basis. The paper [51] proposes a way to improve the spin correlation by chosing the axis on an event-by-event basis. For LHC this approach improves the predicted value for the spin correlation by almost 10%. Yet the helicity basis is chosen because of its stability with regard to reconstruction errors.

In the helicity basis the product of $p_{l^\pm}$ and p_t is calculated with the angle between the lepton boosted in the corresponding top rest frame, and the top momentum boosted in the $t\bar{t}$ rest frame. In figure 4.7 the lepton angles and their determination are illustrated.

More elegant, but less comprehensible, the helicity angle $\cos\theta$ of a lepton can be expressed in terms of lorentz-invariant quantities (see appendix A for

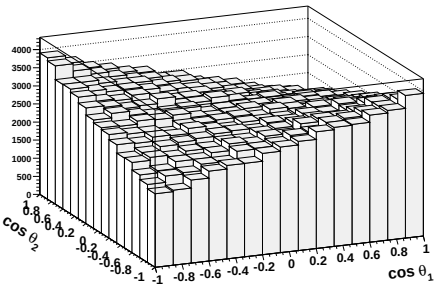

Figure 4.8.: Double differential distribution for the SM model case.

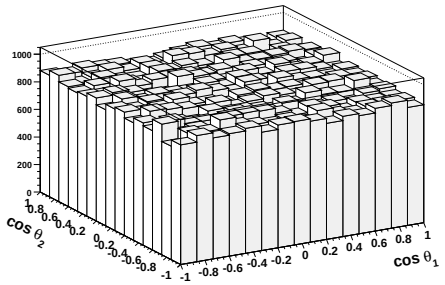

Figure 4.9.: The double differential distribution for the case of no spin–spin-correlation.

the derivation):

$$\cos\theta = \frac{2(m_t^2(p_l p_{t\bar{t}}) - (p_t p_{t\bar{t}})(p_t p_l))}{\hat{s}\sqrt{1-4m_t^2/\hat{s}}\sqrt{(p_t p_l)^2 - m_t^2 m_l^2}}. \tag{4.16}$$

Distribution of Decay Particles

The angular distribution of the decay particles was already introduced at the beginning of this section in equation 4.13, where now $\cos\theta_1$ and $\cos\theta_2$ can be understood as helicity angles. For the SM case the distribution is shown in figure 4.8. It was simulated using the TopReX [53] generator with CTEQ5L for the LHC environment. Figure 4.9 shows the shape of the distribution in case of no correlations. It was simulated using Pythia [54].

In figure 4.10 the probability density of $cos\theta_1 \cdot cos\theta_2$ is given. Both this and the two dimensional version of the correlation are used throughout the literature. Though the double differential distribution itself will be discussed in this thesis, the one dimensional version will be used for visual representation. This will be done due to the lack of dimensions for plotting if two or more distributions are compared.

The theoretical behaviour of the one-dimensional distribution is given after integrating the two dimensional one by

$$P(\zeta) = -\frac{1}{2}\ln|\zeta|(1 + A\zeta), \tag{4.17}$$

with $\zeta = cos\theta_1 \cdot cos\theta_2$. It is plotted in figure 4.11 for different values of the asymmetry. Since the visual difference between both scenarios is very small, another convenient way is plotting only the difference to the non-correlated distribution: $\Delta(\zeta) = -\frac{1}{2}\ln|\zeta|\,\zeta \cdot A$, as shown in figure 4.12.

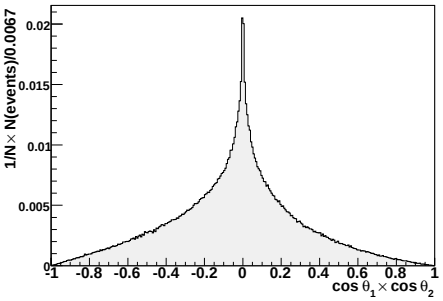

Figure 4.10.: The double differential distribution as projection to $\cos\theta_1 \cdot \cos\theta_2$ in the SM case.

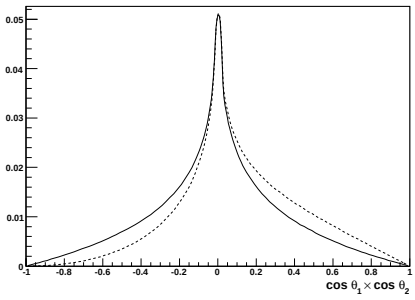

Figure 4.11.: Theoretical distribution for $A = 0$ (solid line) or $A = +1$ spin correlation (dashed line).

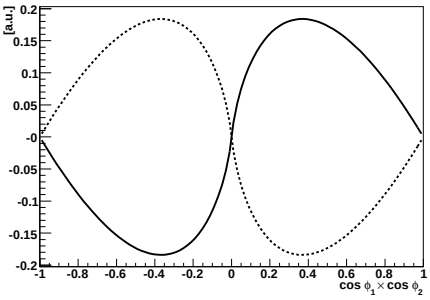

Figure 4.12.: Difference between distribution $A = 0$ and other scenarios fo $A = -1$ (solid line) and $A = 1$ (dashed line).

4.5.4. Predictions for LHC

The expected spin-correlations at LHC in LO are $A = 0.319$ and $A_D = -0.217$. Using the behaviour of the differential cross section as shown in fig. 4.5, the asymmetry can be increased by applying an upper cut on the mass $m_{t\bar{t}}$. Taking a commonly used cut of $m_{t\bar{t}} < 550$ GeV, the theoretical spin-correlation parameters become $A = 0.422$ and $A_D = -0.290$.

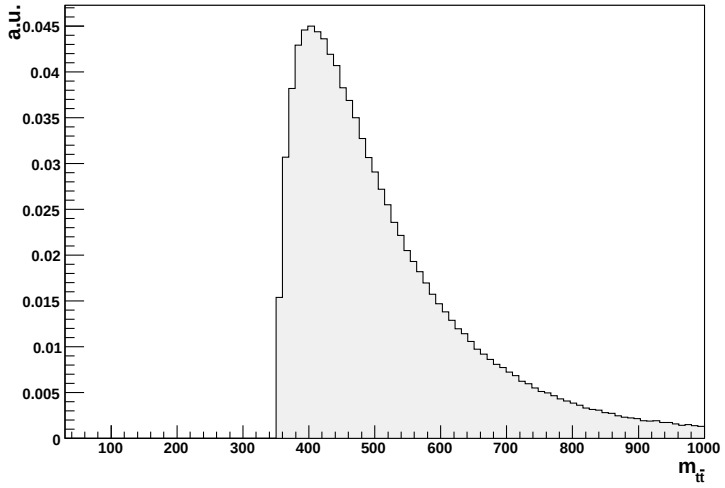

Figure 4.13.: Distribution of $m_{t\bar{t}}$. An upper cut of 550 GeV is chosen to improve the spin-correlation.

4.6. Existing Spin-Correlation Measurements

So far the only possibility for a study of spin–spin-correlations are the Tevatron experiments. Both CDF and D0 did studies on this topic during Run-I. They obtained limits of $A > 0.25$ at 68% C.L. [55], which cannot be compared with the expectations at LHC. At Tevatron the main production processes are different from LHC and thus the predicted value of $A = 0.88$ is significantly different from the LHC predictions. Furthermore this value is defined in another spin base. So the effect of spin correlation has still not been observed yet. For Run-II it is expected to get first results on the 40% level.

4.7. New Physics in Spin Correlations

There are several effects beyond the Standard Model which could affect the measured spin–spin-correlations. One of the assumptions for measuring Standard Model spin–spin-correlations is the short lifetime of the quasi-free top quark. So a correlation measurement can set an upper limit to the lifetime, which is directly linked to the CKM matrix elements (see section 4.2.1). Left-

handed coupling and spin 1/2 are other aspects that can be checked without any influence from hadronization and confinement effects.

Measuring derivations from the prediction will therefore be an indication for new physics. Non-SM interactions like anomalous couplings from dynamical electroweak symmetry breaking models, like top- or technicolour will change the predicted distributions. New heavy resonances in the production like Spin-2 Kaluza-Klein gravitons or a spin 0 neutral Higgs boson affect spin-correlation as well. An example are theories with large extra dimensions. Intermediate Spin-2 Graviton Kaluza-Klein modes in the s-channel induce specific changes to the spin-correlations, which can be seen in the angular distributions of outgoing particles.

Not only the production, but the decay of the top can be influenced by new physics as well. A prominent example is the existence of charged Higgs decay of the top ($t \rightarrow H^+ b$). The spin analyzer quality of the decay products will change and thus the angular distribution will be different from the expected behaviour. [46]

5. CMS Software Infrastructure

Almost no present experiment in high energy physics can be run without a vast amount of software tools, computing resources and well designed infrastructures. This chapter briefly describes the used software tools and computing infrastructures. In the meantime the CMS collaboration replaced many of the tools used for this thesis. Details on the new software, CMSSW, can be found in [9].

5.1. Monte-Carlo-Generators

Through the CMS interface CMKIN [56] several event generators are accessible. For this study mainly two event generators have been used – Pythia [54] and TopReX [53]. The important difference between Pythia and TopReX is the consideration of spin-spin-correlations in the latter. As already mentioned in chapter 4 the spin analyzing quality in the dileptonic channel is quite insensitive to NLO corrections, thus the present study is already at LO very meaningful. How big the effect of NLO calculations on the kinematics of $t\bar{t}$ events is, is subject to other studies. For the present case those effects will be taken care of in the systematic uncertainty. A third generator, ALPGEN 2.05 [57], was used to create some of the non-$t\bar{t}$ background, as described in chapter 7. In [58] an extensive summary of the used MC sample production and settings is given.

5.1.1. Customized TopReX Event Generator

To allow better systematic studies TopReX was extended for this study to be able to produce the different helicity states of the $t\bar{t}$ system separately. The according processing can be selected by *ipar(33)*. The new routines have, heavily modified, become part of TopReX since version 4.22 and are accessible from within the new CMSSW framework as well.

In figure 5.1 ff. the four possible helicity states are shown. Each of the distributions consists of two polarization and one comparably strong correlation contribution as described in formula 4.13.

It has to be pointed out that the relative probabilities of the four split up matrix elements stay the same. In particular the dependency on the invariant mass of the $t\bar{t}$ system is unaltered. The reason for this approach is to avoid the need for reweighting routines in the standard model case. Flexible reweighting routines for other cases have been set up.

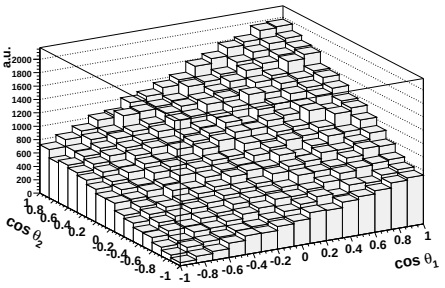

Figure 5.1.: Double differential distribution for the ↑↑ helicity state.

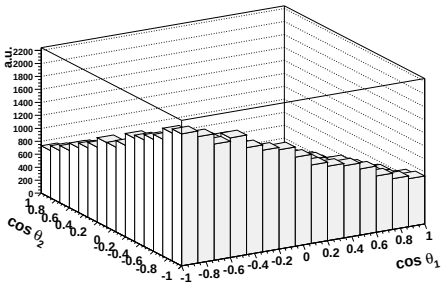

Figure 5.2.: Double differential distribution for the ↓↓ helicity state.

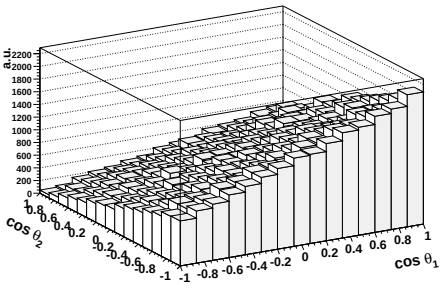

Figure 5.3.: Double differential distribution for the ↑↓ helicity state.

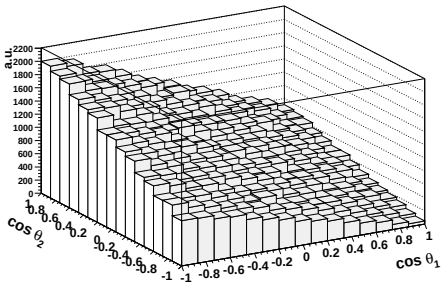

Figure 5.4.: Double differential distribution for the ↓↑ helicity state.

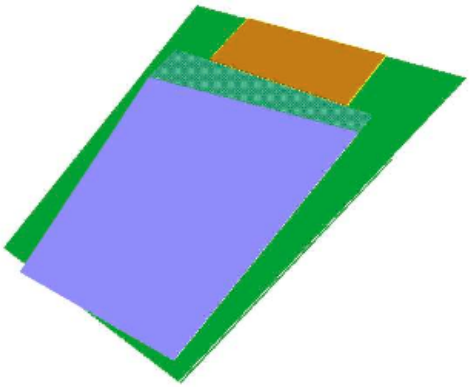

Figure 5.5.: Tracker module modelling in the simulation software.

5.2. Detector Simulation

After the actual physics process has been simulated the next steps are to simulate the interaction of the final state particles in the detector material and the resulting read out signal. The former is called *Simulation*, the latter *Digitization*.

The simulation was done using the application *OSCAR* (**O**bject Oriented **S**imulation for **C**MS **A**nalysis and **R**econstruction) [59]. Internally it is based on the software package *GEANT 4* [60]. It simulates the interaction of particles with the given detector geometry and magnetic field. The result of the simulation are energy depositions in the sensitive parts of the detector volume, so called *SimHits*. Those hits are connected via *SimTracks* of the generated particles. In certain cases time stamps for time-of-flight effects are included. Detector simulation requires a fairly detailed description of all detector components, both the passive as well as the sensitive elements. For reconstruction an accurate description of active detector parts is needed. The needs for the passive parts during reconstruction are slightly lower than for simulation, but nevertheless present. In CMS the detector geometry is modeled via the CMS specific *DDD* (**D**etector **D**escription **D**atabase) [61]. How detailed the description is, can be seen from a tracker detector shown in figure 5.5.

The conversion from the simulated energy depositions to the detector read out signal, i.e. the digitization, was done using *ORCA*. During this step the pile-up is mixed into the detector response. Like OSCAR it is based on the COBRA (**CO**herent **B**ase for **R**econstruction and **A**nalysis) framework. [62]

5.3. Reconstruction tools

The output of the detector simulation as described in the section above, is in the same data format as the later real experimental data. Therefore the following reconstruction and analysis steps could apply to real data as well. The reconstruction was done using *ORCA*. Software engineering details can be found in [62]. The used reconstruction algorithms and physics object definitions are

explained in chapter 6 later in this thesis. The subset of the reconstructed output used for standard physics analyses is called DST (Data Summary Tape).

Since the usage of DST files turned out to need a good understanding of higher programming concepts and some core functionalities were missing, an additional data format called *ExROOTAnalysis* [63] got developed. For this thesis some of the concepts of this format were used and adjusted to the boundary conditions of the locally available resources.

The mentioned problems are one of the reasons why the complete CMS software infrastructure was reviewed and almost everything got transformed into the newly created CMSSW. While the new software was not used to obtain any of the results presented in this thesis, the developed routines are already ported to the new framework and can be used by others for cross checking the results.

5.4. Fast Simulation

In order to do systematic studies usually a much higher number of events needs to be simulated. To serve this need *FAMOS* [64] was developed, which does are parameterized simulation. On average the simulation time is faster by an order of 10^3. In the meantime FAMOS became part of the overall CMSSW framework. For reasons mentioned in section 7.10 none of the results presented in this thesis were made using the fast simulation.

5.5. Data Flow and Computing

As already stated in section 2.2.7 CMS produces roughly 10 TB of data each day. To provide analysis infrastructures for thousands of physicists, a single computing centre would be both technically and politically almost impossible. Instead the computing resources are distributed among multiple computing centres. These are connected via the LHC Computing GRID (LCG). This allows to have transparent access to virtually any of the resources provided by the experiment. Details on the usage of general grid technologies in CMS can for example be found in [65].

Tiered Architecture

In CMS the computing centres are ordered hierarchically in *Tiers* of order 0 to 3. The Tier-0 is the data centre directly connected to the CMS data acquisition system. It performs the split of the data into primary datasets and does a first instant reconstruction.The data is then shipped to the other tiers, which have a certain function. In total six Tier-1 centres, distributed over several time zones, will be responsible for the main processing and reconstruction of the data. To each Tier-1 there are a few Tier-2 centres connected, that serve for data analysis and Monte-Carlo production. Finally Tier-3 centres are (small) clusters of the local university or institute working groups. Most of the single user analyses will happen here. How data are shipped between these centres gets explained

in section 5.5.2. More information on the CMS computing model can be found in [65].

5.5.1. CMS Data Tiers

The CMS Event Data Model (EDM) is a uniform format and technology to manage and store all event data. An event is a container of many so-called products, each of them can be implemented in almost any possible C++ type. Many event products are collections of objects (like tracks, clusters, particles, ...). A main feature of the CMS EDM is the fact, that the persistent and transient representation of any data are identical. This allows uniform object access in both batch and interactive mode. As underlying technology ROOT I/O [66] is chosen and Reflex dictionaries are provided for every stored object type.

Event Data Tiers

CMS defines different standard data tiers corresponding to different levels of detail required by various applications, ranging from alignment, calibration and detector studies, to physics analysis:

FEVT contains (almost) the full event content, including many outputs of intermediate processing steps.

RECO contains a detailed reconstruction output that allows to apply new calibrations and alignments and reprocess many of the components.

AOD (Analysis Object Data) is a subset of reconstructed data (RECO) chosen to satisfy the needs of a large fraction of Physics analysis studies. The final goal is a size of roughly 100 kilo-bytes per event

TAG should contain very basic tag information. This data tier is part of the Computing TDR, but up to now there is now concrete implementation. [65]

Based on these common data formats, new data formats can be defined by adding or dropping products. This is done by simply changing the job configuration without additional need for higher level programming. A use case for a modified event content are analysis groups, which can easily define custom data types that are added to the event. This is convenient to both save CPU time avoiding to re-compute frequently used quantities, and to be able to directly use these quantities in an interactive analysis session.

5.5.2. Analysis Data Workflow

As already explained in previous sections, the computing model of CMS is separated into tiers. This gets reflected in the way, how data and work flow for a typical analysis are organized. A schematic view is shown in 5.6. Data coming from the filter farm is reconstructed in a first pass at the Tier-0 site. They are then, mainly based on HLT bits, split into several primary datasets

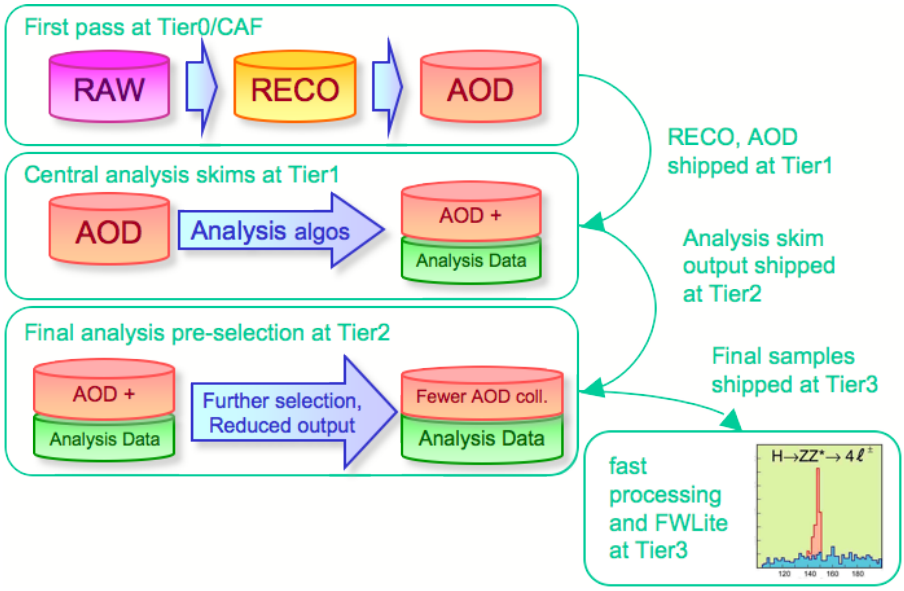

Figure 5.6.: Data flow from Tier-0 to the final analysis. This is the current proposal and probably subject to future changes. [68]

and shipped in RECO and AOD formats at the Tier-1 sites. Here regular reprocessing, recalibration and new alignments can be applied.

Further analysis specific processing steps at this level are physics group specific pre-selections, called skimming jobs, copying certain subsets of the data to the Tier-2 centres. Skimming is driven by the physics groups and foreseen on monthly scale. The actual granularity and complexity of the skim processing may depend on the analysis channel. Though the standard data format is AOD, additional reconstruction tasks like customized clustering algorithms or lepton isolation variables can be run and group objects be added during this process. In certain circumstances one may decide to drop major fractions of the standard AOD product to save disk space.

At the Tier-2 sites the shipped skim output is then individually available for specific analyses and further processing steps with subsequent event selection, and further specialization of the event output content can be performed. Once the data samples at Tier-2 are further reduced and stored in a sufficiently compact format, they can be shipped to Tier-3 sites for the final analysis processing. A mixture of batch and interactive analysis can be applied at this stage. [67]

6. Reconstruction

In chapter 2 the different parts of the CMS detector have been described. How the data of these parts is used to build higher-level objects like electrons, muons or jets, is subject to the present chapter. For each object type relevant for this thesis the reconstruction methods, identification qualities and performances are discussed. A detailed overview on the reconstruction methods used in CMS is given in [9].

6.1. Track Reconstruction

The reconstruction of tracks can be divided in four steps:

- Cluster building and seed generation
- Trajectory building
- Trajectory cleaning
- Trajectory refitting

In the first step hits exceeding a signal-to-noise cut from neighboured pixels or strips are combined into clusters. The position of the cluster and its error are calculated. From these clusters *seeds* are generated. A seed consists of at least three hits, providing start parameters for a track helix. Mainly the pixel detector will be used for track seeding.

During the *trajectory building* the seed is extrapolated along a helix from the inner to the outer part of the detector. The search for compatible hits is taking multiple scattering and energy loss in the massive detector parts into account. For each layer traversed either the trajectory is updated with the new hit or, in case of a missing hit, a fake hit is added. This Kalman filter [69] driven procedure stops once the outermost layer of the tracking detector is reached. To avoid an exponentially increasing number of tracks with each additional layer included, trajectories have to follow some conditions like a maximum number of fake hits and an upper χ^2 of the fit.

In the next step the multiple *trajectories* are *cleaned*. Sometimes identical tracks are reconstructed from different seeds or multiple trajectories from the same seed. For trajectories sharing too many hits, only the best quality trajectory is kept.

As last step *trajectory refitting* is done. Since the trajectory building is based on Kalman filtering the parameters are only best for the last added hits. Once the full trajectory is build the refitting can recalculate the track parameters and covariance matrix. Finally an outside-in smoothing by a backwards running filter is performed. [70, 71]

6.2. Vertex Reconstruction

The starting point for the vertex finding are tracks, which are reconstructed as explained above. They are selected on their transverse impact parameter with regard to the beamline. The ratio of the impact parameter divided by its uncertainty has to be smaller than three. All remaining tracks are then clustered according to their z impact parameter. This is done using a least-squares based Kalman fitter. The resulting vertex candidates are ordered by $\sum P_T^2$ and the first one is taken as primary vertex.

The resolution of primary vertices for $t\bar{t}$ events is about 18 µm along the beam axis and 13 µm perpendicular in x and y. More details on vertex fitting in CMS can be found in [72].

6.3. Muon Reconstruction

For the muon reconstruction similar steps as for the track reconstruction apply. The starting point of the reconstruction are hits, followed by segment reconstruction and trajectory building.

6.3.1. Stand Alone Reconstruction

Natural starting point for the standalone muon reconstruction are detector signals in the muon system. Since the muon system is clearly separated in a barrel and an endcap region the algorithms for these both parts are quite different. [73]

Barrel Region

The barrel region of the muon system consists of drift tubes. Base of the reconstruction of hits in a drift tube is the drift time. Using look-up tables and signal models, both depending on the local magnetic field and the incident angle, the time can be translated into a hit position on the strip. These hit positions are used as input for the track segment reconstruction in the local drift tube chamber. Due to geometrical reasons there is a left-right ambiguity in the cluster position along a strip and both hypotheses are used in the track segment reconstruction.

Endcap Region

The cathode strip chambers in the muon endcap provide two coordinate informations. The ϕ coordinate is obtained by a cluster reconstruction from electronic signals in the cathode strips. The collected charge is fitted by the Gatti parameterization [74] and the position of the strip with the maximum signal is taken as position of the cluster. The r coordinate is measured via the anode wires. For each of the six CSC layers the two coordinates are combined into hits and a local track segment reconstruction is performed. The initial hypotheses are build from straight lines between hits in the inner- and outermost

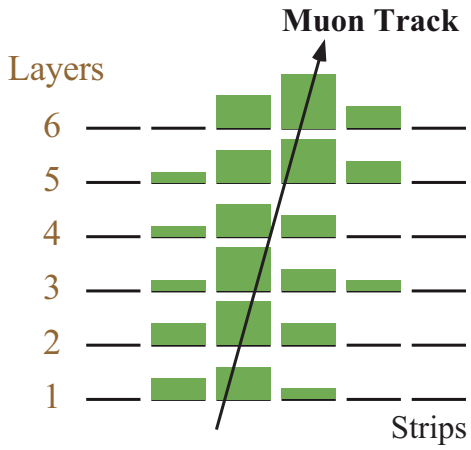

Figure 6.1.: Local reconstruction in the CSC. This R view shows the charge deposition of a transversing muon in the cathode strips. This information is used to reconstruct the ϕ coordinates of the trajectory.

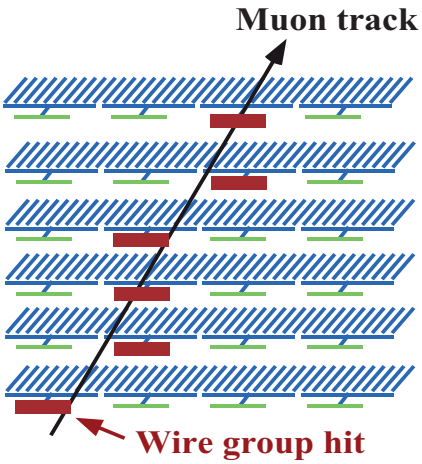

Figure 6.2.: Local reconstruction in the CSC. This ϕ view shows the wires hit by a transversing muon. The hits are used to retrieve the R coordinates of the trajectory.

layer. To build a line hypothesis the two initial hits have to match by 1 cm in both r and ϕ. If an intermediate hit in the region of 2.5 mm around this line is found the trajectory gets updated and the search is continued. If the final line has at least four hits, it is stored as track segment candidate.

RPC readout

The fast triggering RPCs use a simple clustering algorithm for hit reconstruction. Passing trough muons leave hits in adjacent strips. These strips are combined into clusters and the center of gravity is used as ϕ position of the hit, with the cluster width being the uncertainty. Since the strips are alinged along the beam pipe and no drift times are measured, the z position is only constrained by the length of the strip. As hypothesis for the z reconstruction the hit is placed in the strip center.

Level-2 Muon Reconstruction

The input of all three detector types, CSC, DT and RPC, are combined into standalone reconstructed muons. Either Level-1 trigger muons or track segments serve as starting point for a Kalman filter, going inside out. In the barrel region the track segments from the drift tubes are used directly, where in the endcap region with its very inhomogenious magnetic field single hits have to

be used in the algorithm. For every step the energy loss, multiple scattering and magnetic field fluctuations are taken into account via using the GEANE package [75]. Like for track reconstruction the resulting trajectory is smoothed by a backwards running Kalman filter. Assuming the origin of the muon being the interaction point a constrained fit is used to further improve the momentum resolution. The result of this procedure is called Level-2 muon.

6.3.2. Global Muon Reconstruction

So far the muon reconstruction only used information from the muon system. Using information from the tracker the resolution can be further improved. For this the Level-2 muons are extrapolated to the outer regions of the tracker. Again the GEANE package is used to incorporate multiple scattering and energy losses. Tracks compatible with the extrapolation are combined with the standalone muons. After refitting they form global muon candidates. How the combination of muon and track information improves the resolution is shown in figure 6.3. For low energies the multiple scattering in the material in front of the muon spectrometer limits the resolution and the combination with the tracker information is essential.

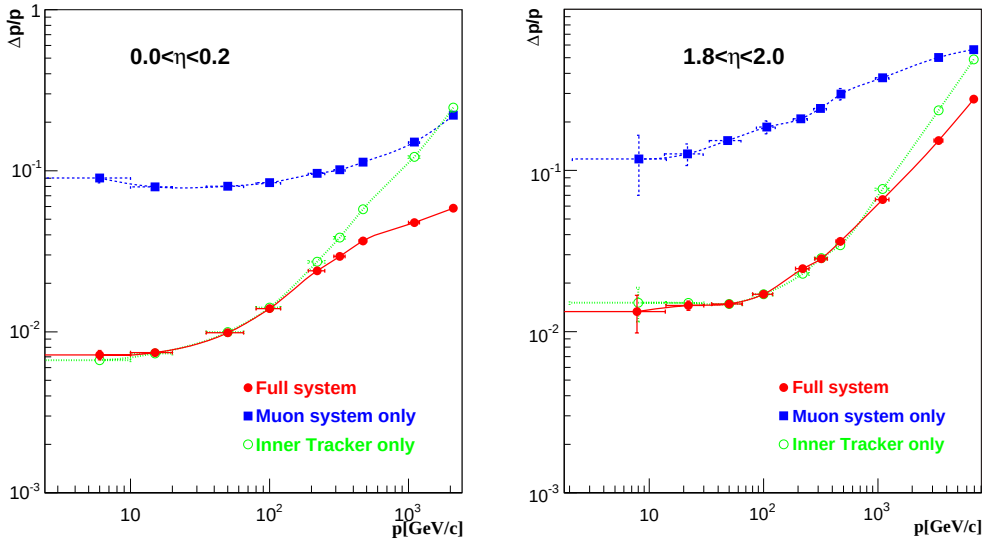

Figure 6.3.: Resolution of muon reconstruction from muon system only, tracker only, and both combined. [9]

6.3.3. Muon Reconstruction Performance

The performance of the formerly described reconstruction is checked for dileptonic top pair events. In figure 6.4 the efficiency of the muon reconstruction is shown. As one can see the efficiency is quite high and the global muons are almost taken as they are provided by the standard reconstruction methods. A sensitivity cut of $|\eta| < 2.4$ is applied.

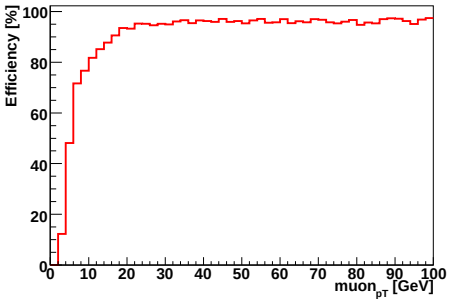

Figure 6.4.: Reconstruction efficiency of isolated muons as function of generated p_T.

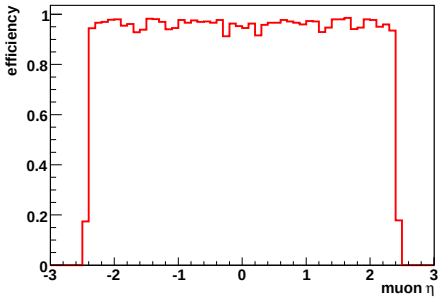

Figure 6.5.: Reconstruction efficiency of isolated muons as function of the generated η.

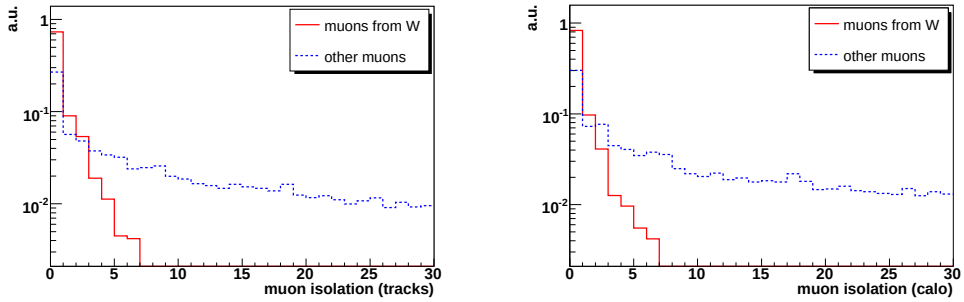

Figure 6.6.: Muon isolation criteria to distinguish muons from W (red) and muons from other sources (blue). Both isolation criteria are explained in the text.

Motivated by signal vs. background selection, muons are only considered if they satisfy $p_T > 20\,\text{GeV}$ and additional isolation criteria. In the scope of this thesis, a muon is considered isolated if the amount of additional tracks near to it is reasonably small. Translating this intp numbers the summed p_T of all tracks in a cone of 0.3 around the muon scaled by the muon p_T has to be smaller than 0.2. The same applies for the calorimeter entries in the same cone. The energy sum divided by the muon p_T should be smaller than 0.2. Both isolation cuts are shown in figure 6.6.

The resolution in η, ϕ and E_T of the remaining muons depending on p_t is shown in figure 6.7. Further details can be found in [76].

6.4. Electron Reconstruction

In the most simple case an electron transverses the tracker leaving a track and then creates an electromagnetic shower in the electromagnetic calorimeter. Such the basic signature of an electron is a cluster in the ECal which can be connected to a trajectory in the tracker. It has to be noted that a sizeable

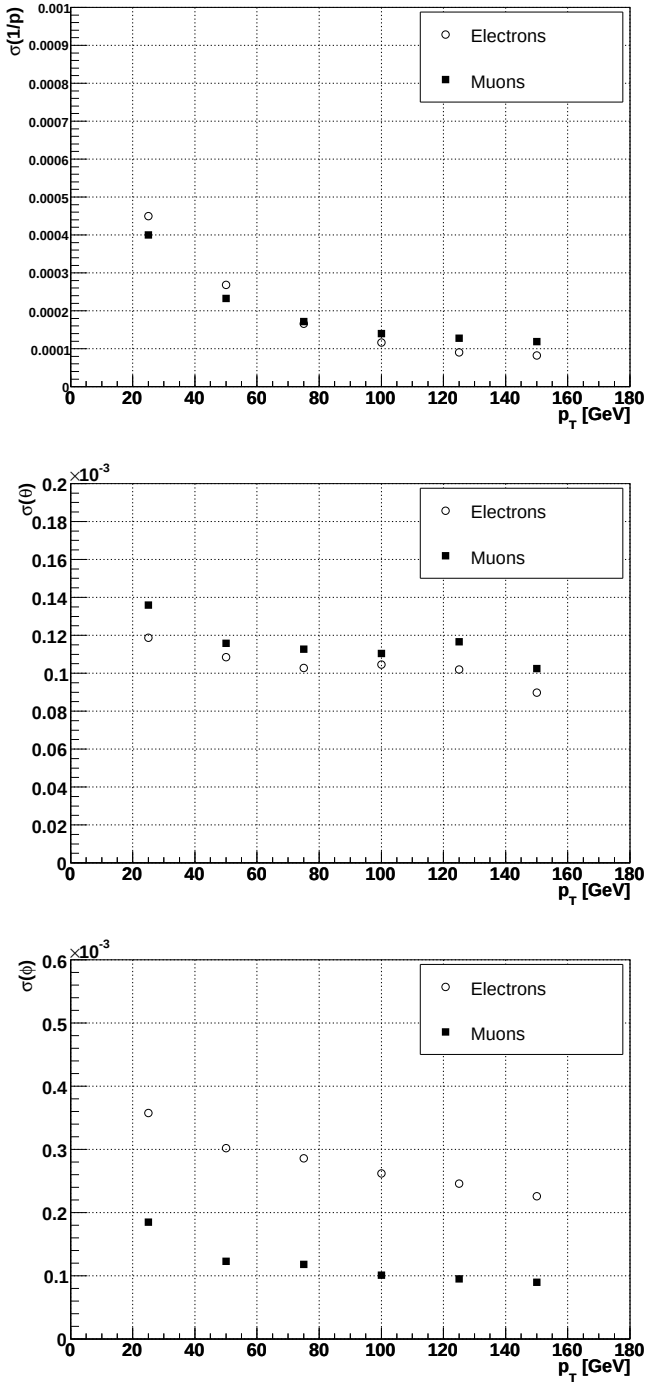

Figure 6.7.: Resolutions of muons (circles) and electrons (boxes) as coming from the pre-selection steps as function of their p_T. Upper: $1/p$; middle: θ; lower: ϕ. Similar studies for the semileptonic channel are available in [77].

amount of electrons already converses in the tracker, which makes the identification of such electrons more complicated. To identify such electrons and to reject fake electrons (e.g. energy depositons of photons which get misconnected to a track) likelihood methods need to be applied. In the following the single building blocks of the electron reconstruction are explained and the performance summarized.

6.4.1. ECal Supercluster

As explained in section 2.2.3 the CMS ECal is build from one single layer of crystals. An average electromagnetic shower from electrons or photons transversing the calorimeter is usually spread over several crystals. In a region of 3×3 crystals around the shower centre almost 94% of the electron energy is contained. For a region of 5×5 crystals it is already 97%. Unfortunately the tracker in front of the ECal leads to bremsstrahlung and photon conversion into e^+e^- pairs. The solenoidal magnetic field bends the energy of the intermediate electrons and the calorimeter hits are largely extended in ϕ. Thus a simple energy clustering is not sufficient for an optimal reconstruction of the electron energy. To overcome this problem, CMS uses two methods for creating super clusters. In the barrel region the *hybrid algorithm* is applied. It collects non-overlapping clusters by using a window around seed clusters with a long ϕ and a small η range. This is shown schematically in figure 6.8. [78]

In the end cap region a more flexible approach is used. The *island algorithm* takes a seed crystal with a certain minimum energy. Starting from this seed the algorithm performs a search in η and ϕ and clusters the crystals by decreasing energy. Nearby clusters are again combined into superclusters. (figure 6.9)

6.4.2. Energy and Direction Calibration

As the electrons already deposit some of their energy in the tracker or passive detector parts, or due to cracks in the geometry, the combined clusters do not represent all the electron energy. Therefore the raw electron energy is calibrated by a function dependend on the detector region. The same has to be done for the electron direction. The direction calibration is a function of particle type, energy and position. [79]

6.4.3. Electron Tracks

As electrons are charged particles they leave signals in the tracker. This can be used for improving the resolution and, via the bend direction, to determine the sign of the electric charge. As explained in section 6.1, track reconstruction is based on seeds. While the methods for track reconstruction stay the same, the seed is taken as the cluster position and a track evolution from the outermost tracker layer to the inner pixel is performed. After looking for compatible vertices the track is reconstructed. How the additional track information improves the reconstruction quality is shown in figure 6.10. In this study only

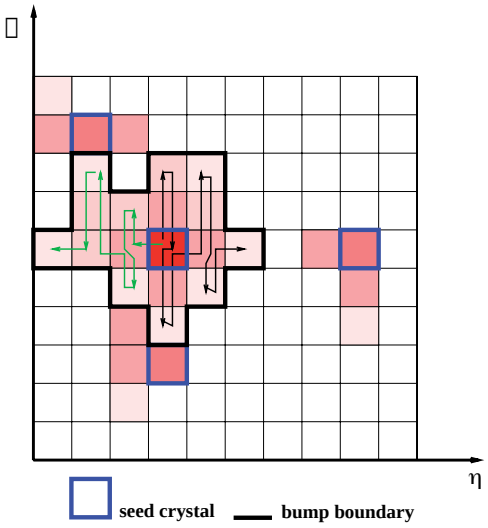

Figure 6.8.: The calorimeter cells have different energy deposits as indicated by brightness. The blue bordered cells have an energy exceeding the seed threshold. The black line indicates one cluster reconstructed by the island algorithm. The arrows are included to show the evolution of the algorithm. [78]

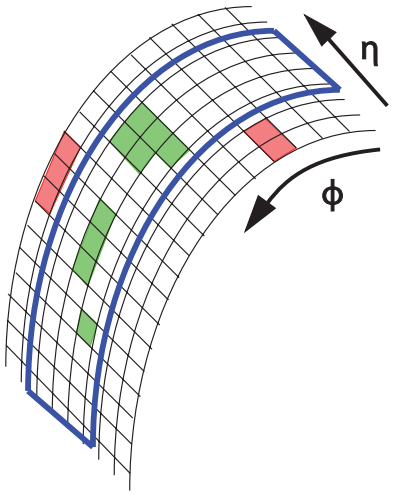

Figure 6.9.: The energy depositions corresponding to one electron (green) can be separated in ϕ due to several effects. The super cluster algorithm is used to combine the energy of several clusters into a supercluster, here indicated by the blue line. [78]

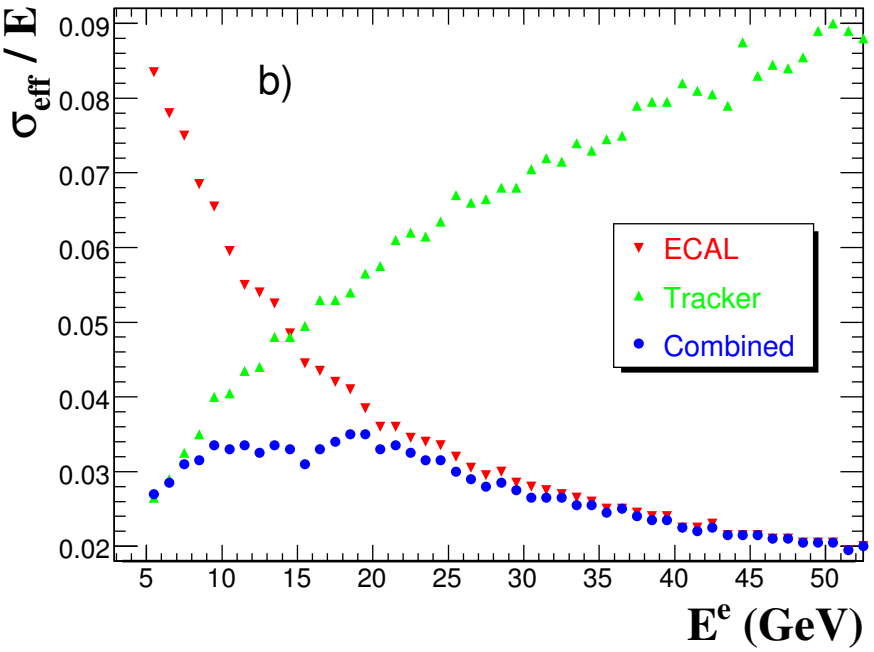

Figure 6.10.: The electron energy resolution using ECal energy deposits (red), tracker information (green) and the combination of both (blue). In this study the electron resolution is mainly dominated by the Ecal resolution. [9]

leptons with $p_T > 20\,\text{GeV}$ are used, so the electron resolution is dominated by the electromagnetic calorimeter.

6.4.4. Electron Cleaning

After reconstruction of electron candidates there are many duplicates. This is due to different tracks being compatible with the same supercluster. To get rid of the duplicates for each supercluster the fraction $\frac{E_{SC}}{|p|}$ for associated candidates is compared. The candidate being closest to 1 is selected.

6.4.5. Electron Reconstruction Performance

The electron reconstruction efficiency is shown in figures 6.11 and 6.12. The identification of electrons is following [77]. In addition isolation criteria are applied. In a cone of $\Delta R = 0.3$ no tracks not belonging to the electron candidate are allowed. The hadronic energy fraction has to be smaller than $|E_{\text{HCal}}/E_{\text{ECal}}| < 0.05$ for an electron. Both variables are shown in figure 6.13. The resolution for the remaining electrons is shown in comparison to the muon resolution (see fig. 6.7).

In general electrons in CMS are classified as golden, big brem, narrow and showering and resolutions plotted separately [9]. For this study all four classes

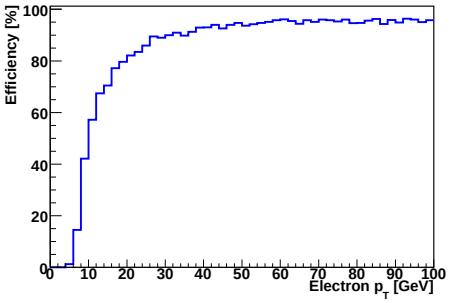

Figure 6.11.: Electron efficiency over electron p_T.

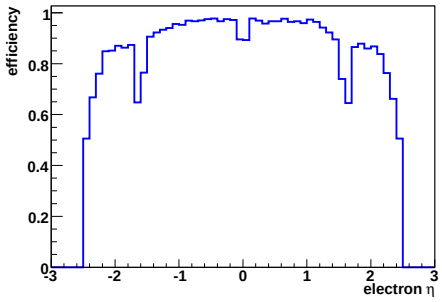

Figure 6.12.: Electron efficiency over electron η. The dips are due to the border between barrel and endcap.

are combined into one single resolution plot. The driving reason for determining the resolution for sample-specific electrons is the resolution smearing tried in section 7.3.4.

6.5. Jet Reconstruction

In the final state of the process under study two b quarks are created. As they can not exist as free particles because of the QCD confinement, each of the b quarks results in a shower of colourless hadrons, mainly pions and kaons.

The resulting shower of particles is mainly focused in the direction of the initial parton. By collecting the HCal, ECal and tracker signals from the shower fragments in so called *jets*, the kinematics of the inital quarks can be reconstructed. This will be explained in the following.

6.5.1. Calorimeter Cluster

The input for the jet reconstruction are hits in the electromagnetic and the hadronic calorimeter. The HCal cells are grouped into HCal towers. Because of their higher granularity multiple ECal crystals are assigned to one single HCal tower, building combined *calorimeter towers*. Including the forward calorimeter there are 4176 towers in total.

6.5.2. Jet Clustering Algorithms

Currently there are three main clustering algorithms used in CMS: Iterative cone (IC), midpoint cone (MC) and the k_t algorithm [80]. Because of the relativistic kinematics the cones are not opened in the θ–ϕ-space but in the η–ϕ-space.

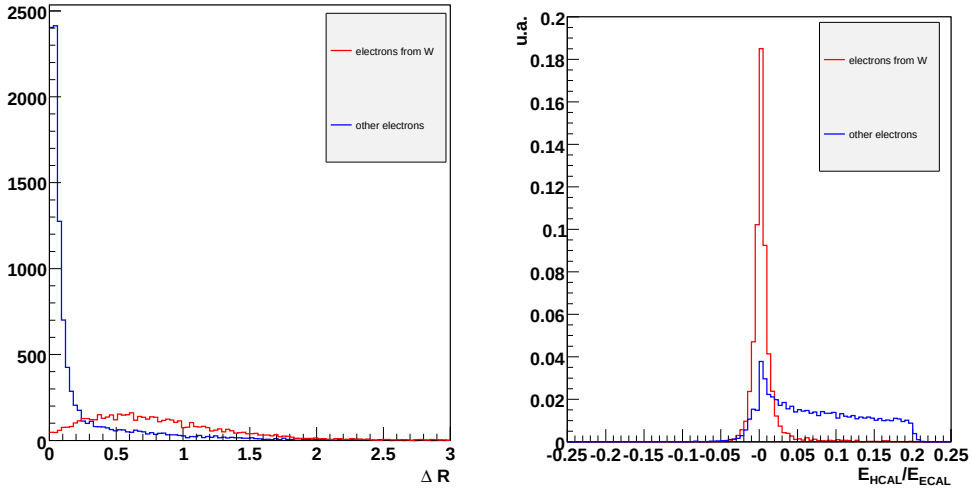

Figure 6.13.: Electron isolation criteria to distinguish electrons from W (red) and electrons from other sources (green). Both isolation criteria are explained in the text.

Iterative cone algorithm

The iterative cone algorithm has two input parameters: a seed threshold and a cone size. The starting point of the algorithm is an E_T ordered list of the input objects, which could be for example calorimeter towers or MC particles from simulation. If the first object is above the seed threshold it is taken as a so-called proto jet. Objects in a given cone around this seed are clustered to a new proto jet with an updated four momentum. This algorithm is repeated until there are no more objects in the cone around the proto-jet left. This stabilized object is then taken as a jet and all the objects forming the jet are removed from the input list. The procedure of finding jets gets repeated until no object above the seed threshold is left.

Midpoint cone algorithm

A problem for the iterative cone algorithm are overlapping jets. Since the resulting jets are not overlapping by method, overlapping jets are reconstructed quite badly. An attempt to overcome this problem is the midpoint cone algorithm. In a first step the same proto-jets as in the iterative cone method are created. Only, the proto-jet constituents are not removed from the input list. This allows different jets sharing constituents.

The k_T algorithm

From all input objects and all possible pairs the following quantities are calculated:

$$d_i = (E_{Ti})^2 R^2$$

$$d_{ij} = min\{E_{Ti}^2, E_{Tj}^2\} \cdot R_{ij},$$

with the dimensionless cut-off parameter R and R_{ij} defined as

$$R_{ij}^2 = (\eta_i - \eta_j)^2 + (\phi_i - \phi_j)^2.$$

If the smallest value is a pair d_{ij} the two objects are removed from the input list and combined to a new object. If the smallest value is the d_i for a single object, it is removed from the list and taken as a final jet. This procedure is repeated until there are no input objects left.

Chosen method

The IC algorithm is the best suited for this analysis, because its behaviour in the LHC environment is well understood. A more detailed study for the different $t\bar{t}$ channels can be found in chapter 8 of [81]. It has to be noted that the IC with a cone size of 0.4 seemed to be better suited on the generator level, but in fact a cone size of 0.5 turned out to be the better choice considering fully simulated samples [82].

6.5.3. Jet Energy Calibration

There are several effects that make the connection of the jet energy with the true parton level energy difficult. The problems can be divided in two classes which are of either theoretical or instrumental nature. On the theoretical side final-state radiation and hadronization effects blur the energy, underlying event and pile-up collisions give additional external contributions to the jet reconstruction. Finally neutrinos are invisible to the detector and leads to missing energy in the detector.

On the instrumental side the electromagnetic field bends out low energetic jet constituents, the response of the calorimeters is unequal for different cells, dead material and leakage reduce the measured energy. Finally electronic noise causes problems as well.

To correct for these problems, several jet energy calibration schemes exist. They can be roughly divided into two families of methods. Either the reconstructed jet energy is calibrated to the particle-level jet, or the energy is calibrated to the parton itself. Using particle-level calibrations some effects can be factorized out, like channel dependency and changes due to the jet algorithm chosen. For parton-level calibrations gluon radiation plays an important role and has to be taken into account.

In the following some of the schemes used or proposed by the CMS collaboration will be explained.

- **Monte-Carlo calibration:**

  This Monte-Carlo based method [83] assumes that the detector simulation is well tuned. Base of this tuning are for example test-beam measurements.

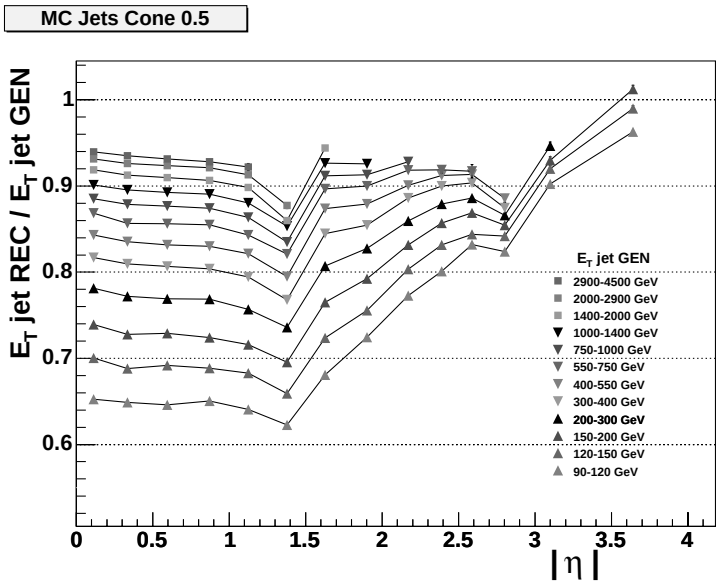

Figure 6.14.: Comparison of transverse jet energy E_T from MC and calorimeter clustering. [9]

Simulated jets are reconstructed in two ways. On the one hand using the MC particle information, excluding neutrinos and muons. On the other hand with calorimeter towers. For both reconstructions the same parameters are applied. The two jet versions are matched within $\Delta R < 0.2$ and a correction to E_T as function of η and p_T is calculated. In figure 6.14 a comparison of MC and calorimeter jets is shown. The final resolution is shown in figure 6.15.

- **Di-jet balancing** as described in [84] is using QCD di-jet events. Defining the di-jet balance

$$b = \frac{p_T^{probe} - p_T^{ref}}{p_T^{probe} + p_T^{ref}}, \tag{6.1}$$

with one jet as reference and the other one as probe jet, the relative response $2\langle b\rangle / (2 - \langle b\rangle)$ as function of η can be used to get relative calibration functions. This calibration technique is well suited for online calibration and monitoring.

- **γ-jet balancing** uses the good energy resolution of the ECal to calibrate the HCal. In prompt photon emissions $gq \rightarrow \gamma q$ and $q\bar{q} \rightarrow \gamma g$, the detector signal is a photon and a hadronic jet which are in leading order transversaly balanced, neglecting initial transversal momenta. Using the better resolution of the ECal, the photon can be taken to determine the "real" energy of the hadronic jet. [85]

- **W boson mass fit:** In hadronical W decays, the energy of both jets can be calibrated using the known W mass. In order to take advantage of this

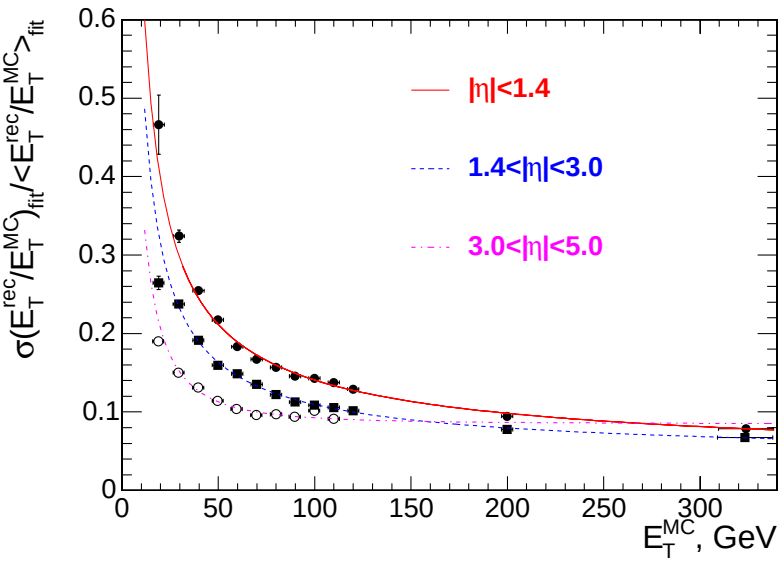

Figure 6.15.: The transverse jet energy resolution for iterative cone $R = 0.5$ jets after Monte-Carlo calibration. [9]

feature, a very clean W sample has to be used. Excellent candidates are semileptonic $t\bar{t}$ decays. [86]

6.6. B-Jet Identification

The smallness of the matrix elements V_{ub} and V_{cb} results in a lifetime of B-Hadrons in the order of 1.5 ps or a flight distance of $c \cdot \tau \approx 450\,\mu m$ accordingly. With the resolution of the vertex detector being one order of magnitude higher the reconstruction of the B-decay as secondary vertex will be possible. Together with significant differences in kinematical and topological distributions with regard to lighter hadrons a so-called b-tag can be applied.

The flight distance of 450 µm leads to a decay vertex of the B that is significant different to the primary vertex. This secondary vertex can be reconstructed by displaced tracks that have their origin in the B decay. Starting from the secondary vertex, the identification of b jets is now done using the following criteria [87]:

- The invariant mass of all charged particles in the vertex. B-hadrons have a larger invariant mass than decays from other flavours.
- The multiplicity of charged particle tracks belonging to the secondary vertex. B- hadron decays have 5 charged particles on average.
- The flight distance significance, i. e. the transverse distance between primary and secondary vertex divided by their errors.

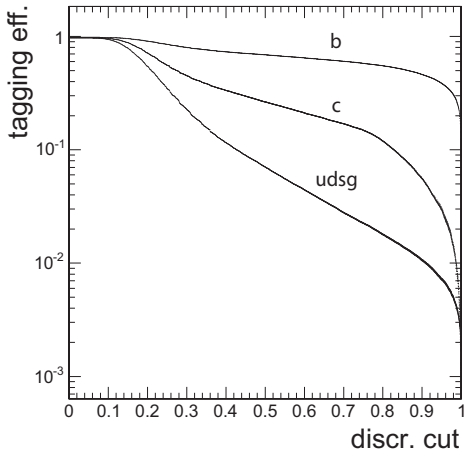

Figure 6.16.: The efficiency of the b tagging algorithm for different flavours and discriminator cuts. It was created using QCD events with $30\,\text{GeV} < p_T < 200\,\text{GeV}$ and $|\eta| < 2.4$. [87]

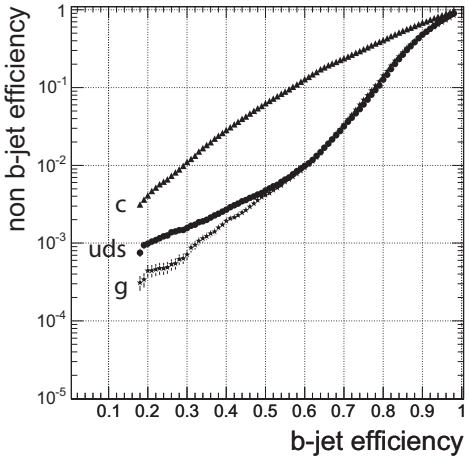

Figure 6.17.: Comparison of bjet mistagging and b jet tagging efficiency for different jet flavours. The data was retrieved using semileptonic $t\bar{t}$ events. [87]

- The energy of the charged particle tracks from the secondary vertex divided by the total energy of charged jet particles. This is connected to the hard b-fragmentation.
- The rapidities of charged particle tracks coming from the vertex with respect to the jet direction.
- The track impact parameter significance of the tracks exceeding a charm related mass threshold.

B-tagging

All the above mentioned criteria are combined into a likelihood ratio

$$y = f_{BG}(c) \times \frac{L^b}{L^b + L^c} + f_{BG}(q) \times \frac{L^b}{L^b + L^q},$$

where $f_{BG}(c, q)$ are the prior of the non b-jet part. The terms $L^{b,c,q}$ are connected to the probability of jets coming from the denoted quark flavour or a gluon. These values are calculated using the input variables mentioned above. The scaling of y is such, that b jets get more likely for higher discriminator values. The efficiency of the used b tagging methods is shown in the figures 6.16 and 6.17. It discriminates light quark and b quark jets by two orders of magnitude.

6.7. Missing Transverse Energy

In a proton–proton collision the longitudinal momentum of the system is undefined, where the transversal momentum can, to a certain amount, be assumed to be zero. The difference between the p_T sum of the detector objects and zero is called missing transverse energy or MET. In CMS the MET is reconstructed by using the sum of all electromagnetic and hadronic calorimeter towers, corrected for jet calibrations and the information from the muon system, since muons leave the calorimeter with a very small energy loss. In mathematical terms it reads:

$$E_T = \sum E_T^{tower} - (\sum E_T^{rawjet} - \sum E_T^{caljet}) + \sum E_T^{Muon}$$

The jet calibration includes a part correcting for out-of-cone losses. Thus the E_T formula implies some double counting. This is a rather small effect and negligible compared to the improvements. A detailed explanation of the MET measurement in CMS can be found in [88]. For the present case a resolution of 30.6% is obtained, compairing the MET due to the two neutrinos and the reconstructed MET (figure 6.18).

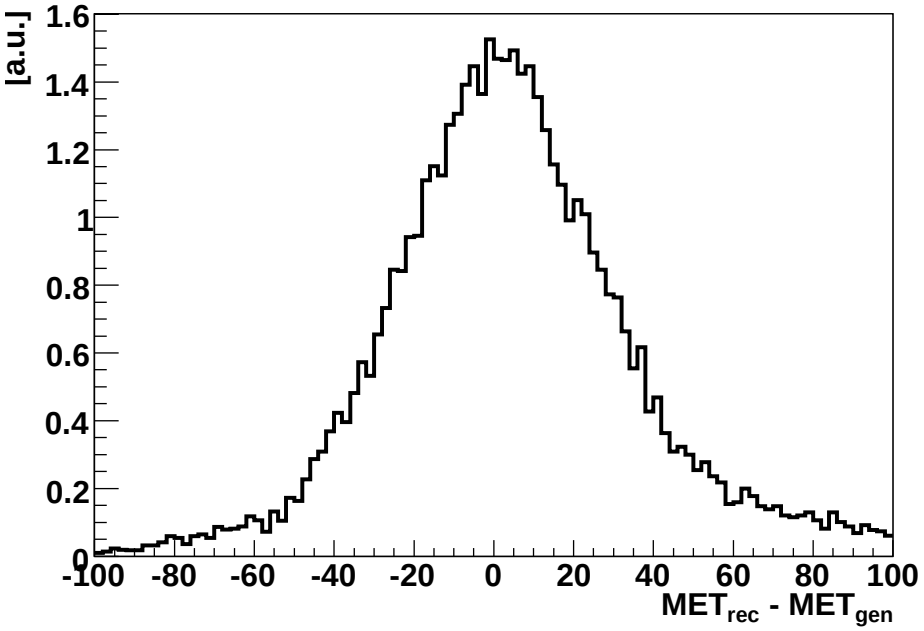

Figure 6.18.: Resolution of the MET reconstruction.

7. Spin–Spin Correlation

After explaining the theoretical base of spin correlations (chapter 4) and the reconstruction of basic objects (chapter 6), this chapter covers the reconstruction of dileptonic $t\bar{t}$ events, the measurement of correlation observables and estimates for the significance of possible results at CMS. The studied observables $\mathcal{O}_1$, $\mathcal{O}_2$ and their parameters A and A_D respectively have been introduced in section 4.5. The base of the study is one year of LHC at a low luminosity, which corresponds to roughly 10 fb^{-1}.

7.1. Signal Definition

As explained in chapter 4 there exist three main classes of $t\bar{t}$ events: the fully hadronic, the semileptonic and the dileptonic decay. For measuring spin-correlations only the semileptonic and the dileptonic channel are of interest, since the combined spin analyzer quality of the final state particles in the fully hadronic case is too low and the background much too high. Comparing the semileptonic and the dileptonic case, both have a very clean signature, yielding good chances of a high signal-to-background (S/B) ratio. The former channel is kinematically very well defined and a has bigger cross section, while the latter has the higher spin analyzing power. Still, both channels are expected to perform comparably strong.

In this thesis the dileptonic channel is explored. Compared to other studies in this channel the definition of dileptonic will be tightened to the $e - \mu$ cases. Decays with τ-leptons are not considered because the additional τ decay dilutes the spin information and with the additional third neutrino the used reconstruction methods are unsuitable for a proper reconstruction of the spin–spin-correlation observables. In fact, those events are the major background contribution in the present analysis. The used definition translates into roughly 400,000 signal events for 10 fb^{-1}.

7.2. Event Selection

The final state of dileptonic $t\bar{t}$ events consists of two leptons with opposite charge, two jets coming from b-quarks and two neutrinos leaving the detector without any signal.

The clean signature of this channel allows already a good selection via cut based methods. Since it turns out that the major uncertainties are neither related to statistics nor to the background uncertainty, but to systematic effects, more advanced selection methods have not been used. This is to facilitate the

interpretation of the results. This is especially important during the investigation of suitable unfolding techniques, which are introduced in section 7.5.

Because of the different signal definition and the different physics under study the selection methods used here deviate in some details from the selections used for other studies in the dileptonic channel [33]. An older, preliminary study on spin correlations at CMS [52] uses comparable cuts and the obtained efficiencies are compatible. A summary table of the cuts explained in the following is given in table 7.1.

7.2.1. Main Background Contributions

As can be seen from figure 3.2 there are many processes with cross sections which are much higher than for this signal. The background can be divided into background yielding the identical final state (physics background) and in background related to mis-reconstruction (instrumental background). Physics backgrounds are events which produce real MET, real leptons and jets from e. g. ISR or FSR. Candidates for such events are (WW, WZ and ZZ) + jets production. Semileptonic $t\bar{t}$ decays and dileptonic decays with either one or two τ-leptons count as physics background as well.

Instrumental backround are usually large cross section processes like QCD multi-jets or Drell-Yan production ($Z/\gamma^\star \rightarrow \ell^+\ell^-$). With jets mis-reconstructed as lepton candidates (fake leptons), $W \rightarrow \ell\nu$ + jets events are also included. They all have in common a low and not significant missing transverse momentum.

The cross sections for the signal and the considered background physics are given in the first row of table 7.1.

7.2.2. Preselection

First the events need to pass both the L1 and the HLT trigger. The selection efficiencies for the $\mu\mu$, μe and ee channels are 88.4%, 79.1% and 77.5% respectively.

According to the final state one expects two leptons and two (b-)jets. Therefore preselection requires at least each two leptons and jets.

7.2.3. Selection

Because of its stability regarding the assumed reconstruction quality the selection developed for the top mass and cross section measurements [33, 89] can be used for the study of spin correlations as well. Two minor adjustments were done. The isolation criteria for the leptons as explained in chapter 6 differ from those studies. While the mentioned studies use a cut on the invariant mass of the two leptons, this cut was not used in the present study. The result of the cuts explained in the following is summarized in table 7.1.

Table 7.1.: Selection efficiencies for signal and the main background contributions. The used criteria are explained in the text. For consistency all cross sections are given in LO in pb.

	Signal	τ	WW	WZ	ZZ	Z+jets	other $t\bar{t}$
Cross section	24.3	30.4	7.74	0.89	11.10	3912	438
Trigger (L1+HLT)	19.4	15.1	4.4	0.37	3.4	657	92
Jets ($2\times E_T > 20\,\text{GeV}$)	11.5	9.8	0.6	0.012	0.06	23.9	73.1
MET $> 40\,\text{GeV}$	9.6	8.1	0.5	0.01	0.03	5.8	53.6
l^+l^-	3.2	0.42	0.04	0.001	0.01	1.17	0.12
b-tag	1.12	0.15	0.002	$\approx 10^{-4}$	$\approx 10^{-5}$	0.02	0.05
Kinematical solver	0.89	0.11	0.001	$< 10^{-4}$	$< 10^{-5}$	0.01	0.03
Mass cut	0.63	0.08	0.001	$< 10^{-4}$	$< 10^{-5}$	$< 10^{-3}$	0.02

At least two jets with $E_T > 20$ GeV

Many of the jets accompanying the di-boson and Z background are soft. A jet E_T cut of 20 GeV, which ensures reasonably reconstructed jets, can suppress them by almost one order of magnitude.

MET

The two neutrinos produced in the decay of the two W bosons in $t\bar{t}$ events cause a significant missing transverse energy, whereas the Drell-Yan and the Z background only have fake MET. Thus a cut on MET is expected to reduce this background. With a cut of MET $>$ 40 GeV the Z+jets background gets significantly reduced.

Two leptons with opposite charge

The two W bosons in the $t\bar{t}$ decay emit two leptons of opposite charge. Demanding two leptons with opposite charge is in particular very strong against non-dileptonic $t\bar{t}$ events, which of course largely survive the former jet related cuts, since the two expected jets are part of their final state as well.

In the preselection explained above only two leptons, but no opposite charge was required. The same-sign events, which are now rejected in the final selection, can give an estimate on the W+jets background, since no charge correlation is expected for those events.

As mentioned in chapter 6, the leptons are demanded to be sufficently isolated. This is to suppress leptons which are not originating from W decays.

Two b-tagged jets

The mono- and diboson background do not necessarily have high energetic b-quarks in their final state, thus the b-tagging information is a powerful discriminator. This cut is in particular very powerful against the remaining Z+jets

background. For the first b-jet a discriminator value of 2 and for the second b-jet a value of 1.5 is chosen. As all $t\bar{t}$ events have similar b-jets behaviour, the relative fraction of signal to $t\bar{t}$ background stays almost unaltered.

Not used cuts

In the ee and the $\mu\mu$ channel one expects a mass peak for the invariant mass of the two leptons in the background. This peak is the Z mass of the Z background. Despite the fact that other studies of cross sections and top masses [33] use an invariant mass cut to suppress this peak, as shown in figure 7.1, it was renounced to take advantage of it. The mass cut directly connects the kinematics of both leptons, which is the same domain as for the correlation observables themselves. Therefore, this leads to a non-trivial shift and a discontinuity in the selected phase space. This yields both theoretical and practical problems for the unfolding routines that need to be applied in the subsequent steps of the analysis.

Even without this cut the Z background is sufficiently suppressed, as can be seen in table 7.1.

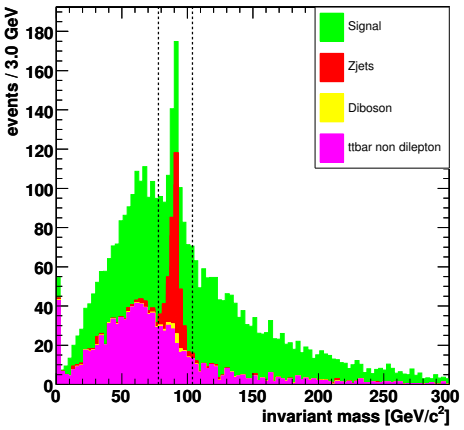

Figure 7.1.: The invariant mass of both leptons could be used to suppress the Z background. While this cut was used successfully in other studies, the cut is rejected for the study of spin correlations. [33]

7.2.4. Selection Summary

Already with a simple cut based selection, the final signal-to-background ratio is 5.2 : 1. The $t\bar{t}$ background has the biggest contribution. The other background is smaller by about one order of magnitude. Further suppression of the top-pair background happens during the kinematical reconstruction of the full event. The final S/B ratio is 6.3 : 1. For the final analysis in total 14,700 signal and 1,800 background events are left.

7.3. Event Reconstruction

The selected events are reconstructed using the physics object definitions as introduced in chapter 6. The visible final state of dileptonic top-pair events consists of two b-jets and two leptons, wich have to be selected from the reconstructed objects.

Lepton selection

After reconstruction there are usually more than two reconstructed leptons in the event, as shown in figure 7.2). To select the right leptons one can take advantage of the overall kinematics. From SM calculations the expected leptons are mainly emitted with low η and high p_T values. A simple parameter using this behaviour is the sum of the transversal momenta of both leptons, namely $|p_T^{l^-}| + |p_T^{l^+}|$. This simple approach already yields very good results, the right particles are chosen in 98% of the cases.

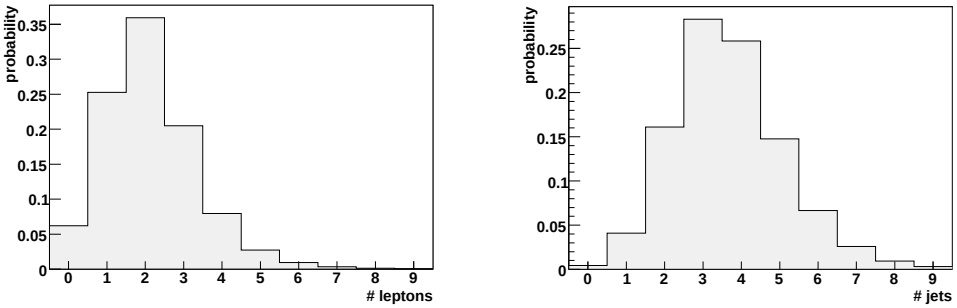

Figure 7.2.: Number of leptons (left) and jets (right) after reconstruction. The proper leptons and jets have to be selected.

B-jet selection

As the requirement for two jets with a high b-tag discriminator is too rigid for sufficient statistics, the b-tag information cannot be used for identifying both proper jets in the selected events. Instead the jet with the highest b-tag is taken and the second b-jet found by searching for the maximum p_T.

Neutrino information

After having selected both leptons and both b-jets, there are yet two missing particles in the final state. Since the two neutrinos are leaving the detector without interaction almost all information about their momenta is lost. Only the information about the missing transversal energy conserves some information:

$$\begin{aligned} E_x &= p_{\nu_x} + p_{\bar{\nu}_x} \\ E_y &= p_{\nu_y} + p_{\bar{\nu}_y} \end{aligned} \tag{7.1}$$

7.3.1. Kinematical Reconstruction

Combining the information of the selected objects with some kinematical constraints, the full kinematics of the $t\bar{t}$ process can be reconstructed. Setting the neutrino mass to zero, which is a good approximation, one can simplify further calculations:

$$E_\nu^2 = p_{\nu,x}^2 + p_{\nu,y}^2 + p_{\nu,z}^2 \tag{7.2}$$

$$E_{\bar{\nu}}^2 = p_{\bar{\nu},x}^2 + p_{\bar{\nu},y}^2 + p_{\bar{\nu},z}^2 \tag{7.3}$$

Other kinematical constraints for the event are the invariant mass of both W-bosons:

$$\begin{aligned} m_{W^+}^2 = (E_{l^+} + E_\nu)^2 - (p_{l^+,x} + p_{\nu,x})^2 \\ -(p_{l^+,y} + p_{\nu,y})^2 - (p_{l^+,z} + p_{\nu,z})^2 \end{aligned} \tag{7.4}$$

$$\begin{aligned} m_{W^-}^2 = (E_{l^-} + E_{\bar{\nu}})^2 - (p_{l^-,x} + p_{\bar{\nu},x})^2 \\ -(p_{l^-,y} + p_{\bar{\nu},y})^2 - (p_{l^-,z} + p_{\bar{\nu},z})^2 \end{aligned} \tag{7.5}$$

and both top quarks:

$$\begin{aligned} m_t^2 = (E_b + E_{l^+} + E_\nu)^2 - (p_{b,x} + p_{l^+,x} + p_{\nu,x})^2 - \\ (p_{b,y} + p_{l^+,y} + p_{\nu,y})^2 - (p_{b,z} + p_{l^+,z} + p_{\nu,z})^2 \end{aligned} \tag{7.6}$$

$$\begin{aligned} m_{\bar{t}}^2 = (E_{\bar{b}} + E_{l^-} + E_{\bar{\nu}})^2 - (p_{\bar{b},x} + p_{l^-,x} + p_{\bar{\nu},x})^2 \\ -(p_{\bar{b},y} + p_{l^-,y} + p_{\bar{\nu},y})^2 - (p_{\bar{b},z} + p_{l^-,z} + p_{\bar{\nu},z})^2 \end{aligned} \tag{7.7}$$

In total we have as many unknowns ($p_{\nu,x}$, $p_{\nu,y}$, $p_{\nu,z}$, $p_{\bar{\nu},x}$, $p_{\bar{\nu},y}$, $p_{\bar{\nu},z}$) as kinematical constraints ($m_{W^+}, m_{W^-}, m_t, m_{\bar{t}}, E_{T,miss}$). This makes higher level methods like kinematic fitting impossible. The equations can be transformed into a polynom in fourth order of one of the unknown neutrino momenta compontents, only using known values as input [90]:

$$\sum_{i=0}^{4} c_i \left(p_{l^+}, p_{l^-}, p_b, p_{\bar{b}}\right) \left(p_\nu^x\right)^i = 0 \tag{7.8}$$

All other values can then be calculated from the found solution. There exist both algebraic [91] and analytical [92, 90] methods to solve the polynomial equation. Both lead to a four-fold ambiguity in the solution, two for each neutrino. In this study the algebraic approach as proposed in [91] is used. The input of the algorithm are the four masses ($m_{W^+}, m_{W^-} m_t, m_{\bar{t}}$), the four momenta ($p_b, p_{\bar{b}}, p_{l^+}, p_{l^-}$), and the two components of the missing transversal energy.

7.3.2. Solver quality

The algorithm was tested in the kinematical regions of LHC. A summary of the obtained results is listed in table 7.2. In the ideal case where the known off-shell masses are used as input, a solution is obtained in 99.8% of the cases.

In almost all of the cases (99.7%) the solution is within numerical precision. This is very close to the results for the kinematical regions of Tevatron at 1.96 TeV [91].

Using the perfect generator information from the final state particles and the exact per-event mass of the top quarks and the W-bosons as additional parameters, the efficiency is almost perfect. Assuming zero-width of the W-bosons, the efficiency drops by 8.5%. Using the pole mass for both t and W, which is the assumption for the real reconstruction, the solver delivers a solution in 88.4% of all cases. If wrong l–b pairing is allowed, the efficiency slightly increases.

Testing the solving routine on reconstructed objects, the efficiency is still very high. Using the right l–b pairing a solution is obtained in 72.3% of the cases. The efficiency increases to 96.2% once iterative smearing of input objects and input parameters is applied. This will be explained in section 7.3.4 below.

Table 7.2.: Event solver performance for different input quality.

	solvability
Known t and W off-shell masses	99.8%
Known W mass, t pole mass	91.3%
Pole masses of W and t	88.4%
both l–b combinations	90.1%
Reconstructed objects (right pairing)	72.3%
Reconstructed objects (wrong pairing)	36.7%
Reconstruced objects (both pairings)	81.1%
Reconstructed objects (smeared)	96.2%

As can be seen from figure 7.3 the pairing purity of the solutions increases quickly for higher $\sqrt{\hat{s}}$. For reasons explained in chapter 4 a cut on 550 GeV is applied and this behaviour cannot be utilized. But it looks promising for differential spin-correlation measurements for higher statistics than 10 fb^{-1}.

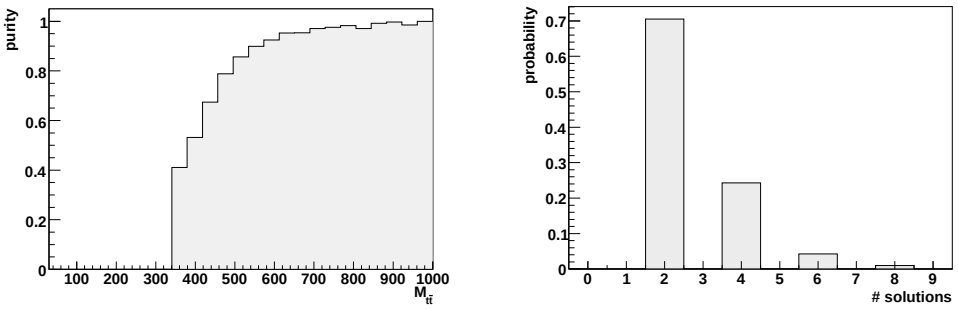

Figure 7.3.: Left: the probability to get a solution for the wrong pairing decreases with higher energies. Right: total number of solutions taking both pairings into account.

Comparing the overall purities for Tevatron [91] and the kinematical regions

of LHC, the better result for the latter can be explained by the higher contribution of high $m_{t\bar{t}}$ events.

7.3.3. Selecting the Right Solution

In figure 7.3 (right) the number of solutions using both pairing hypotheses is shown. Still one needs to find out which solution is the correct one. Several methods have been proposed using the kinematical behaviour of $t\bar{t}$ events [52, 90]. Among those are weighting the solutions via the p_T spectra of the top quarks or the neutrinos, or a combination of both (see figure 7.4). Especially the neutrino spectrum could be obtained in the semi-leptonic $t\bar{t}$ channel and would not be limited to pure Monte-Carlo assumptions.

For the present study a combination of the probabilities for both top spectra and one neutrino spectrum

$$P_{solution} = P_{p_T^{\nu}} \cdot P_{p_T^{t}} \cdot P_{p_T^{\bar{t}}} \tag{7.9}$$

was found to yield the best results. With a probability of 68% the right solution was chosen, which is compatible with other studies [52]. Including the second neutrino information into the weighting causes a visible bias in the spin observables. Both neutrino spectra are correlated via the kinematics of spin–spin-correlations. This and the fact that the probability of obtaining the right solution was only increased by about 1%, lead to the decision not to use the second neutrino information.

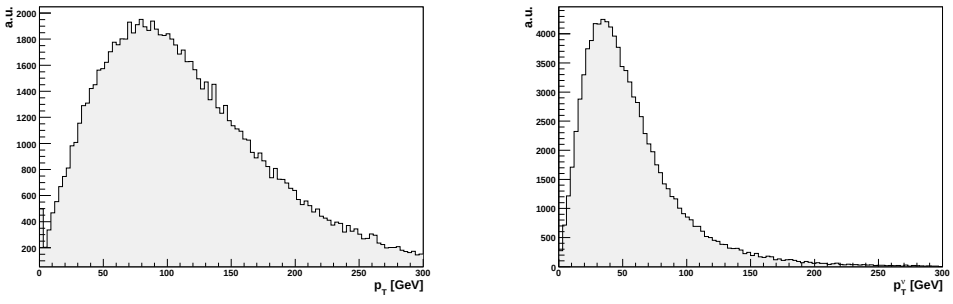

Figure 7.4.: The p_T spectra used for weighting the kinematical hypotheses. On the left the p_T spectrum of the top quarks. It is almost independent from the production process and thus not biasing; on the right the neutrino spectrum. Both are combined into a probability for weighting the multiple event hypotheses.

7.3.4. Influence of Smearing on the Solver Efficency

As one can see from table 7.2 there are two reasons that reduce the efficiency of the used solving routine. One of them is the assumption of purely on-shell processes, the other one is the smearing due to the detector resolution. It was tested if taking these effects into account, the solver efficency can be increased.

In fact the efficiency increases to 96.2%. Unfortunately the higher efficiency of the kinematical smearing does not improve the final results, but the results are either getting worse or biased. This will be explained in the following.

Resolution Smearing

Taking the limited detector resolution into account some properly selected events are not solvable in means of the kinematics. An approach to increase the solver efficiency is varying the input objects. The inputs to the solver, namely p_{l^+}, p_{l^-}, p_{jet_1} and p_{jet_2} are smeared according to the detector resolution, as studied in chapter 6. Only MET is not taken into consideration but is used to absorb the changes of the other quantities.

To anticipate results of following sections, the migration of the observable is significantly increased and thus the method rejected here. Still the increase of the solver efficiency is signifcant and a further investigation how to take advantage of this is needed. One possible approach would be to introduce an event quality weighting based on the number of smearing iterations until a solution is obtained.

Masses as free parameters

Apart from the measured momenta, there exist other quantities that go into the solving routine, the two W masses and the two top masses. Using these four quantities as free parameters during the iterative solving procedure is not feasible. The two top masses could be considered free parameters. Since the goal of this analysis is not the top mass measurement, m_t can be used as known input. The clean physical approach for smearing would now be varying it with its mass width. As already mentioned in chapter 4 the measured upper bound to the top mass width is still one order of magnitude bigger than the theoretical prediction. Hence it is not known well enough for this approach. More over the spin–spin correlation is to a certain extend dependend on the top mass width. Introducing the measured or even the predicted width at this level is not sensible. Therefore and because smearing of the top and the W masses increases the migration significantly, the mass smearing is rejected as well.

7.4. Spin-Spin Observables

With the $m_{t\bar{t}} < 550$ GeV cut, the input correlation parameters as defined in chapter 4 are determined to be $A = 0.422$ and $A_D = -0.290$. After selection and reconstruction all information for doing the actual measurement is available. Figure 7.7 shows the obtained distribution for the double differential distribution and fig. 7.9 the one for the opening angle. Both distributions are completely distorted compared to the inital distributions. This is mostly due to the fact that the selection efficiency is very sensitive to the measured angles.

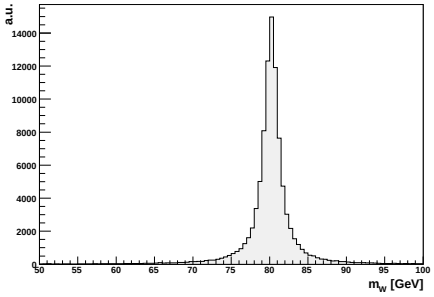

Figure 7.5.: The generator mass of the W bosons.

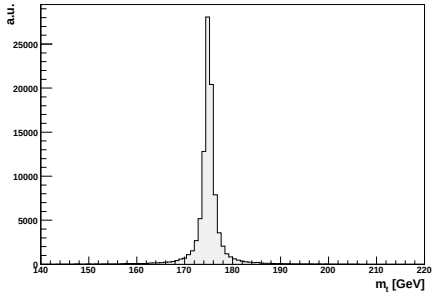

Figure 7.6.: The generator mass of the top quarks.

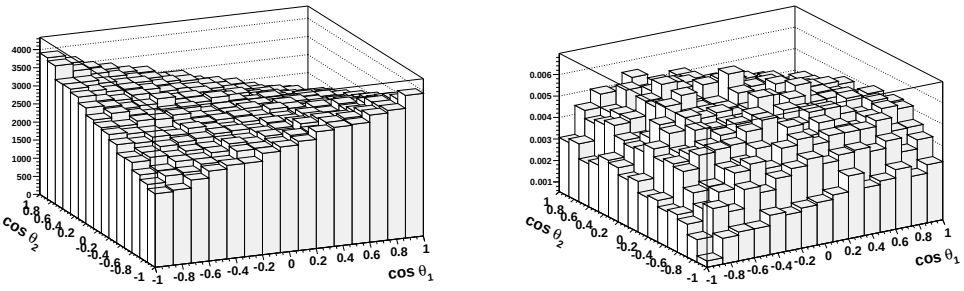

Figure 7.7.: Double differential distribution after selection and reconstruction. The initial distribution (left) gets transformed into the completely differently reconstructed histogram (right).

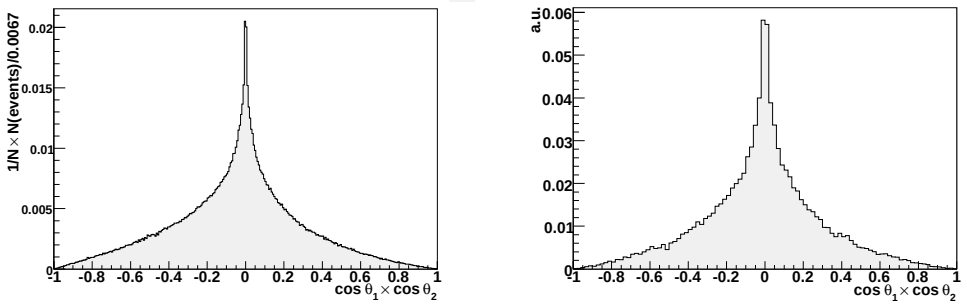

Figure 7.8.: Dilution of the spin asymmetry observable $\cos\theta_1 \times \cos\theta_2$. On the left the initial generator information. On the right the result after selection and reconstruction.

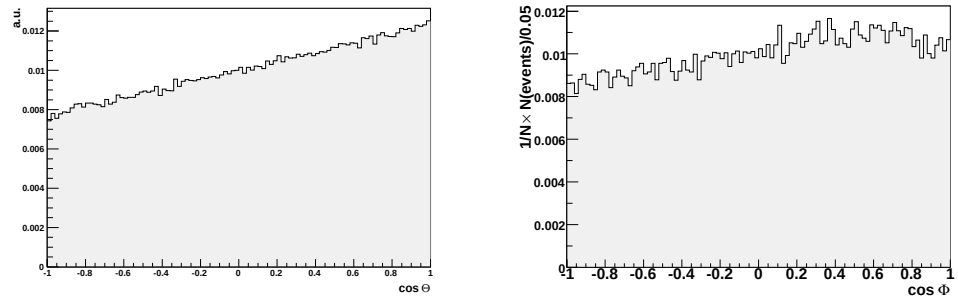

Figure 7.9.: Dilution of the opening angle distribution. On the left the initial generator information. On the right the result after selection and reconstruction.

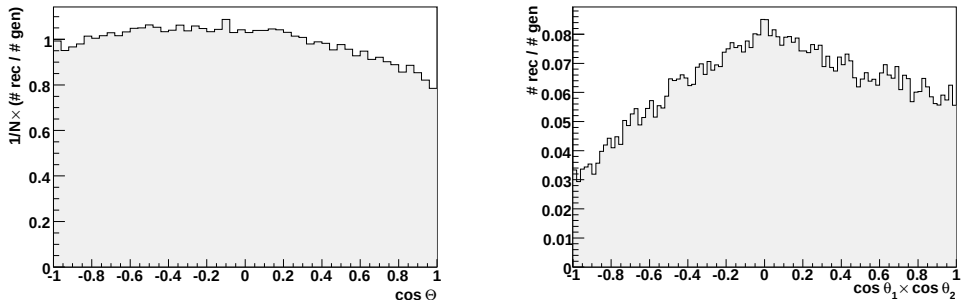

Figure 7.10.: On the left the efficiency for A_D, on the right the efficiency for A comparing the information before and after selection.

7.4.1. Selection efficiencies

The obtained selection efficiency is shown in figure 7.10. The one-dimensional projection is chosen for comparison with other studies. This plot is calculated based on the comparision of generator information for the original sample and the sample after reconstruction and cuts. As can be seen especially the left part of the A distribution has a very low efficiency. Which is unfortunately the more interesting part of the distribution, since for the SM case of correlation this side of the distribution would be pronounced.

The efficiency distribution can be understood by looking at the according event kinematics. For simplicity only the corners of the two-dimensional distribution ($\cos\theta_1 = \pm 1$ and $\cos\theta_2 = \pm 1$) are considered. For the sake of clarity, the center of mass system of the production process is assumed to be at rest. The two top quarks are flying back-to-back. For the flight direction of the leptons coming out of the process there are four border cases indicated in figure 7.11 (left). Either both leptons are emitted in the direction of the corresponding top and get a boost. Those leptons will be clearly visible in the detector. In the case where both are emitted against the direction of the top, both leptons get a negative boost and will be low energetic in the lab frame. Thus the selection efficiency will be lower. In the mixed case the leptons are

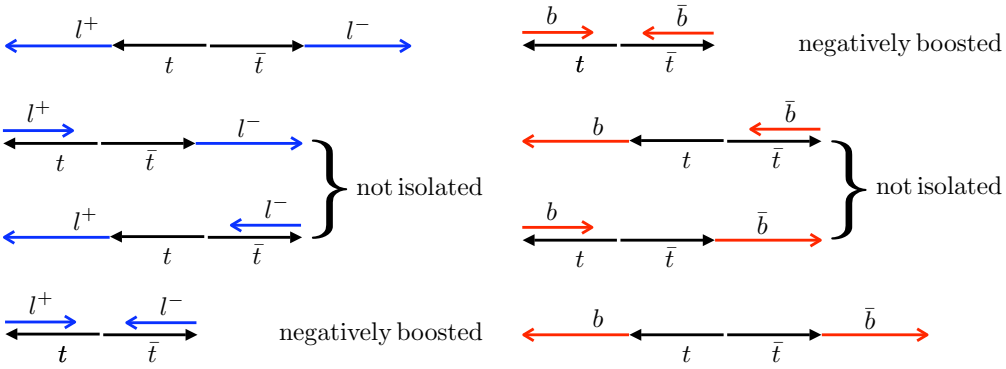

Figure 7.11.: A simplified view of the kinematics for the four border cases of the double differential distribution. A superposition of all these effects leads to the shape of the acceptance function.

not isolated and again the efficiency drops. The same holds, less strong, for the b-jets as shown on the right hand side of figure 7.11. In reality it is not that easy and there is a superposition of all those effects leading to the complicated shape of the acceptance function.

7.4.2. Migration

After selection and reconstruction not only the efficiencies change the shape of the resulting distribution, but the experimental resolution of the reconstructed objects as discussed in chapter 6 leads to significant migration. How huge the migration effect is, is shown in figure 7.12. This level of migration causes the need for advanced unfolding techniques as explained in the section 7.5 further below.

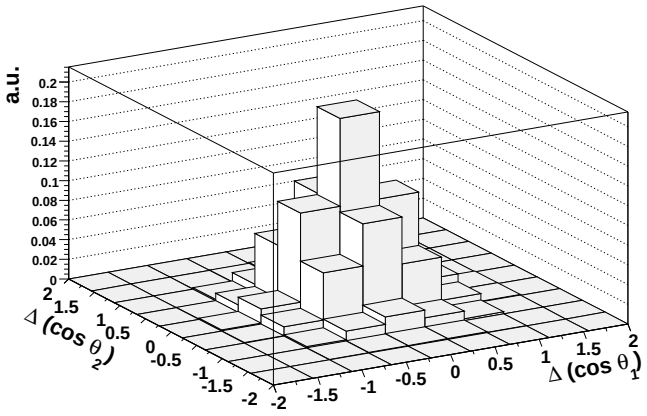

Figure 7.12.: Migration of the helicity angles $\cos\theta$. Plotted are the differences between generated and reconstructed value.

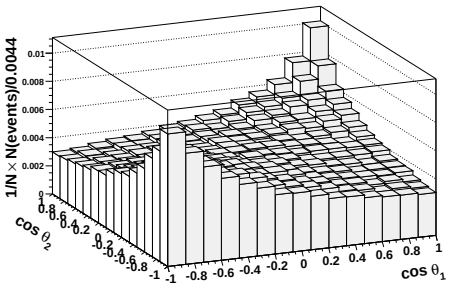

Figure 7.13.: Double differential distribution with wrong pairing

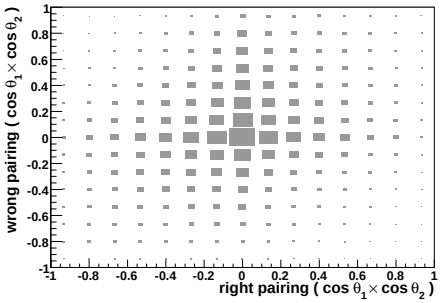

Figure 7.14.: Migration due to wrong pairing

Wrong pairing

One main problem not directly connected to the detector resolution is the wrong assignment of b-jet and lepton. This combinatorial background is suppressed by the lower chance of getting a kinematical solution, but it still has a significant contribution. As it turns out the fake spin information for the wrong pairing is almost opposite to the real signal. Figure 7.14 shows the double differential distribution for wrong pairing on parton level. As can be seen the wrong pairing has huge effects on the measured correlation observable.

Thus it is essential to understand the fraction of wrong combinatorics and to keep it as low as possible. As mentioned earlier in section 7.3.4 using smearing to improve the reconstruction efficiency increases migration significantly. This can now be understood due to more wrong combinations created.

7.5. Unfolding procedures

As explained above two main effects disturb the analysis. These are varying efficiency through the whole phase-space and migration effects. Going back from measured data to the parton level quantities is one special case of so-called unfolding procedures. There are several methods developed and used in high energy physics [93, 94, 95].

In the mathematical sense unfolding is a simple deconvolution problem. Given $f(x)$ is the distribution and $g(y)$ the measured distribution, both are connected via

$$g(y) = \int_x R(x) f(x) + b(y), \tag{7.10}$$

where $R(x)$ is the (detector) response function and $b(y)$ an additional (independent) background contribution. To simplify the theoretical discussion below, all quantities are assumed to be discrete. Then equation 7.10 transforms into:

$$y_i = \sum A_{ij} x_j + b_i. \tag{7.11}$$

In the following some methods to solve this deconvolution problem are explained.

Matrix inversion: Assumed the true and the measured distribution have the same binning. The quadratic matrix A_{ij} can be tried to be inverted, giving the following expression:

$$x_j = A_{ij}^{-1} (y_i - b_i) \tag{7.12}$$

In general the matrix cannot be assumed to be invertible. So this simple approach will work only in exceptional cases. In addition it is very likely that the resulting distribution will have a very fluctuating shape. Therefore this naïve approach is not used.

Bin-by-bin correction is another very naïve approach. In mathematical terms the matrix A_{ij} is assumed to be purely diagonal. This method is only feasible in case of small migration effects. How badly this method performs for the problem under study can be seen in figure 7.15 and in [96], where this method is rejected as well.

Fitted bin-by-bin correction or parameterized unfolding is the method used in the ATLAS studies to spin–spin-correlations. For different values of the quantity that will be measured correction functions are provided. Each iteration an updated correction is applied until the procedure converges. The drawback is that this method introduces assumptions about the kind of expected distribution at a very early level. Probably due to these strong assumptions the method performes and converges particulary well for the present case.

Histogram fitting is not an unfolding method, but comparable to the fitted bin-by-bin correction. Here g_j is not transformed back to f_i, but $f(x)$ is split into several parts being a base of the to be explored phase space, i. e. the later fitting function. For each part g_{theor} is calculated separately and the fitting of g_{exp} is done only in the codomain. This approach is equivalent to the former method, only the minimization happens at different places, either in the domain or the codomain.

For spin–spin-correlations base histograms of choice are for example the four spin states as shown in figures 5.1ff.

Bayesian unfolding is based on the Bayes' theorem and is explained in the following section. Except for the starting value the algorithm does not need to make assumptions about the expected distribution. Nevertheless, using the shape of the final distribution for smoothing, the speed of convergence can be increased.

Regularized unfolding is an approach to remove the problems of the simple matrix inversion. One widely used tool is the program *RUN* [97]. Here the regularization is based on the minimatization of curvature. In general the choice of the regularization method is a non-trivial problem

resulting in quite diverging flavours of unfolding. This and the fact, that the other applied methods turn out to be more than sufficient, leads to the rejection of this approach for the present case.

7.6. Bayesian Unfolding

In the following the less rigid notation of [95] is used. The foundation of the Bayesian unfolding is Bayes' theorem connecting conditional probabilities

$$P(C|E) = \frac{P(E|C)P(C)}{P(E)}, \tag{7.13}$$

where C is the *cause* (true value) and *effect* (measured value).

In case of more causes and effects, e.g. bin frequencies of a physics distribution the formula can be extended to:

$$P(C_i|E_j) = \frac{P(E_j|C_i)\ P(C_i)}{\sum_{l=1}^{n_C} P(E_j|C_l)\ P(C_l)} \tag{7.14}$$

This is a very general approach. In particular the number of causes and effects do not need to be identical. Here the causes and effects are simply bin entries in histograms. For simplicity the binning is chosen to be identical. The conditional probability $P(E_j|C_i)$ is the knowledge of how efficiencies, migration and other effects dilute a true quantity to a measured one. This folding matrix is calculated from parton level and full simulation information. $P(C_i|E_j)$ is the probability of the true values C_i given the measured quantities E_j, i. e. the unfolding matrix. And finally $P(C_i)$ is the true distribution to be measured.

Bayesian unfolding uses this equation for an iterative solving routine. Starting point is a histogram $P_0(C_i)$ which is chosen according to an initial hypothesis. For this study the two natural choices are either the expected SM spin correlation or a completely unbiased flat distribution. This distribution is then smeared via $P(E_j|C_i)$. The via equation 7.14 resulting $P(C_i|E_j)$ can be used for unfolding the measured distribution.

Given the measured histogram with the entries $n(E_j)$, the corresponding unfolded histogram can be calculated via:

$$n(C_i) = \sum_j P(C_i|E_j)n(E_j) \tag{7.15}$$

This replaces the old histogram $P_0(C_j)$. Summed up the Bayesian unfolding algorithm is as follows:

1. The conditional probabilities $P(E_j|C_i)$ are calculated from signal and background MC. Smoothing of the distribution can be applied.
2. The initial primer $P_0(C_i)$ is set as flat distribution in the signal part and to the MC value for the background.
3. Bayes' theorem is used to calculate $P(C_i|E_j)$.

4. From formula 7.15 the updated $n(C_i)$ are calculated. The old and the new numbers are compared. If the difference is smaller than a certain distance, the algorithm is stopped. Else, the new values are used as starting point for a new iteration starting with step two.

The tool developed for this thesis is available through [98]. Comparable C++ or Fortran implementations already exist [99, 100]. Other Bayesian based unfolding methods are described in [101].

7.6.1. Other causes

The causes in the Bayesian unfolding are not limited to simple histograms or signal distributions. An alternative for the causes could be the eight partitions of four contributions (constant, two polarizations, correlation) times two production processes. This would be almost equivalent to the approach of histogram fitting. Studies of these alternative causes have to be done in a latter study and are left open here. The advantage of using more causes would be to factor out the actual spin–spin-correlation from other effects that influence it.

7.7. Comparison of Methods

The methods explained in section 7.5 have been compared in order to see their advantages and disadvantages. This comparison is far from being complete and only a snapshot of the methods used throughout the literature about spin correlations. Base for the comparison are a tune sample of 400,000 events for obtaining the needed MC primers, and a to be unfolded 'signal' sample of the same size.

In table 7.3 and figure 7.15 the result of the fitted bin-by-bin correction for different starting values is shown. The 0th iteration step is identical to a simple bin-by-bin correction. As can be seen easily the simple correction performs very poorly. This gets reflected in the statistical uncertainty one obtaines from this method, which is significantly worse than for other methods. In comparison, the improved fitting correction converges reasonably fast and yields very good results. Especially for the opening angle observable A_D the algorithm converges rather quickly. Figures 7.16 and 7.17 show the behaviour of the algorithm for different starting values.

The Bayesian unfolding, which was tested as well, performs almost identical on the final values. On average it needs one iteration less, though the assumptions on the final distribution are much weaker. Still this can be sometimes seen in the intermediate steps, which are not forced to be reasonable from the physics point of view. The result of unfolding the measured distribution 7.8 is shown in 7.18. Though no assumptions on the final shape were made, the fluctuation of the histogram is reasonable small.

As summary both the parameterized and the Bayesian approach seem to be well suited for performing unfolding in spin correlation studies. Both methods are able to detect spin correlations different from SM predictions and are not

Table 7.3.: Convergence of the iterative unfolding routine for fitted bin-by-bin corrections. A ″+″ indicates termination of the iteration. The starting point for this test of the algorithm is the SM prediction for the asymmetry parameter A. The column ″0″ is the correction after trivial bin-by-bin correction. Because of yielding comparable results the histogram fitting is omitted.

True value	0	1	2	3	4	5
0.0	0.169	0.066	0.025	0.012	0.006	0.002
0.1	0.231	0.148	0.118	0.107	0.100	+
0.2	0.299	0.235	0.209	0.200	+	+
0.3	0.347	0.318	0.309	0.301	+	+
0.4	0.405	0.402	0.400	+	+	+
SM	+	+	+	+	+	+

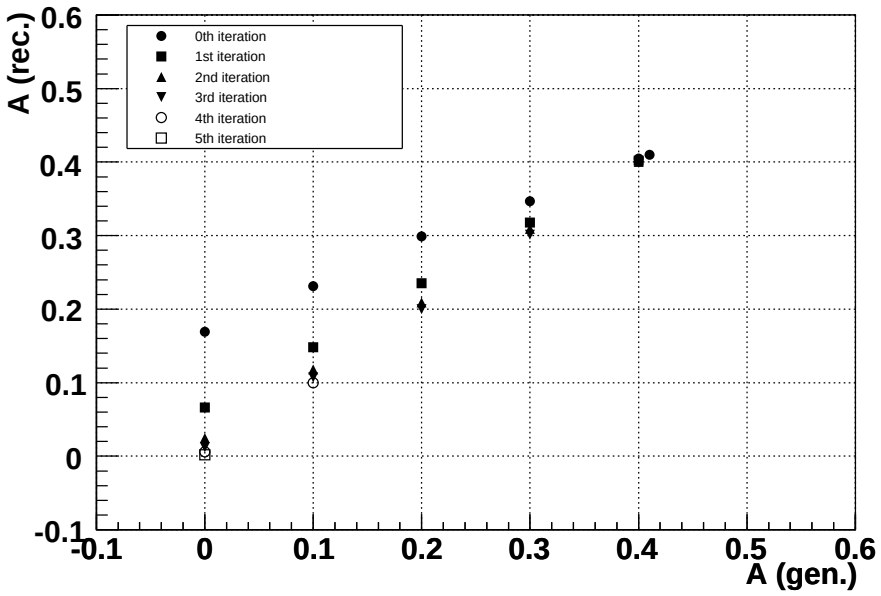

Figure 7.15.: Unfolding of observable A with different start values. During the iteration steps the computed value gets closer to the input value.

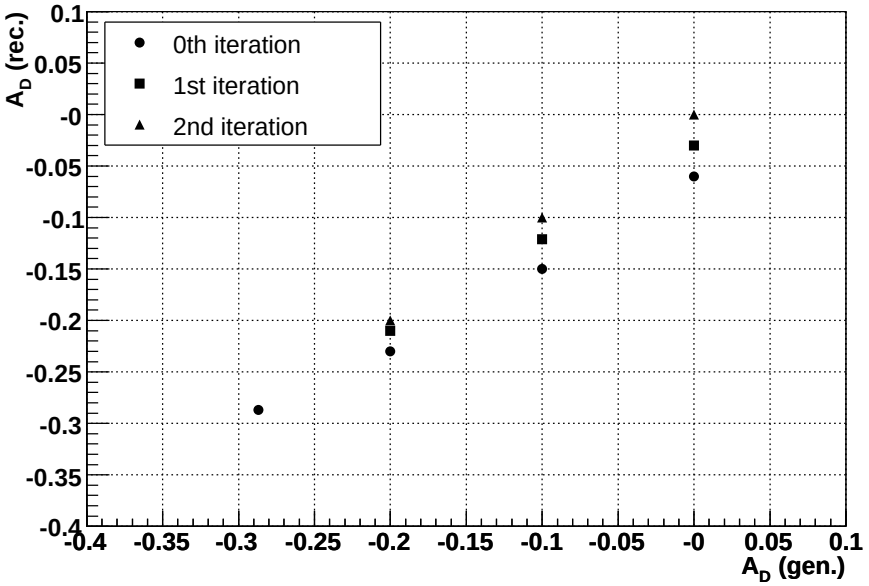

Figure 7.16.: Unfolding of observable A_D. Starting assumption for the unfolding procedure is the SM prediction $A_D = -0.287$.

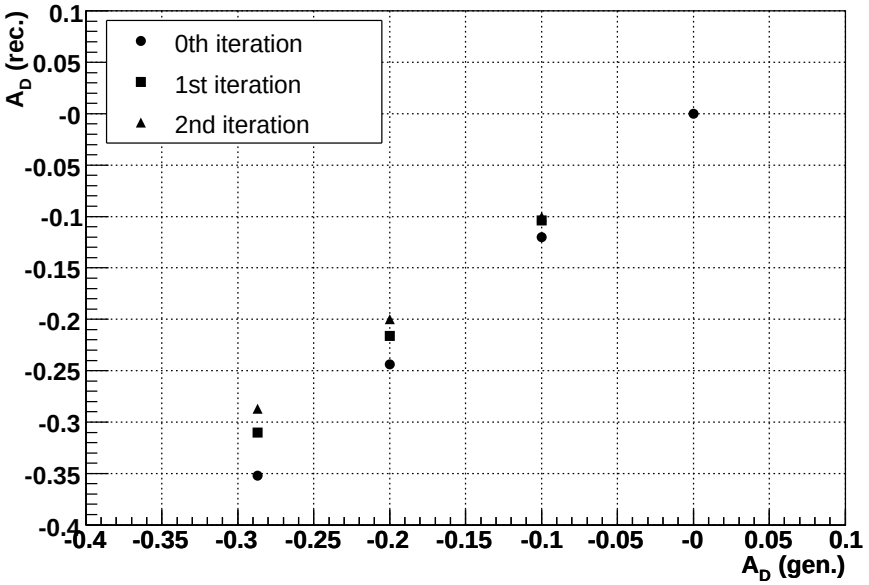

Figure 7.17.: Unfolding of observable A_D. Starting assumption is a parameter of $A_D = 0.0$.

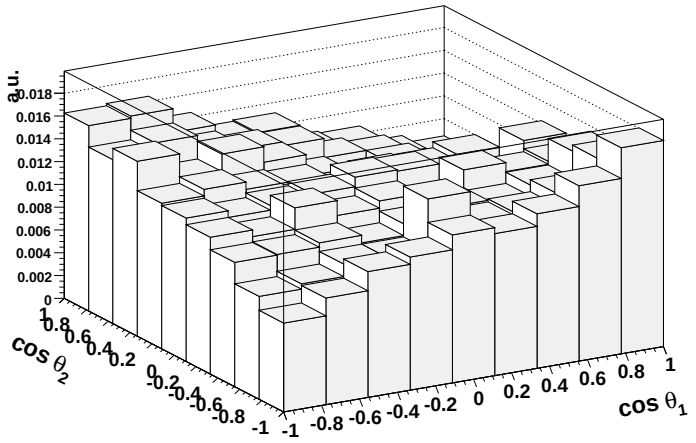

Figure 7.18.: Spin–spin-correlation distribution after application of Bayesian unfolding.

biased towards the SM value. Because of making less strong assumptions the Bayesian driven unfolding approach is prefered and used in the following.

7.7.1. Mixing non SM spin–spin-correlations

To be able to produce table 7.3 different sets with different values of the spin correlation parameters were needed. A discussion on different ways of obtaining such samples is given in appendix B. For the present case the helicity states as shown in figures 5.1ff were mixed to build appropriate samples.

7.8. Background Contributions

In terms of spin-correlation the background seems to be reasonable uncorrelated as can be seen in figure 7.19. The dependency of the background shape on the input spin-correlation was found to be negligible. Therefore a simple background substraction method is chosen. The error of this approach is estimated in section 7.10.2.

7.9. Statistical Uncertainties

The number of bin entries in the unfolded distribution C_i can be expressed in terms of the measured distribution E_j like follows [95]:

$$C_i = \sum_j M_{ij} E_j \tag{7.16}$$

Because of the huge migration the C_i cannot be treated as uncorrelated. Therefore one needs to know the covariance matrix V composed from the uncer-

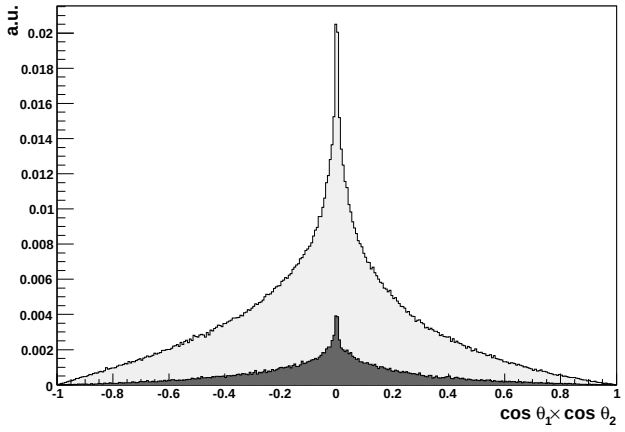

Figure 7.19.: Signal (grey) and background contribution (black) for the measurement of A. The background has the shape of an uncorrelated sample.

tanties coming from the statistically limited measurement of E_j and the uncertainties arising from limited Monte-Carlo statistics, which is used for (iteratively) obtaining the unfolding matrix M:

$$V = V(E) + V(M) \tag{7.17}$$

The measurement uncertainty is given by

$$V_{kl}(E) = \sum_j M_{kl} M_{ij} E_j \left(1 - \frac{E_j}{N}\right) - \sum_{i,j,i\neq j} M_{kl} M_{ij} \frac{E_i E_j}{N}, \tag{7.18}$$

while the uncertainty of the unfolding can be written as:

$$V_{kl}(M) = \sum_{i,j} E_i E_j \cdot Cov(M_{kl}, M_{ij}). \tag{7.19}$$

The latter expression does not contain systematic effects from MC. Those are discussed in the following sections.

Evaluation

For the present case 400,000 events were used for obtaining the needed conditional probabilities $P(E_j|C_i)$. As 'signal' another set of the same size resulted in 14,700 selected events. The evaluation of the statistical uncertainty depends on the final result. Using the Standard Model prediction leads to the following statistical uncertainties:

$$\begin{aligned} \sigma_{stat.}(A) &= 0.032 \\ \sigma_{stat.}(A_D) &= 0.014 \end{aligned} \tag{7.20}$$

Extrapolating the uncertainty to unlimited MC statistics for tuning the conditional probabilities, the uncertainty can be improved to roughly

$$\begin{aligned} \sigma_{stat.}(A) &\approx 0.02 \\ \sigma_{stat.}(A_D) &\approx 0.01 \end{aligned} \tag{7.21}$$

7.10. Systematic Uncertainties

As already mentioned there are many places for systematic effects. In the following the CMS guidelines from [102] were used to estimate theses uncertainties.

The systematic uncertainties can be divided into theoretical and instrumental uncertainties. The former could mainly be checked at generator level. In contrary, the systematics of instrumental uncertainties was done using full simulation samples. As the spin–spin-correlation is a very subtle effect, the study could not rely on fast simulation for systematic studies. Throughout full simulation samples were generated and used. Similar observations concerning the feasibility of intermixing fast- and full-simulation studies were done in [103].

7.10.1. Theoretical uncertainties

Hard Process Scale

To estimate the uncertainty due to the Q^2-scale, it was tested for the scenarios $p_T(t)^2 + M_T^2$ and M_t^2. The estimate for the uncertainty is:

$$\begin{aligned} \Delta A &= 0.013 \\ \Delta A_D &= 0.003 \end{aligned} \tag{7.22}$$

PDF uncertainty

As the spin correlation is highly dependend on the production process, it is expected that the spin correlation is very sensitive to the input parton density function. Several PDFs (CTEQ5L, CTEQ6L and MRST2002) have been compared and the maximum difference has been taken as systematic uncertainty. As conservative assumption the PDF uncertainty is taken as independently from the above mentioned changes to the Q^2 scale. The error was found to be:

$$\begin{aligned} \Delta A &= 0.008 \\ \Delta A_D &= 0.005 \end{aligned} \tag{7.23}$$

The cleaner approach would have been to use the errors of CTEQ6L directly [104], but this was not possible because of the needed statistics and limited computing resources.

Underlying Event

During the pp-collision, not only the hard scattering process creating the $t\bar{t}$-pair is happening. There are other outgoing particles, commonly called *underlying event*. In order to estimate the contribution to the systematic uncertainty, the parameter steering the colour screeing p_T cut off was modified. No significant changes to the observables have been found.

Initial State and Final State Radiation

During the physics process partons can radiate other particles, like gluons or photons. This is either called Initial State (ISR) or Final State Radiation (FSR). The influence was checked by modifiying the Pythia parameters steering the strength of this radiation. According to the used values described in [33], the values of Λ_{QCD} and Q^2_{max} were changed consistently in two additional scenarios. The obtained changes are:

$$\begin{aligned} \Delta A &= 0.003 \\ \Delta A_D &= 0.001 \end{aligned} \tag{7.24}$$

7.10.2. Instrumental Uncertainties

Jet Energy Scale and Jet Calibration

The consideration of jet energy scale and resolution follows the commonly agreed CMS guidelines [105]. The uncertainty due to the JES is studied by shifting the jet energies systematically up or down by a relative percentage. The actual percentage depends on the transverse momentum of the jet. For a transverse momentumabove 50 GeV, the uncertainty is expected to be 3%, because calibration methods like the hadronic W-boson mass in tt events are expected to be working well at this energy. In the low p_T region down to 20 GeV, where the W-boson mass calibration is not available, the energy scale will be set by the γ + jet calibration leading to a linear increase of the uncertainty from 3% to 10%. Below 20 GeV, only single particle calibration methods are possible with an accuracy of 10%. This leads to the following functional form of the jet energy scale uncertainty:

$$\frac{\sigma_E}{E} = \begin{cases} 10\%, & \mathrm{p_T} < 20\,\mathrm{GeV/c} \\ 10\% - 7\% \cdot (\mathrm{p_T} - 20\,\mathrm{GeV/c})/30\,\mathrm{GeV/c}, & 20\,\mathrm{GeV/c} < \mathrm{p_T} < 50\,\mathrm{GeV/c} \\ 3\%, & \mathrm{p_T} > 50\,\mathrm{GeV/c} \end{cases} \tag{7.25}$$

which is schematically shown in figure 7.20. The shift of the results is:

$$\begin{aligned} \Delta A &= 0.015 \\ \Delta A_D &= 0.004 \end{aligned} \tag{7.26}$$

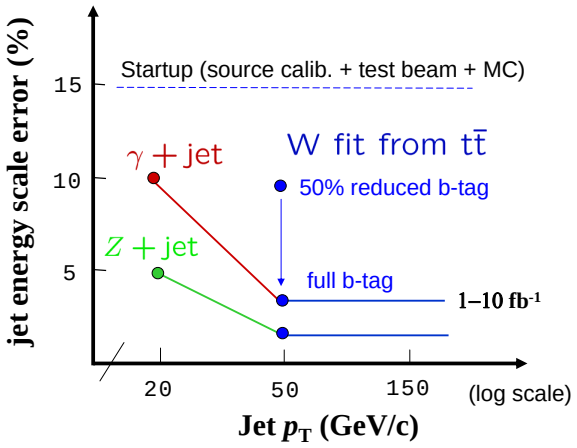

Figure 7.20.: Estimates for the jet calibration uncertainty. [33]

B-tagging Performance

The estimated uncertainty of the B tagging is shown in figure 7.21. For 10 fb^{-1} the error was assumed to be 3% in the barrel and 6% in the endcap region for the working point of 55%. The b-tag selection criteria have been adjusted to lower and respectively raise the efficiency in the estimated error range.

The changed behaviour of identifying the right b-jets for reconstructing the event kinematics is neglegible. The fully reconstructed events have been unfolded with the original settings. The results were shifted by

$$\begin{aligned} \Delta A &= 0.002 \\ \Delta A_D &= 0.001 \end{aligned} \tag{7.27}$$

Compared to the results from the semileptonic channel this is almost an order of magnitude better [33]. The selection of dileptonic events seems to be very stable against this influence. A similar observation was already made in [96].

Fragmentation Function

As the transition from quarks to the final hadrons cannot be calculated in pertubative QCD, fragmentation models have to be used. To estimate the error due to the used model, different settings for the Peterson fragmentation function used by Pythia have been used. The b-fragmentation was changed within the errors obtained by the OPAL collaboration. The correlation observables change by:

$$\begin{aligned} \Delta A &= 0.006 \\ \Delta A_D &= 0.003 \end{aligned} \tag{7.28}$$

Top Mass

While the top mass itself does not influence the spin correlation for dileptonic events in leading order, the top mass is a fixed value in the reconstruction

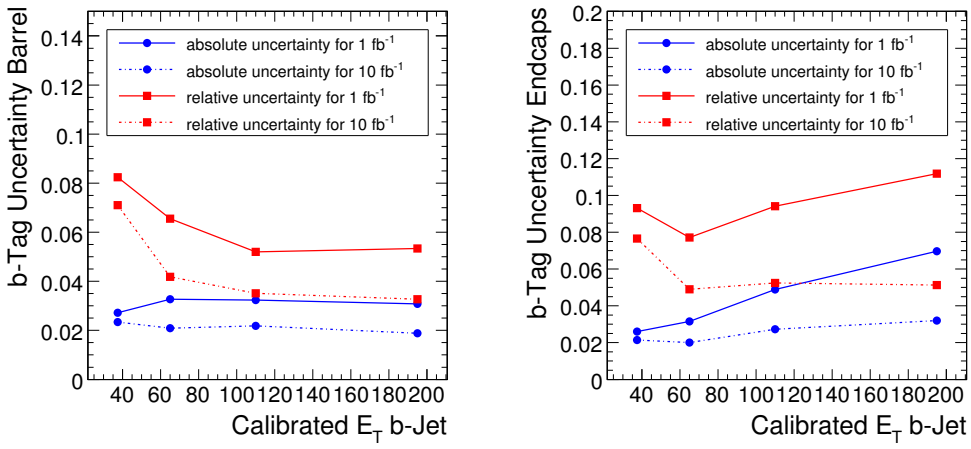

Figure 7.21.: Estimates for the b-tagging uncertainty at different luminosities for barrel (left) and endcap (right). [9]

of the event topology. Assuming an top mass error of $\Delta m_t = 2.5\,\text{GeV}$, the uncertainty is

$$\begin{aligned} \Delta A &= 0.006 \\ \Delta A_D &< 0.001. \end{aligned} \tag{7.29}$$

Pile-up

During the low-luminosity phase on average 3.5 events per bunch crossing on top of the real process will take place. These pile-up events can cause jets with a transverse momentum that is high enough to interfere with the signature of the hard process. Thus the selection of events and jets can be affected.

The effect of pile-up has been checked as follows. Additional samples with a changed number of pile-up events per bunch crossing have been produced. Using 1.0 and 6.0 pile-up events, the measured spin correlations are changed by:

$$\begin{aligned} \Delta A &= 0.004 \\ \Delta A_D &= 0.002 \end{aligned} \tag{7.30}$$

7.10.3. Background Contribution

There are two main effects connected to the background handling. First the cross-section of $t\bar{t}$-production relative to the non-$t\bar{t}$-background. As shown before this background is rather small and not taken into account here. The total selection efficiency of signal events depends on the magnitude of the spin-spin-correlation whereas this is of course not the case for non-$t\bar{t}$-background events. The $t\bar{t}$ background contributions seem not to vary within the statistical error for different spin-correlations. It has to be noted, that the MC statistics are very limited and less than 2,000 simulated events survive the cuts.

Table 7.4.: Summary of the systematic uncertainties for the correlation observables A and A_D.

Effect	A	A_D
Generation		
Q^2 scale	0.013	0.003
PDF	0.008	0.005
ISR/FSR	0.003	0.001
Fragmentation	0.006	0.003
Reconstruction		
B-tagging	0.002	0.001
Jet energy	0.015	0.004
Top mass	0.006	0.001
Pile-up	0.004	0.002
S/B ratio	0.002	0.004
	0.024	0.009

As mentioned in section 7.6.1 it can be taken care of the S/B ratio by using the backround contribution as another cause in the Bayesian unfolding. For the systematic uncertainty a more conservative estimation was done. The background ratio after full event reconstruction of the observables is 6.2. Assuming an uncertainty of 10% for this ratio, the results are shifted by

$$\begin{aligned} \Delta A &= 0.002 \\ \Delta A_D &= 0.004 \end{aligned} \tag{7.31}$$

7.10.4. Summary of Systematics

In table 7.4 a summary of the systematic uncertainties for both considered observables is given. On the generator level, the uncertainties are cleary dominated by the Q^2 scale and the used PDF. This is expected since a changed ratio of $q\bar{q}$ and gg production processes has a direct effect on the spin correlation.

On reconstruction side the b-jet energy scale and the top mass are of importance. Both are important parameters in the event reconstruction and the observables are very sensitive to misreconstructions. A good result is the small sensitivity on the b-tagging uncertainty, which shows that the chosen selection criteria are sufficiently stable.

Comparing the observables A and A_D the former has a much bigger absolute systematic uncertainty, which is about a factor 2.7 higher than for observable A_D. Recalling the definitions of section 4.5, the measurement of A_D only needs the calculation of angles in both top systems separately, while for observable A the calculation has to be done in the combined $t\bar{t}$ system, which is more difficult to reconstruct.

7.11. Overall Result

After selection of 400,000 events at $10\,\mathrm{fb}^{-1}$ approximately 14,700 signal events are left, which corresponds to an efficiency of 3.7%. In contrast about 1,800 background events, mainly $t\bar{t}$ events with τ-leptons, pass the selection criteria.

Using these events for calculating the spin–spin-correlation observables A and A_D a Bayesian unfolding is applied and the resulting distributions are fitted by the expected shapes. Calculating the statistical and systematic uncertainties as explained above, the CMS accuracy for spin–spin-correlations after $10\,\mathrm{fb}^{-1}$ will be:

$$\begin{aligned} A &= 0.415 \pm 0.032\,(\text{stat.}) \pm 0.024\,(\text{syst.}) \\ A_D &= -0.287 \pm 0.014\,(\text{stat.}) \pm 0.009\,(\text{syst.}) \end{aligned} \tag{7.32}$$

The input values for the given scenario are $A = 0.422$ and $A_D = -0.290$, so correct values could be extracted.

These numbers are valid if the size of the signal sample and the cross-checking Monte-Carlo are of the same size. Increasing the MC statistics as discussed in section 7.9 the uncertainty that can be achieved is

$$\begin{aligned} A &= 0.415 \pm 0.02\,(\text{stat.}) \pm 0.024\,(\text{syst.}) \\ A_D &= -0.287 \pm 0.01\,(\text{stat.}) \pm 0.009\,(\text{syst.}) \end{aligned} \tag{7.33}$$

This means, that the precision of the spin–spin-correlation after one year of low luminosity will already be in the 10% region. For higher statistics the measurement will clearly become systematically limited.

The parameter A_D can be measured much more precisely because of its simpler definition and reconstruction. On the other hand A provides a lot more information in case of derivations from the expected Standard Model behaviour and could be capable of detecting top-quark polarizations. Further studies of the sensitivity to polarizations would be a natural extension to the present study.

7.11.1. Comparison with existing studies

There exist two studies for LHC which can be compared with the results obtained here. A previous CMS study on parton level for the dileptonic channel [52], which is not using the cut on $m_{t\bar{t}}$, results in

$$A = 0.311 \pm 0.059\,(\text{stat.}) \pm 0.028\,(\text{syst.}), \tag{7.34}$$

The statistical uncertainty given here was scaled to the statistics of $10\,\mathrm{fb}^{-1}$. Both the statistical and the systematic uncertainty are much worse than for the new study. Though the results seem not to be compatible at first sight, the differences can be explained. The statistical uncertainty of the older CMS study is influenced by the MC statistics available (compare formula 7.20 and 7.21) and due to the used unfolding method, which is a simple bin-by-bin correction that

leads to worse fits. This could be seen in the present study as well and was discussed in section 7.7. The systematic uncertainty is slightly different, because the assumed uncertainty of the PDFs was bigger by a factor of about 2.

A more recent study by ATLAS in the dileptonic channel [96] obtained:

$$\begin{aligned} A &= 0.404 \pm 0.020\,(\text{stat.}) \pm 0.024\,(\text{syst.}) \\ A_D &= -0.290 \pm 0.011\,(\text{stat.}) \pm 0.010\,(\text{syst.}) \end{aligned} \tag{7.35}$$

Even if this study was done on fast simulation for a different detector, the systematic uncertainty is very comparable. This leads to the conclusion that both detectors ATLAS and CMS are rather equal in their capabilities for the study of spin–spin-correlations. The statistical uncertainty of the ATLAS study compares to the estimated uncertainty for unlimited MC tuning statistics as shown in formula 7.21.

It has to be noted that the ATLAS study did a more extensive treatment of the hadronization effects. So it is to be expected that including this the estimate of the systematic uncertainty obtained in the present thesis will slightly increase.

Other channels

Another channel for measuring spin–spin-correlations is the semileptonic $t\bar{t}$ decay, where one W decays leptonically, while the other one decays hadronically. There exist both studies of CMS and ATLAS about the prospects for LHC. According to the analysis by CMS the precision at $10\,\text{fb}^{-1}$ is expected to be

$$A_{b-t,l-t} = 0.346 \pm 0.021\,(\text{stat.})\,^{+0.026}_{-0.055}\,(\text{syst.}), \tag{7.36}$$

where the study uses the b-quark as spin analyzer on the hadronical decay side. The predicted correlation parameter differs due to the not applied cut on $m_{t\bar{t}}$. A full simulation study of ATLAS [106] obtains the following result:

$$\begin{aligned} A &= 0.422 \pm 0.020\,(\text{stat.}) \pm 0.090\,(\text{syst.}) \\ A_D &= -0.288 \pm 0.012\,(\text{stat.}) \pm 0.041\,(\text{syst.}) \end{aligned} \tag{7.37}$$

While the statistical uncertainties of both studies are almost identical, the systematic uncertainties differ significantly. This is likely to be caused by the less complete systematic contributions of the CMS study.

8. Conclusions and Outlook

In the first years of LHC operation top-pairs will be produced at a frequency of about one event per second. This will allow detailed studies of the top quark and its properties. A feature of the pair production in the Standard Model is the correlation of both top spins. This gets reflected in the angular distribution of the decay products. Derivations from the SM predictions could be a hint for resonances in the production and decay processes, i.e. physics beyond SM. Up to now the predicted effects of spin–spin-correlation have not been observed and only very loose limits are set by Tevatron results. With the event rate at LHC this is expected to change.

In general $t\bar{t}$-events can be classified by the further decay of the two Ws from $t\bar{t} \rightarrow b\bar{b}W^+W^-$ as fully hadronic, semileptonic and dileptonic. Only the semileptonic and dileptonic mode seem to be promising for the measurement of spin–spin-correlations. In this thesis the dileptonic channel is explored. The signal definition is tightened to the $e - \mu$ cases only, while decays with τ-leptons are considered to be background.

Very important is the choice of the right observables for measuring the spin–spin-correlation. Two promising ones have been chosen. Those are the correlation A of the helicity angles for the outgoing leptons and the parameter A_D of the opening angle between both leptons. Close attention on the used frames of reference has to be paid. A cut on the invariant mass of the $t\bar{t}$-system increases the correlation. With $m_{t\bar{t}} > 550$ GeV the correlations are $A = 0.422$ and $A_D = -0.290$.

Base of the present study are samples done with CMS full simulation corresponding to $10\,\text{fb}^{-1}$. As generators for the signal Pythia and TopReX were used. The latter was modified to allow for non-SM correlation parameters.

The efficiencies and resolutions of the muons, electrons, b-jets and missing transversal energy reconstruction were studied. Since all leptons considered in this study are originating from Ws criteria to distinguish those leptons from leptons from other sources were explored.

Due to the clear signature the selection of dileptonic $t\bar{t}$ events is possible with standard cut based methods. The remaining background consists mainly of $t\bar{t}$-events that contain one or two τ-leptons. A S/B ratio of 5.3:1 is obtained.

For the study of spin–spin-correlations the whole kinematics of the hard process has to be known. In order to calculate the full event kinematics a polynom

of the fourth order has to be solved. Together with a combinatorical factor of two this results in up to eight event solutions. The efficiency of the solving procedure was tested for different scenarios. All non-trivial methods to increase the solver efficiency of 81.1% lead to significantly larger migration in the final spin observables. The procedure for selecting the right solution is chosen to be as unbiased as possible, resulting in small deviations from methods used for other measurements in the dileptonic channel. An overall purity of 68% was achieved.

After selection and reconstruction the distributions of the spin-observables are completely distorted. This is due to both significant migration caused by the limited resolutions and due to selection efficiencies. To correct for this several unfolding techniques have been compared in quality and performance. Fitted bin-by-bin correction, histogram fitting and Bayesian unfolding turn out to be well suited for the present analysis. Because of making the weakest assumptions on the initial distributions Bayesian unfolding is chosen as method for the later steps.

The discussion of statistical and systematic uncertainties completes this thesis. Base of the statistical uncertainty are $10\,\mathrm{fb}^{-1}$ with the NLO $t\bar{t}$ cross section of 830 pb, corresponding to roughly 400,000 signal events. Main contribution to the systematic uncertainty on the theoretical side are the Q^2-scale and the PDFs. Of a similar magnitude at experimental side is the contribution of the jet energy scale.

Combining the single results, the correlation measurement will have uncertainties of

$$\begin{aligned} A &= 0.415 \pm 0.02\,(\text{stat.}) \pm 0.024\,(\text{syst.}) \\ A_D &= -0.287 \pm 0.01\,(\text{stat.}) \pm 0.009\,(\text{syst.}) \end{aligned} \tag{8.1}$$

Thus spin–spin-correlations can be measured for the present scenario with an accuracy of 10% for A and 7% for A_D. For higher statistics the study will quickly become limited by systematics. The observable A_D seems to be the better observable because of its simpler definition and reconstruction. With this level of precision a search for non-Standard Model effects would be possible.

Though instrumental uncertainties are included in the systematic uncertainty, this study assumes a well understood detector and the results can probably not be extrapolated to the start-up phase of CMS. For example the selection, which relies on b-tagging for Z-background suppression, would need to be modified. A study on this is the would be the next logical step on exploring spin–spin-correlations at CMS.

With the precision in the spin–spin-correlation measurement, a similar sensitivity for top-polarization measurements could be expected. A study on this could use the methods presented here and would be a natural extension to this thesis.

A. Helicity angle calculation

Here a definition of the helicity angle only build of lorentz-invariants is derived. In particular this allows to calculate the helicity angles by using solely momentum information from the laboratory frame without heavy boosting.

Simple lorentz boost calculation

For the following calculations, it is useful to introduce a simple form of lorentz boost calculations. Given the four-vectors p and q are defined in frame A as:

$$\begin{aligned} p &= (p_0, \overrightarrow{p}) \\ q &= (q_0, \overrightarrow{q}) \end{aligned} \tag{A.1}$$

and in frame B as:

$$\begin{aligned} p' &= (m, 0) \\ q' &= (q'_0, \overrightarrow{q}'), \end{aligned} \tag{A.2}$$

then the transformation rules become very simple. For $q' \rightarrow q$ one can use the following transformation rules:

$$q_0 = \frac{p_0 q'_0 + (\overrightarrow{p} \cdot \overrightarrow{q}')}{m}$$

$$\overrightarrow{q} = \overrightarrow{q}' + \frac{q'_0 + q_0}{m + p_0} \cdot \overrightarrow{p}$$

To change from frame A to the center of mass system of p:

$$q'_0 = \frac{pq}{m}$$

$$\overrightarrow{q}' = \overrightarrow{q} - \frac{q'_0 + q_0}{m + p_0}$$

Calculation of the Helicity Angle

As in the definition of the helicity angle we need to to calculate the angle between the top t in the $t\bar{t}$ rest frame and the lepton p_l in the top rest frame. In the following all primed variables are in the top rest frame. The other variables in the $t\bar{t}$ system. p is the top quark.

The base of the calculation is the concept as follows. An angle is calculated by the scalar product of two normalized three-vectors. Using the transformation rules above, the frames are chosen such that the scalar product of the three vectors and the product of the four vectors become identical. This makes it possible to express the helicity angle in means of lorentz-invariant products.

Direction vector of the top quark

q' defines the direction of the top inside the $t\bar{t}$ rest frame:

$$\overrightarrow{q}' = \frac{\overrightarrow{p}}{|\overrightarrow{p}|}$$

q' itself is a four-vector in the top rest frame. If we set it explicitly to 0 it allows us to re-write all expressions in lorentz-invariant form:

$$q'_0 = 0$$

Transformed to the $t\bar{t}$ system q' becomes:

$$q_0 = \frac{\overrightarrow{p}^2}{m \cdot |\overrightarrow{p}|} = \frac{|\overrightarrow{p}|}{m}$$

$$\overrightarrow{q} = \frac{\overrightarrow{p}}{|\overrightarrow{p}|} + \frac{|\overrightarrow{p}|}{m(p_0+m)} \cdot \overrightarrow{p} = \overrightarrow{p} \cdot (\frac{1}{|\overrightarrow{p}|} + \frac{\dots}{\dots}) = \frac{p_0 \cdot \overrightarrow{p}}{m \cdot |\overrightarrow{p}|}$$

Helicity angle calculation

With this q the angle is given by:

$$\cos\theta = \frac{\overrightarrow{q}' \cdot \overrightarrow{l}'}{|\overrightarrow{l}'|}$$

Using $q'_0 = 0$ and the four-vector product $(ql) = \overrightarrow{q}' \cdot \overrightarrow{l}' - q'_0 l'_0 = \overrightarrow{q}' \cdot \overrightarrow{l}'$ the angle can be rewritten as:

$$\cos\theta = \frac{(ql)}{|\overrightarrow{l}'|}$$

Now (ql) is a lorentz invariant and can be calculated in any frame. For the $t\bar{t}$ system it becomes:

$$(ql) = \frac{|\overrightarrow{p}| \cdot l_0}{m} - \frac{p_0(\overrightarrow{p}\,\overrightarrow{l})}{m \cdot |\overrightarrow{p}|}$$

$$= \frac{1}{m|\overrightarrow{p}|} \cdot (\overrightarrow{p}^2 l_0 - p_0 \overrightarrow{p}\,\overrightarrow{l})$$

$$= \frac{1}{m|\overrightarrow{p}|} \cdot ((p_0^2 - m^2)l_0 + p_0 \cdot ((pl) - p_0 l_0))$$

$$= \frac{p_0 \cdot (pl) - m^2 l_0}{m|\overrightarrow{p}|}$$

The denominator of the angle is:

$$|\overrightarrow{l}'| = \sqrt{l_0^2 - \mu^2},$$

where μ is the mass of the lepton. With $l_0 = \frac{(pl)}{m}$ this becomes:

$$|\overrightarrow{l}'| = \frac{\sqrt{(pl)^2 - \mu^2}}{m}$$

Combining both expressions the angle can be written as:

$$\cos\theta = \frac{p_0(pl) - m^2 l_0}{|\overrightarrow{p}|\sqrt{(pl)^2 - m^2\mu^2}}.$$

Transformation to laboratory frame

The variables p_0,l_0, $\overrightarrow{p}$ are defined in the $t\bar{t}$ rest frame but we need them expressed by values from the laboratory frame. Given $c = (E_{tot}, \overrightarrow{c})$ as $t\bar{t}$ four-vector in lab frame this is done by:

$$l_0 = \frac{(lc)}{\sqrt{\hat{s}}}$$

$$p_0 = \frac{(pc)}{\sqrt{\hat{s}}}$$

We get the following expression:

$$\cos\theta = \frac{(pc)(pl) - m^2(lc)}{\sqrt{\hat{s}}|\overrightarrow{p}|\sqrt{(pl)^2 - m^2\mu^2}}$$

For $\overrightarrow{p}$ we can use the follwing expression:

$$\overrightarrow{p} = \overrightarrow{p}^{lab} - \frac{p_0 + p_0^{lab}}{m + \sqrt{\hat{s}}}\overrightarrow{c}$$

Finally we get an expression which can be evaluated by laboratory frame values:

$$\cos\theta = \frac{m^2(lc) - (pc)(pl)}{\sqrt{\hat{s}}|\overrightarrow{p}^{lab} - \frac{(pc)/\sqrt{\hat{s}} + p_0^{lab}}{m+\sqrt{\hat{s}}}\overrightarrow{c}|\sqrt{(pl)^2 - m^2\mu^2}}$$

Special case

If the center of mass system of the $t\bar{t}$-System we can use the fact that both quarks have the same momentum. Now it reduces to:

$$\cos\theta = \frac{2(m^2(lc) - (pc)(pl))}{\hat{s}\sqrt{1 - 4m^2/\hat{s}}\sqrt{(pl)^2 - m^2\mu^2}}$$

B. Mixing non SM-spin correlation

To be able to produce the table 7.3, a set of MC samples with different spin-correlations is needed. Unlike other parameters the spin-correlation is not a value that can be changed simply by a single generator setting like e.g. the top mass. Since different studies on the subject use quite different ways of varying the correlation parameter, an overwiev over the methods, their advantages and drawbacks is needed.

In general there are three parameters that influence the spin correlation. Those are the production process, the invariant mass of the top pair, and the assumption that the spin is completely preserved (no spin flip, no hadronization effects). Thus every derivation changes the phase space.

Weighting the Spin Correlation Distribution

For the simple approach of weighting the spin–spin-correlation to the desired shape one can distinguish two cases. Either one starts with a sample without spin correlation, yielding a flat double differential distribution, or the standard model scenario. Weighting the former with the $\cos\theta_1 \cdot \cos\theta_2$ distribution completely ignores the shape of the phase space, especially the dependency on $m_{t\bar{t}}$. For the latter the situation is slightly better. But here the two production processes are considered being in the same region of the phase space, while they are obviously not (see figure 4.5).

gg vs. qq Contribution

To overcome the problem, that the gg and qq contributions with almost opposite spin states are treated identically, another possibility is weighting the production processes according to the desired spin correlation parameter. Unfortunately the phase space is limited and not the hole correlation range of -1 to $+1$ can be modelled. This is especially true for regions far from the threshold. In addition polarizations cannot be introduced. Both the gg and the qq subset are themselves unpolarized.

Mixing Helicity States

The former methods have the problem that either all MC events get individual weights or a significant fraction of events has to be thrown away. Others cannot model the hole parameter range and all destroy the shape of the phase space. This is the reason why TopReX was extended to produce the four helicity states explicitly. With this one gets a much higher flexibility in exploring

the parameter phase space. In particular, these four states can be used to rebuild the four parts of equation 4.13, which provide together with the helicity states another natural basis of the distribution.

Even if the difference between different approaches is not too big and they can be combined with each other, one should nevertheless start with a well defined scenario. For this study a mixing of the helicity states was done.

List of Figures

List of Tables

Bibliography

[1] The LHC Design Report, Volume 1: The LHC Main Ring. CERN 2004-003-v1, 1995/2004. URL: http://ab-div.web.cern.ch/ab-div/Publications/LHC-DesignReport.html.

[2] The LHC Design Report, Volume 3: The LHC Injector Chain. CERN 2004-003-v3, 1995/2004. URL: http://ab-div.web.cern.ch/ab-div/Publications/LHC-DesignReport.html.

[3] The LHC Design Report, Volume 2: The LHC Infrastructure and General Services. CERN 2004-003-v2, 1995/2004. URL: http://ab-div.web.cern.ch/ab-div/Publications/LHC-DesignReport.html.

[4] ALICE Collaboration. Technical proposal. Technical report, CERN/LHCC 95–71 LHCC/P3, 1995.

[5] ATLAS Collaboration. Technical proposal, 1994.

[6] LHCB Collaboration. Technical proposal, 1998.

[7] LHCf Collaboration. Technical proposal. Technical report, CERN/LHCC 2005-32 LHCC/P007, 2004.

[8] M. Deile. TOTEM: Forward Physics at the LHC. hep-ex 0410084, URL: http://arXiv.org/abs/hep-ex/0410084, October 2004.

[9] CMS Collaboration. CMS Physics Technical Design Report Vol I: Detector Performance and Software. CERN/LHCC 2006-001, February 2006.

[10] Ch. Hoermann. *Design and Performance of the Silicon Pixel Detector Modules for the CMS Experiment*. PhD thesis, Universität Zürich, 2006.

[11] St. Kasselmann. *Untersuchung der Qualitätskriterien für die CMS-Silizium-Module anhand einer Prototypserie*. Diploma thesis, RWTH Aachen, 2003.

[12] M. Axer. *Development of a Test System for the Quality Assurance of Silicon Microstrip Detectors for the Inner Tracking System of the CMS Experiment*. Phd thesis, IIIB, 2003.

[13] T. Franke. *Development and Evaluation of a Test System for the Quality Assurance during the Mass Production of Silicon Microstrip Modules for the CMS Experiment*. Phd thesis, IIIB, 2005.

[14] W. Adam et al. The effect of highly ionising particles on the CMS silicon strip tracker. *Nucl. Instrum. and Methods*, A543, 2005.

[15] CMS Collaboration. The tracker project, technical design report. CERN/LHCC 98-6, April 1998.

[16] CMS Collaboration. Addendum to the CMS Tracker TDR. CERN/LHCC 2000-016, February 2000.

[17] Rutherford Appleton Laboratory - Particle Physics Department. *Electron Shower Simulation*. URL: `http://hepwww.rl.ac.uk/OpenDays97/images/CMS_ECAL_shower.gif`.

[18] P. Adzic et al. Energy resolution of the barrel of the cms electromagnetic calorimeter. CMS Note 2006/148, CERN, November 2006.

[19] CMS Collaboration. The Hadron Calorimeter, Technical Design Report. CERN/LHCC 97-31, June 1997.

[20] James Rohlf. Design, performance and calibration of cms hadron-barrel calorimeter wedges. CMS NOTE 2006/138, August 2006.

[21] CMS Collaboration. The magnet project, technical design report. CERN/LHCC 97-10, May 1997.

[22] CMS Collaboration. The Trigger and Data Acquisition Project, Volume I. The Level 1 Trigger, Technical Design Report. CERN/LHCC 2000-38, December 2000.

[23] S. Vanini, M. Vasquez Acosta, C. Leonidopoulos, S. Esen, R. Harris, K. Lassila-Perini, C. Delaere, S.R. Dasu, C. Hogg, J.L. Leonard. 2e33 trigger tables for ptdr, volume 2. CMS AN 2006/085, CERN, May 2006.

[24] CMS Collaboration. The Trigger and Data Acquisition Project, Volume II. Data Acquisition and High-Level Trigger, Technical Design Report. CERN/LHCC 2002-26, December 2002.

[25] J. Pumplin, D. R. Stump, J. Huston, H. L. Lai, P. Nadolsky, and W. K. Tung. New Generation of Parton Distributions with Uncertainties from Global QCD Analysis. *JHEP*, 0207:012, 2002.

[26] ZEUS Collaboration. A ZEUS next-to-leading-order QCD analysis of data on deep inelastic scattering. *Physical Review D*, 67:012007, 2003.

[27] Rick Field. The underlying event in hard scattering processes. hep-ph 0201192, URL: `http://arXiv.org/abs/hep-ph/0201192`, January 2002.

[28] S.R. Slabospitzky. CMS values for the major SM cross sections.

[29] M.L.Mangano(ed.), G.Altarelli(ed). Workshop on standard model physics (and more) at the lhc. Yellow report, 2000–2004, CERN, 1999.

[30] The ALEPH Collaboration and The DELPHI Collaboration and the L3 Collaboration and The OPAL collaboration and The SLD Collaboration and the LEP Electroweak Working Group and the SLD Electroweak and Heavy Flavour Groups. Precision Electroweak Measurements on the Z Resonance. *Physics Reports*, 427:257, 2006.

[31] Nicola Cabibbo. Unitary symmetry and leptonic decays. *Physical Review Letters*, 10(12):531–533, June 1963.

[32] Makoto Kobayashi and Toshihide Maskawa. CP violation in the renormalizable theory of weak interaction. *Prog. Theor. Phys.*, 49:652ßß657, 1973.

[33] CMS Collaboration. CMS Physics Technical Design Report Vol II: Physics Performance. CERN/LHCC 2006-021, June 2006.

[34] Particle Data Group. Particle physics booklet, July 2004.

[35] G. L. Fogli and E. Lisi and A. Marrone and A. Melchiorri and A. Palazzo and P. Serra and J. Silk and A. Slosar. Observables sensitive to absolute neutrino masses: A reappraisal after WMAP-3y and first MINOS results. *Physical Review D*, 75:053001, 2007.

[36] Stephen P. Martin. A Supersymmetry Primer, 1997.

[37] F. Abe et al. Evidence for top quark production in $\bar{p}p$ collisions at $\sqrt{s}$ = 1.8 tev. Technical Report 73, 225, 1994.

[38] F. Abe et al. Observation of top quark production in pbar-p collisions. Technical Report 74, 2626, 1995.

[39] The Tevatron Electroweak Working Group. Combination of CDF and D0 Results on the Mass of the Top Quark. hep-ex 0608032, URL: `http://arXiv.org/abs/hep-ex/0608032`, August 2006.

[40] A. Quadt. *Top Quark Physics at Hadron Colliders*. Springer, 2007.

[41] M. Beneke et al. Top quark physics. hep-ph 0003033, CERN, March 2000. URL: `http://arXiv.org/abs/hep-ph/0003033`.

[42] M. Mohammadi Najafabadi. Single top production at LHC. 2006.

[43] `http://www-d0.fnal.gov/Run2Physics/top/top_public_web_pages/top_feynman_diagrams.html`.

[44] CDF collaboration. A Limit on the Top Quark Width and the Lifetime using the Template Method in the Lepton plus Jets Channel at CDF II. CDF note 8953, 2007.

[45] T. Stelzer and S. Willenbrock. Spin correlation in top-quark production at hadron colliders. *Physics Letters B*, 374:169–172, 1995.

[46] Gregory Mahlon and Stephen Parke. Angular correlations in top quark pair production and decay at hadron colliders. *Physical Review D*, 53(9):4886–4896, May 1996.

[47] Werner Bernreuther, Arnd Brandenburg, and Peter Uwer. Transverse Polarization of Top Quark Pairs at the Tevatron and the Large Hadron Collider. *Physics Letters B*, 368:153, 1996.

[48] W. Bernreuther, A. Brandenburg, Z. G. Si, and P. Uwer. Top quark pair production and decay at hadron colliders. *Nuclear Physics B*, 690:81, 2004.

[49] Arnd Brandenburg. Spin-spin correlations of top quark pairs at hadron colliders. *Phys. Lett.*, B388:626–632, 1996.

[50] Gregory Mahlon and Stephen J. Parke. Maximizing spin correlations in top quark pair production at the tevatron. *Phys. Lett.*, B411:173–179, 1997.

[51] Peter Uwer. Maximizing the spin correlation of top quark pairs produced at the lhc. *Phys. Lett.*, B609:271–276, 2005.

[52] Lars Sonnenschein. *The $t\bar{t}$ production in pp collisions at $\sqrt{s} = 14$ TeV*. Pitha, RWTH Aachen, 2001.

[53] S.R. Slabospitzky, L. Sonnenschein. TOPREX Generator, Ver. 3.25. hep-ph 0201292, URL: `http://arXiv.org/abs/hep-ph/0201292`, January 2002.

[54] Pythia 6.2 physics and manual. hep-ph 0108264, URL: `http://arXiv.org/abs/hep-ph/0108264`, April 2003.

[55] D0 Collaboration and B. Abbott. Spin Correlation in $t\bar{t}$ Production from $p\bar{p}$ Collisions at $\sqrt{s} = 1.8$TeV. *Physical Review Letters*, 85:256, 2000.

[56] *CMKIN, Physics event generation, Manual*, November 2005. URL: `http://cmsdoc.cern.ch/cmsoo/projects/CMKIN`.

[57] Michelangelo L. Mangano, Fulvio Piccinini, Antonio D. Polosa, Mauro Moretti, Roberto Pittau. Alpgen, a generator for hard multiparton processes in hadronic collisions. hep-ph 0206293, URL: `http://arXiv.org/abs/hep-ph/0206293`, June 2005.

[58] St. Kasselmann. *Top Quark Mass Measurement in the Lepton+Jets Channel using Full Simulation of the CMS Detector*. PhD thesis, RWTH Aachen, 2007.

[59] CERN. *OSCAR, Object Oriented Simulation for CMS Analysis and Reconstruction*. URL: `http://cmsdoc.cern.ch/oscar`.

[60] S. Agostinelli et al. *GEANT4: A simulation toolkit*, 2003. URL: `http://geant4.web.cern.ch/geant4`.

[61] Michael Case. Xml based detector description language. CMS Note (Draft) 2005/000, URL: `http://cmsdoc.cern.ch/cms/software/ddd/www/draft1.3_cms_ddl.pdf`, April 2005.

[62] V. Innocente, L. Silvestris, D. Stickland. CMS Software Architecture - Software framework, services and persistency in high level trigger, reconstruction and analysis. Computer Physics Communications 140, 2001.

[63] Pavel Demin, Giacomo Bruno. *ExRootAnalysis - a tool for CMS data analysis, preliminary draft*. UCL/FYNU, Louvain-la-Neuve, Belgium, February 2005.

[64] http://cmsdoc.cern.ch/FAMOS.

[65] CMS Collaboration. The computing project technical design report. CERN/LHCC 2005-23, June 2005.

[66] Rene Brun, Fons Rademarkers et al. *ROOT - An Object Oriented Data Analysis Framework, Ver. 4.04/02*, July 2004.

[67] Christopher D. Jones, Benedikt Hegner, and Luca Lista. Analysis Environments for CMS. In *International Conference on Computing in High Energy and Nuclear Physics*, 2007.

[68] Luca Lista, Francesco Fabozzi, Benedikt Hegner, and Christopher D. Jones. Physics Analysis Tools for the CMS experiment at LHC. In *International Conference on Computing in High Energy and Nuclear Physics*, 2007.

[69] R. Frühwirth. Application of kalman filtering to track and vertex fitting. *Nucl. Instrum. and Methods A*, 262:444–450, 1987.

[70] W. Adam, B. Mangano, T. Speer, T. Todorov. Track reconstruction in the cms tracker. CMS Note 2006/041, CERN, December 2005.

[71] S. Cucciarelli, M. Konecki, D. Kotlinski, T. Todorov. Track reconstruction, primary vertex finding and seed generation with the pixel detector. CMS Note 2006/026, CERN, January 2006.

[72] T. Speer, K. Prokofiev, R Fruhwirth, W. Waltenberger, P. Vanlaer. Vertex fitting in the cms tracker. CMS NOTE 2006-032, CERN, 2006.

[73] G. Bruno, P.T. Cox, S. Lacaprara, N. Neumeister, B. Van de Vyver, S. Villa, R. Wilkinson. Local reconstruction in the muon detectors. CMS Note 2002/043, CERN, December 2002.

[74] E. Gatti et al. Analysis of the position resolution in centroid measurements in mwpc. Technical Report 188, 327-346, 1981.

[75] V. Innocente et al. Geane, average tracking and error propagation package. CERN Program Library W5013-E, 1991.

[76] I. Belotelov, N. Neumeister. Performance of the CMS offline muon reconstruction software. CMS AN 2005/010, CERN, June 2005.

[77] Steven Lowette. *B-Tagging as a Tool for Charged Higgs Boson Identification in CMS*. PhD thesis, Vrije Universiteit Brussel, 2006.

[78] E. Meschi, T. Monteito, C. Seez, P. Vikas. Electron Reconstruction in the CMS Electromagnetic Calorimeter. CMS 2001/034, CERN, June 2001.

[79] G. Daskalakis. Cms ecal calibration strategy. CMS Conference Report 2006/065, July 2006.

[80] A. Heister, O.Kodolova, S. Petrushanko, V. Konoplianikov, J. Rohlf, C. Tully, A. Ulyanov. Jet reconstruction and performance in the cms detector. CMS AN 2005/005, CERN, June 2005.

[81] D. Benedetti, S. Cucciarelli, J. D'Hondt, A. Giammanaco, J. Heyninck, A. Schmidt, C. Weiser. The QCD, EW, and Higgs working group - Study of Jet Clustering Algorithms at the LHC. hep-ph 0604120, URL: `http://arXiv.org/abs/hep-ph/0604120`, April 2006.

[82] Alexander Schmidt. *Search for $H \rightarrow b\bar{b}$ in Association with a $t\bar{t}$ Pair in Proton–Proton Collisions at $\sqrt{s} = 14$TeV*. PhD thesis, University of Karlsruhe, 2006.

[83] A. Heister et al. Measurement of jets with the cms detector at the lhc. CMS Note 2006-036, CERN, 2006.

[84] R. Harris. Jet Calibration from Di-jet Balancing. CMS IN 34, CERN, 2005.

[85] V. Konoplianikov, A. Ulyanov, O. Kodolova. Jet Calibration using γ+Jet Events in the CMS Detector. *The European Physical Journal C*, Volume 46:37–43, 2006.

[86] J.D'Hondt, S. Lowette, J. Heynick, S. Kasselmann. Light quark jet energy scale calibration using the w mass constraint in single-leptonic ttbar events. CMS AN 2006/025, CERN, January 2006.

[87] C. Weiser. A combined secondary vertex based b-tagging algorithm in cms. CMS AN 2005/042, CERN, November 2005.

[88] Haifeng Pi, P. Avery, D. Green, J. Rohlf, C. Tully. Measurement of missing transverse energy with the cms detector at the lhc. CMS Note 2006/035, CERN, February 2006.

[89] M. Davids et al. Measurement of top-pair cross section and top-quark mass in the di-lepton and full-hadronic channels with cms. CMS Note 2006/077, CERN, May 2006.

[90] D. Tornier. *Untersuchung dileptonischer $t\bar{t}$-Zerfälle bei CMS*. Diploma thesis, RWTH Aachen, 2005.

[91] Lars Sonnenschein. Algebraic approach to solve $t\bar{t}$ dilepton equations. *Physical Review D*, 72, 2005.

[92] Lars Sonnenschein. Analytical solution of $t\bar{t}$ dilepton equation. *Physical Review D*, 73, 2006.

[93] Volker Blobel. Unfolding methods in high energy physics. 1984.

[94] Andreas Hoecker and Vakhtang Kartvelishvili. SVD Approach to Data Unfolding. *Nucl. Instrum. and Methods A*, 372:469, 1996.

[95] G. D'Agostini. A multidimensional unfolding method based on Bayes' theorem. *Nucl. Instrum. and Methods A*, 362:487–498(12), 1995.

[96] F. Hubaut, E. Monnier, P. Pralavorio, V. Simak, and K. Smolek. ATLAS sensitivity to top quark and W boson polarization in $t\bar{t}$ events. *Eur. Phys. J.*, C44S2:13–33, 2005.

[97] Volker Blobel. An unfolding method for high energy physics experiments. hep-ex 0208022, DESY, 2002.

[98] http://www.scipy.org.

[99] `http://www.slac.stanford.edu/~dimarcoe/HTML/bayesian_unfolding.html`.

[100] `http://www.roma1.infn.it/~dagos/bayes_distr.txt`.

[101] T. J. Loredo. From laplace to supernova sn 1987a: Bayesian inference in astrophysics. *Maximum Entropy and Bayesian Methods*, 1990.

[102] P. Bartalini, R. Chierici, A. De Roeck. Guidelines for the estimation of theoretical uncertainties at the lhc. CMS AN 2005/013, CERN, September 2005.

[103] F. Hubaut, E Monnier, P. Pralavorio, B. Resende, and C. Zhu. Polarization studies in $t\bar{t}$ semileptonic events with atlas full simulation. Atl-phys-pub-2006-022, CERN, 2006.

[104] D Bourilkov, R C Group, and M R Whalley. LHAPDF: PDF use from the Tevatron to the LHC. hep-ph/0605240, 2006.

[105] J. Rohlf, C. Tully. Recommendations for Jet and Missing Transverse Energy Reconstruction Settings and Systematic Treatment. CMS IN 2006/025, CERN, May 2006.

[106] Bernardo Resende. *Étude du quark top avec ATLAS au LHC. Mise en route du calorimètre électromagnétique*. PhD thesis, Université de la Méditerranée Aix-Marseille II, 2007.

Acknowledgement

Of course nobody can write a thesis without the support of other people. Therefore I want to thank the many of you who helped me the past few years.

- My supervisor Prof. Dr. Joachim Mnich gave me the great opportunity to work on the interesting field of top physics. I appreciate the freedom I had while working in his group.
- Prof. Dr. Peter Schleper for his support, especially at the beginning of this thesis when we not yet had a CMS group at DESY.
- Without my colleagues Alex and Christoph it would never have been so much fun. I hope to see you staying in physics! Alex, I am still suprised how you survived my attempts to poison you with strong coffee. ;-)
- Thanks to Dr. Andreas Nowack and Dr. Stefan Kasselmann for keeping me motivated all the time!
- I enjoyed the time at DESY! It started with a warm welcome, when I initially joined the FLC group. It was a real pleasure to work with you all! I want to thank my CMS colleagues at DESY and the University of Hamburg. Especially Dr. Hannes Jung for his valuable comments to my thesis.
- Thanks to Dr. Sergey Slabospitzky for his help during my stay at CERN. Especially his explanations about top physics, spin correlations and TopReX internals. For the understanding of top physics Dr. Peter Uwer gave fruitful tips. Thanks for the patience in cross reading my theory chapter.
- The Cusanuswerk, who supported this thesis and gave me the opportunity to spend time on other things besides physics.
- Finally I want to thank my parents and my sisters. You have given more than I ever asked for. Thanks for everything!